

Western Australian School of Mines

Investigating the Corrosion Characteristics of Carbon Steel and the
Efficacy of Phenolic-Epoxy Coatings in Enclosed Environments

Saleh Ahmed S Alsaleh

This thesis is presented for the Degree of
Doctor of Philosophy
of
Curtin University

July 2023

Declaration

To the best of my knowledge and belief this thesis contains no material previously published by any other person except where due acknowledgment has been made. This thesis contains no material which has been accepted for the award of any other degree or diploma in any university.

Signature: .....

Date:28/07/2023

Abstract

Organic coatings are widely used for the corrosion protection of metals in marine environments because they provide good protection against corrosion at a relatively low cost. In marine environments, active corrosion in enclosed systems, such as ballast tanks or corrosion under insulation (CUI), cannot be effectively halted by organic coatings. The maximum operating temperature for organic coating systems is often defined by dry heat exposure, but this is not highly relevant to enclosed environments under water immersion where the maximum operating temperature of the coating is dramatically reduced.

In this study, the ability of phenolic-epoxy coatings to prevent corrosion in enclosed environments was investigated. In enclosed environments, metals are often exposed to aggressive conditions, such as high temperature (isothermal or cyclic conditions), corrosive salts such as seawater and various pH levels. To evaluate the performance of phenolic-epoxy coatings under enclosed conditions, the performance of freshly coated carbon-steel panels was compared with that of coated specimens after thermal treatment at 120 °C.

Case study I focused on simulating the effect of carbon steel in closed environments (i.e., CUI conditions or ballast tanks). To evaluate the corrosion behaviour and mechanism when the samples were immersed in 3.5 wt. % NaCl solution vs. exposed to condensation conditions. Electrochemical methods were applied to monitor corrosion.

In case study II, a phenolic-epoxy coating was exposed to different heating conditions (isothermal or cyclic temperatures) based on high dry temperatures. The highest performance of the coated panels was observed after exposure to thermal cycling (22–120 °C) for 40 d, whereas cracking of the coating was observed after treatment at 150 °C for 3 d.

In case study III, the corrosion performance of panels coated with commercial phenolic epoxy was analysed after exposure to thermal cycling (22–120 °C for 40 d) and compared to that of freshly coated specimens. Accelerated corrosion tests were conducted in (3.5 and 5.0 wt. % NaCl solutions) in an enclosed system at 80 °C for 60 d. The effect of chloride ions on the coatings was investigated by visual observation (degree of blistering and degree of degradation around an artificial scribe in the coating) and electrochemical measurements. More significant degradation of the freshly coated panels was observed after exposure to 3.5 wt. % NaCl than 5.0 wt.% NaCl. The exposure of the organic coatings to heat provided improved resistance against severe marine conditions.

Case study IV compared the performance of phenolic-epoxy-coated panels before and after thermal exposure (thermal cycling; 22–120 °C for 40 d). The effect of the solution pH (4

or 8) on the coated specimens was evaluated in simulated seawater (3.5 wt. % NaCl solutions) at 80 °C for 60 d. These tests aimed to mimic the acidic/alkaline marine environments as different enclosed environments with different pH ranges. The results of electrochemical measurements and the degree of blistering and delamination around scribed regions of the coated panels showed that the alkaline 3.5 wt. % NaCl solution caused greater coating degradation than a similar acidic solution. In contrast, thermal treatment of the coated panels improved corrosion protection against severe marine conditions at both pH levels.

Overall, this study identified the conditions under which phenolic-epoxy coatings provide maximum corrosion protection to steel in enclosed environments. In conclusion, the case studies demonstrate that heat treatment of the coated panels improves their coating performance in enclosed environments.

Acknowledgements

I would like to thank my supervisors A/Prof. Thunyaluk (Kod) Pojtanabuntoeng, A/Prof. Katerina Lepkova and Dr. Yang Hou for their countless hours of guidance, inspiration and support through my Ph.D. study. Special thanks to Prof. Mariano Iannuzzi for giving me such great support in conducting experiments in the Curtin Corrosion Centre. I found a great wealth of knowledge from you all.

I am grateful to my student colleagues Silvia Salgar, Lina Silva Bedoya, Sri Kambhampati, Janice Xin and Ricardo Santamaria, and the staff in corrosion centre, particularly Ammar Al Helal, Darwin Hartono, Yu Long, Yousuf Abdulwahhab and Marisa Yookhong. They not only helped me in the laboratory but also provided ideas for my research.

I would also, like to express my gratitude to Royal Saudi Naval Forces for offering me scholarship to complete this research project.

I dedicate this thesis to my parents Ahmed Alsaleh and Najiba Alshubiki, and my brothers Araf, Raed, Jamal, Entesar, Musaad and Hajar. Special thanks to my family, my wife Alaa Algusayar, my daughters Rema, Joud and Noor for supporting me to pursue my dream in a foreign country. I would never have had the confidence and endurance to finish this project without your unconditional love.

Peer Reviewed Publications

Journal Publication or submitted

1. S. Ahmed, Y. Hou, K. Lepkova, T. Pojtanabuntoeng, Investigation of the effect chloride ions on carbon steel in closed environments at different temperatures, published 27 June 2023 in Journal of Corrosion and Materials Degradation.

2. S. Ahmed, K. Lepkova, X. Sun, T. Pojtanabuntoeng, The performance of phenolic epoxy coating after exposure to high temperatures, submitted to Journal of Corrosion and Materials Degradation and under revision.

International Conference

S. Ahmed, K. Lepkova, T. Becker, T. Pojtanabuntoeng, The performance of phenolic epoxy coating after thermal exposure for corrosion protection in marine environments, paper no. C2023-19046, AMPP International Corrosion Conference Series, 2023.

I warrant I have obtained, where necessary, permission from the copyright owners to use any third-party copyright material reproduced in the thesis, or to use any of my own published work in which the copyright is held by another party.

Statement of Contribution by Others

I, Saleh Ahmed, as the first author of the publications comprising this thesis was primarily involved in planning and conducting the experiments, data analysis and interpretation and manuscript preparation. Contributions by the co-authors is mentioned below and the written statements from the co-authors are included in appendix 1.

Thunyaluk Pojanabuntoeng significantly contributed in all experiments design, the conception of data interpretation and the preparation and appraisal of the manuscripts. Katerina Lepkova provided valuable ideas regarding the experiment design and actively in data analysis, preparation and modification of the manuscripts. Yang Hou greatly helped in the experiment design and execution of all experiments as well as the perpetration and revision of the manuscripts. Thomas Becker participated particularly with Raman data analysis, and modification of the manuscript. William Rickard and Xiao Sun helped in interpreted the ToF-SIMS data and revision of the manuscript.

All the experiments were conducted at the Corrosion Centre of Curtin University. Financial support for this research was provided by Royal Saudi Naval Forces (RSNF).

Table of contents

LIST OF SYMBOLES AND ABBREVIATIONS	XI
CHAPTER 1	1
INTRODUCTION	1
1.1 Background	1
1.2 Objectives	1
1.3 Thesis structure	4
CHAPTER 2	5
LITERATURE REVIEW	5
2.1 Electrochemical corrosion	5
2.2 Corrosion in enclosed environments.....	8
2.3 Protective coatings	13
2.3.1 Phenolic-epoxy coatings	15
2.3.2. Permeation of corrosive species through organic coatings	21
2.3.3 Adhesive failure	23
2.4 Typical methods for investigating protective properties and degradation mechanisms.	29
2.4.1 Surface characterisation methods.....	29
2.4.2 Electrochemical technique	35
2.4.3 Physical characterisation techniques.....	39
2.5 REFERENCES	41
CHAPTER 3	41
Effect of Chloride Ions and Temperature on the Corrosion of Carbon Steel in Closed Environments	58
3.1. Introduction.....	59
3.2. Experimental	60
3.2.1 Materials and corrosion solutions	60
3.2.2 Test procedures	60
3.2.3 Post-test analysis	62

3.3. Results and discussion	63
3.3.1 Uniform corrosion.....	63
3.3.2 Localised corrosion.....	64
3.3.3 Corrosion product layer	66
3.3.3.1 Morphology and composition	66
3.3.4 Chemical composition.....	71
3.3.5 Electrochemical behaviour.....	73
3.4. Conclusions.....	82
3.5. References.....	83
CHAPTER 4	86
Performance of Phenolic-Epoxy Coatings after Exposure to High Temperatures.....	87
4.1 Introduction.....	88
4.2 Experiments	88
4.2.1 Materials	88
4.2.2 Exposure conditions.....	89
4.3 Characterisation techniques	90
4.3.1 Pull-off adhesion strength	90
4.3.2 EIS.....	90
4.3.3 Thermal analysis	91
4.3.4 FTIR.....	91
4.3.5 ToF-SIMS	92
4.4 Results and discussion	93
4.4.1 Pull-off adhesion strength	93
4.4.2 Electrochemical properties.....	95
4.4.3 Thermal behaviour	101
4.4.4 Chemical properties	103
4.4.5 Molecular structure of the coatings.....	106
4.5 Conclusions.....	109
4.6 References.....	110

CHAPTER 5	112
Influences of NaCl and pH on a Phenolic Epoxy Coating.....	113
5.1 Introduction.....	114
5.2 Experiments	116
5.2.1 Materials	116
5.2.2 Exposure conditions.....	116
5.2.3 Setup of the test cell.....	116
5.3 Coating characterisation techniques.....	118
5.3.1 Degree of delamination and corrosion around scribed regions.....	118
5.3.2 Blister detection	119
5.3.3 EIS.....	119
5.3.4 Characterisation of corrosion products	120
5.3.5 Thermal analysis	120
5.4 Results and discussion	121
5.4.1 Influence of NaCl concentrations.....	121
5.4.2 Influence of pH levels of 3.5 wt. % NaCl.....	140
5.5.4 Thermal behaviour	151
5.5. Conclusions.....	155
5.6 References.....	156
CHAPTER 6	161
CONCLUSIONS AND FUTURE WORK	161
6.1 Conclusions.....	161
6.2 Future work.....	163

LIST OF SYMBOLS AND ABBREVIATIONS

CUI	corrosion under insulation
PE	phenolic epoxy coating
EP	epoxy resin
DGEBA	diglycidyl ether of bisphenol A
EDA	ethylene diamine amine
TSA	thermal spray aluminium
A	working surface area of an electrode
EN	electrochemical noise
ECN	electrochemical current noise
EPN	electrochemical potential noise
ZRA	zero resistance ammeter
R_n	noise resistance
I	current signal (nA)
E	potential signal (mV)
EIS	electrochemical impedance spectroscopy
WE	working electrode
CE	counter electrode
RE	reference electrode
OCP	open circuit potential
AC	alternating current (A)
DC	direct current (A)
R_s	solution resistance (Ω)
R_{ct}	charge transfer resistance (Ω)
C	coating capacitance ($\mu\text{F}/\text{cm}^2$)
f	frequency (Hz)

CPE	constant phase element
Q	CPE parameter of capacitor ($\mu\text{F cm}^2 \text{s}^{\alpha-1}$)
Q_{dl}	double layer of CEP ($\mu\text{F cm}^2 \text{s}^{\alpha-1}$)
α	power-law exponent in model I (dimensionless)
R_c	coating resistance ($\Omega.\text{cm}^2$)
Z_{CPE}	CPE impedance ($\Omega.\text{cm}^2$)
Z_i	imaginary impedance
Z_{real}	real impedance
Z_w	Impedance of the Warburg element
σ	the Warburg coefficient
DFT	dry film thickness
CR	corrosion rate (mpy)
PF	pitting factor
c	delamination value
w	width of artificial scribe
w_c	mean width of coating delamination
K	thermal conductivity (W/mK)
SEM	scanning electron microscopy
EDS	energy dispersive X-ray spectroscopy
RE	Raman spectroscopy
TA	thermal analysis
TGA	thermogravimetric analysis
DSC	differential scanning calorimetry
T_g	glass transition temperature
FTIR	Fourier transform infrared spectroscopy
ToF-SIMS	time of flight - secondary ion mass spectroscopy
GS	glass cell test

CHAPTER 1

INTRODUCTION

1.1 Background

Corrosion is a significant global problem which has not only an environmental impact in terms of material damage and pollution, but also has a huge economic impact because of the material loss in industries and the budget set aside for corrosion control and maintenance of equipment and systems subjected to corrosion. Almost every metallic material that we use in our daily life is subjected to corrosion in one way or another. Corrosion can be considered to be a natural phenomenon in which pure metals and alloys form a stable compound after the interaction with a surrounding corrosive environment chemically or electrochemically [1]. Corrosion is an electrochemical phenomenon which requires four components: anode, cathode, electrolyte and an electrical connection [2]. A chain of electrochemical processes takes place during the corrosion process which involves the dissolution of metal ions into the electrolytic solution at the anode, which is, comparatively, a more active site during the electrochemical phenomenon. Following that, the electrons are transferred from the metal undergoing corrosion to a cathode, through an electric current through the metal [3] and an ionic current traversing the solution completes the electrical circuit.

Variation in the temperature of the aqueous medium affects rates of corrosion. With rising temperature, kinetics of reactions increases. However, oxygen solubility decreases with increasing temperature. Thus, in the open system, corrosion rate is reportedly peaked around 80 °C [4].

On the contrary, corrosion rate tends to increase with temperature in an enclosed environment [5]. Additionally, the micro-environment created in an enclosed space can be complicated, such as insulated steel piping and vessels, storage tanks, bilge, or ballast tanks [6-9,10].

An effective method for controlling corrosion is the isolation of the metallic material to be protected from the corrosive media by a protective coating. Coatings are still the most commonly utilised technique for protecting metallic materials against corrosion [11]. Protective coatings (organic or metallic) are used as the barrier to prevent corrosion of the metallic substrate. It acts as a barrier preventing corrosive species to reach the metal underneath the coating [12].

General characteristics for an efficient coating system are good adhesion, durability and corrosion resistance. Corrosion resistance provided by coatings depends upon: (1) surface

preparation, (2) the application procedure, and (3) coating properties [12]. In addition, when coatings are used, the entire coating system, not just the coating itself, must be carefully considered. For example, SP0198-2010 [13] recommends coatings for insulated austenitic and carbon steels. However, coating degradation is still inevitable even after proper selection of a type of coating and following the specifications, particularly when exposed to an aggressive corrosion environment. For instance, most coatings function well in moderate temperature but high temperature exposure can cause some coatings to be brittle, less flexible, and leading to cracks [14].

For carbon steel, the coating types recommended by NACE publication SP0198 for hot water immersion conditions are amine-cured-coal tar epoxy, and epoxy-phenolic [15]. Metallic coating such as thermally sprayed aluminium (TSA) coatings have performed successfully in marine and high-temperature environments. Inorganic zinc coating has dry heat resistance, but serious failures have been reported in wet environments [12].

Organic coatings as an effective means of corrosion protection have been widely applied in enclosed environments [16,18] that may be subjected to aggressive corrosive environments involving seawater, high temperature and humidity. Kristian Haraldsen implemented a steam heating system in conjunction with a test flow loop to evaluate three types of coating (high temperature inorganic copolymer coating, phenolic epoxy coating, and thermally sprayed aluminium (TSA)) at 140 °C. The test results show that phenolic epoxy coating had the best performance among all the coating tested [19].

Despite the efficiency of coatings in the SP0198 standard [13] to application at elevated temperatures, phenolic epoxy coating was selected to be applied on carbon steel to deal with wet/ dry conditions to mitigate corrosion among all coatings types as a result of a previous study [19]. Phenolic-epoxy coatings results from reaction between epoxy resins and hardening agents, thereby forming a protective layer [20]. Such resins are known to confer excellent mechanical properties [21-22], chemical resistance [23], anti-corrosive properties [24-25] and thermal stability [26-27] due to their highly cross-linked nature. Nonetheless, for every application reliant on the mechanical or barrier properties of an epoxy resin, wet conditions (moisture or immersion) are a key consideration in the evaluation of long-term performance. Yet, to date, a comprehensive mechanical understanding of the effect wet environments on the corrosion process in closed systems remain elusive.

Corrosion under insulation (CUI) occurs when water is continually replenishing oxygen at a steel-insulation interface where the steel temperature ranges between -4 °C to 175 °C [28]. Another example is in the ballast tank where temperature could rise to 80 °C (in a car-carrier ship) due to the heat treatment effect [29]. The closed environment is a complex

process because it interfaces with several factors. Thus, each aspect and factor must be individually examined. When coatings are under insulation or in closed systems, various parameters can contribute to the degradation of organic coatings, such as dissolved oxygen, ionic species, temperature such as isothermal or cyclic conditions, and pH ranges.

The majority of studies have focused on model epoxy resins [30,32-33]. Little attention has been given to industrial systems, which typically comprise a complex mixture of resin and cross linkers with pigments, fillers and numerous additives. Typical additives have been shown to be hygroscopic, so that water uptake may be dependent on their concentration and distribution [34-35]. Furthermore, relatively few studies have reported kinetic investigations of the water uptake for epoxy-phenolic systems. Suzuki et al. [36-37] measured free volume for a range of epoxy-phenolic and found a direct correlation between free volume and water uptake. However, the effect of resin polarity was neglected. Conversely, Zhang et al. [24] examined two epoxy-phenolic systems and reported greater water sorption for the coating containing less free-volume.

So far, there is a lack in the demonstration and understanding of a phenolic epoxy coating, particularly commercial formulations regarding their ability to prevent corrosion in aggressive conditions such as high temperature (isothermal or cyclic conditions), corrosive salt such as seawater concentrations, and different pH levels.

1.2 Objectives

Based on literature review, there is a lack of understanding about phenolic epoxy coatings exposed to elevated temperatures. In particular, the effects of simultaneous immersion and condensation, mimicking a closed environment, on the coating behaviour have not been widely investigated. On this basis, the objectives of this study are set as follows:

1. Investigate the effect of immersion and condensation on corrosion behaviours of bare carbon steel.
2. Evaluate thermal degradation of a phenolic epoxy coating and its effects on the coating's performance.
3. Evaluate the post curing effects on the performance of a phenolic epoxy coating exposed to varying NaCl concentrations through immersion and condensation.
4. Study the effects of pH (alkaline/ acidic) on phenolic epoxy coating behaviour.

1.3 Thesis structure

This thesis is structured as follows:

Chapter 2 introduces literature review into electrochemical corrosion and a review of the causes of carbon steel corrosion, particularly in an enclosed environment. Corrosion products that form on carbon steel surfaces are discussed. Afterwards, detail on the types of coatings commonly used are given, with emphasis on the chemical properties and structure of phenolic epoxy coatings. Finally, factors that may contribute to the failure of organic coating in wet conditions and advanced methods for investigating organic coatings' protective properties and degradation mechanisms are explained.

Chapter 3 presents the experimental investigation into the influences of environment, i.e., immersion and condensation, on corrosion behaviour of carbon steel. The experimental design aimed to mimic an enclosed environment where multiple micro-environments concurrently exist. The study employed electrochemical techniques including electrochemical noise and electrochemical impedance spectroscopy to monitor corrosion behaviour. Key findings indicated that specimens immersed in a bulk solution at a constant temperature exhibited the highest weight loss and corrosion pattern was uniform. At the same time, carbon steel samples exposed to condensing conditions suffered localised corrosion.

Chapter 4 studied the effects of thermal exposure on the behaviour of a phenolic epoxy coating. The performance of the coated panels improved after thermal exposure at 120 °C for 40 d, as manifested by the high EIS impedance and increased adhesion force between coating and metal. The coating degradation was observed at 150 °C after 3 d by the appearance of cracks on the surface of coated panels.

Chapter 5 evaluated the roles of NaCl concentrations and pH on the performance of the selected phenolic epoxy coating, when exposed to water condensation and immersion in NaCl solution. Furthermore, the post curing effect was investigated by comparing the behaviour of fresh coating and pre-heated coating under the same exposure conditions. Degree of delamination and blistering were used to quantify the coating performance. Cross sectional analysis of the coating and corrosion products was performed to gain a better insight into the behaviour observed.

Chapter 6 summarises the achievements and limitations of this study along with some recommendations for the future work.

CHAPTER 2

LITERATURE REVIEW

2.1 Electrochemical corrosion

Corrosion refers to the degradation of a material caused by its interaction with the environment. Metal is particularly susceptible to corrosion owing to its low thermodynamic stability. During metallic corrosion, electrons, ions, and atoms are exchanged as the metal oxidises to a more stable oxidation state, known as the metallic oxide state [38]. In contrast, materials with lower electrical conductivity, such as polymers, degrade owing to a combination of physical alterations and chemical reactions, resulting in bond scissions and bulk material dissolution [39]. In this thesis, the term "corrosion" is used only to refer to the oxidation of carbon steel.

When iron is exposed to water or oxygen, an iron-oxide layer is formed on its surface. Initially, this layer is composed of goethite (α -FeOOH), lepidocrocite (γ -FeOOH) or a mixture of the two. This process occurs because of the following electrochemical redox reaction:



All redox reactions can be divided into two half reactions that occur simultaneously on spatially separable electrodes. The anode functions as the oxidizing electrode, and the cathode serves as the reducing electrode. An anode, a cathode, the electrical pathway between them, and a conductive medium (e.g. electrolyte) between them are sufficient to form an electrochemical corrosion cell in which the redox reaction occurs (Figure 2-1) [40]. To operate the electrochemical cell, a constant supply of electrons must be available and transferred to the electrochemical species, and ions must flow freely between the electrodes to maintain the neutrality of the system [41].

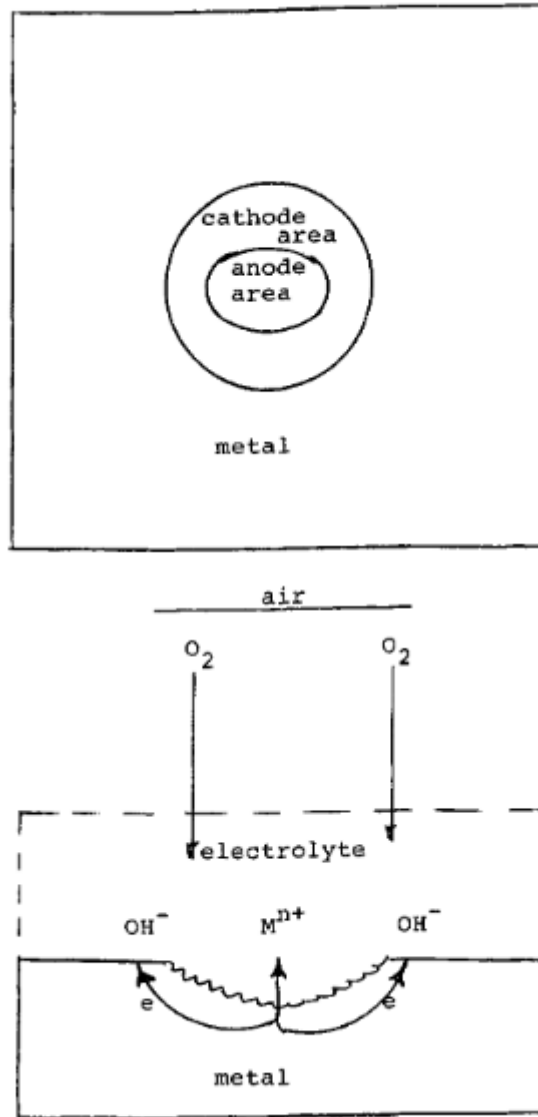


Figure 2-1: Electrochemical corrosion cell in top view and cross section [42].

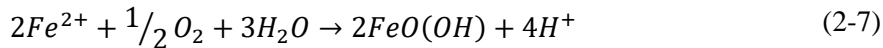
When metallic materials undergo corrosion, metal oxidation (Equation (2-2)) is usually the anodic reaction. However, the occurrence of cathodic reaction depends on the environmental conditions. In acidic and anaerobic conditions, the most common cathodic reaction is hydrogen evolution, while oxygen reduction is the most common reaction in aerated solutions [43]. Table 2-1 shows the potential cathodic reactions that can occur on iron exposed to various electrolytes (2-3) to (2-6). All of these reactions occur simultaneously on the metal surface but to varying degrees [44].

Table 2-1: The anodic and cathodic reactions that take place during iron corrosion.

Anodic reaction	Cathodic reaction	
$Fe \rightarrow Fe^{2+} + 2e^-$ (2-2)	$O_2 + 4H^+ + 4e^- \rightarrow H_2O$ (2-3)	Oxygen
	$\frac{1}{2} O_2 + H_2O + 2e^- \rightarrow 2OH^-$ (2-4)	reduction
	$2H^+ + 2e^- \rightarrow H_2$ (2-5)	Hydrogen
	$2H_2O + 2e^- \rightarrow H_2 + 2OH^-$ (2-6)	evaluation

The cathodic reaction (hydrogen evolution) is relatively slow in neutral and acidic media and does not remarkably contribute to the corrosion caused by the oxygen-reduction reaction [45]. Cox et al. demonstrated that as dissolved oxygen concentrations increase, the rate of corrosion initially increases, producing a predominantly granular form of magnetite (Fe_3O_4). At high oxygen concentrations, a passive film composed of ferric oxide is formed, which decreases the rate of corrosion. However, at low pH, hydrogen evolution tends to remove the passive film. The hydrogen evolution reaction considerably affects the composition, structure, electrical performance, and mechanical properties of the passive film and decreases its stability [46]

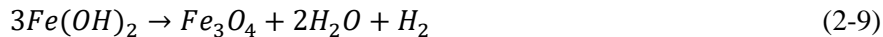
Once the iron has been dissolved, a few different reactions can occur. Under neutral aerobic conditions, dissolved iron ions can be oxidised to Fe^{3+} , which then precipitates out into amorphous iron oxide-hydroxides. Hematite ($\alpha-Fe_2O_3$) or maghemite ($\gamma-Fe_2O_3$) can also be formed by further crystallisation.



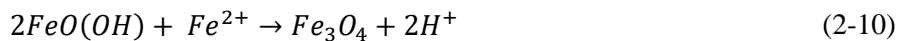
However, under anaerobic conditions, the following reaction can occur:



Although $Fe(OH)_2$ is unstable under these conditions, it can still react with other elements to produce magnetite (Fe_3O_4).



Fe_3O_4 can also be formed when dissolved oxygen is exhausted; this reaction increases the local acidity.



Under aerobic and anaerobic conditions, the oxide layers formed on the iron surface can reduce the rate of corrosion. The thickness and consistency of these oxide layers considerably depend on temperature, pH, and electrolyte composition [48].

The addition of sodium chloride to distilled, aerated water considerably increases the rate of iron corrosion. The chloride ions make the medium more conductive, allowing the current to flow between the anode and cathode areas that are far apart [45]. At room temperature, the rate of corrosion increases as the salt concentration increases and decreases if the concentration of NaCl exceeds 3.0 wt.% [49]. Iron corrodes faster when placed in a dilute NaCl solution because more of the dissolved oxygen can reach the cathode. However, if NaCl concentration exceeds 3.0 wt.%, the solubility of oxygen decreases and the corrosion rate goes down [49].

2.2 Corrosion in enclosed environments

Carbon steel can be immersed in condensed water in an enclosed environment. The oxygen content in condensed water is higher than in aqueous water; therefore, different corrosion processes may occur under these two conditions. Figure 2-2 shows the various types of corrosion that can occur on coated carbon steel in the enclosed spaces because of different environmental conditions. Ballast tanks are often in direct contact with sea water, moisture, and chloride ions. Therefore, among the various compartments of a cargo ship, a ballast tank is subject to the highest level of corrosion [50]. The corrosion patterns of ballast tanks are not uniform across the entire tank, and each region exhibits a distinct pattern. The distinctions are most evident in the empty section of the tank. In this section, the headspace is subject to condensation and is accessible to air and oxygen. Therefore, the rate of atmospheric corrosion is faster than the rate of corrosion in areas that are immersed in water ((Figure 2-2 a) and (Figure 2-2 b)) [51]. Figure 2-2c shows the normal corrosion distribution at the base of an insulated pipe and localised corrosion along the sides of the pipe.



Figure 2-2: Corrosion of carbon steel in enclosed environments; (a-b) inside a ballast water tank used to stabilise a ship [52] (c) under insulation [53].

Corrosion largely depends on temperature. As temperature increases, the kinetic energy of reactant molecules increases. The rate of corrosion typically increases with increasing temperature [54]. According to Fontana et al. [55], the corrosion rate of an enclosed system increases with increasing temperature as the oxygen is readily available. In contrast, the corrosion rate of an open system first increases with increasing temperature and then decreases as the temperature rises above $\sim 80\text{ }^{\circ}\text{C}$ as shown in Figure 2-3. The solubility of oxygen decreases with temperature, and the concentration of dissolved oxygen approaches

zero at 100 °C [5]. However, in closed systems, oxygen is confined in the gas phase at high temperatures, which increases its partial pressure. This in turn increases its solubility in water, thereby increasing the corrosion rate [56]. As documented in NACE SP0198 and API PR583, the most critical temperature range for preventing the CUI of carbon steel is 50–175 °C [56–57]. Moreover, the corrosion rate of the carbon steel increases with the temperature under insulation [57].

A ballast tank can be used as a heat exchanger with a freshwater cooling system. The maximum temperature of ballast water measured on board a car-carrier ship was 80 °C [58]. The temperature inside the ballast tank is 80 °C. This causes the water inside the tank to condense, which creates a humid atmosphere in the headspace of the tank.

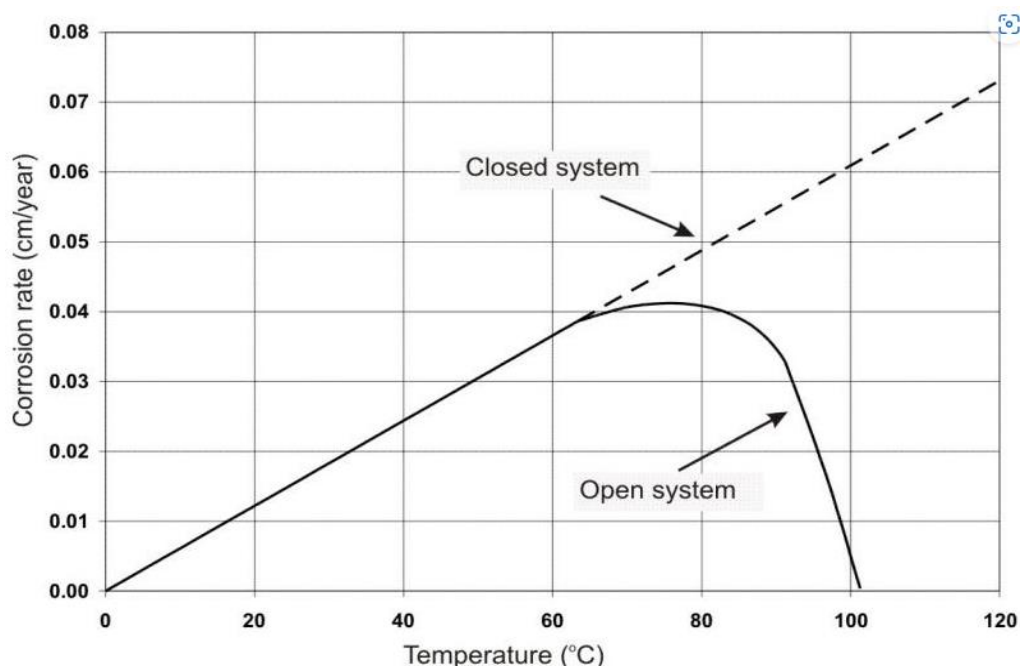


Figure 2-3: Effect of temperature on metal corrosion in water [5].

In closed systems, such as carbon steel under thermal insulation (Figure 2-4), water or moisture penetrates the insulation and becomes trapped between the insulation and jacketing. When evaporation occurs, the water cannot escape the closed system, and it condenses on the inner surface of the jacketing (water barrier). Water accumulates on the internal metal cladding and then migrates back to the hot surface [59]. Thus, it is plausible two distinct micro-environments are created within this closed system, the lowest part with a highly conductive electrolyte and the top section with a relatively lower conductivity from condensed water. Furthermore, in ballast tanks, owing to the cyclical charge and discharge of seawater as well as the motion of the ship at sea, regions exist where the electrolyte

concentration on surfaces above the water level has low concentration of Cl^- . Also, condensation occurring at the underside of the top surface.

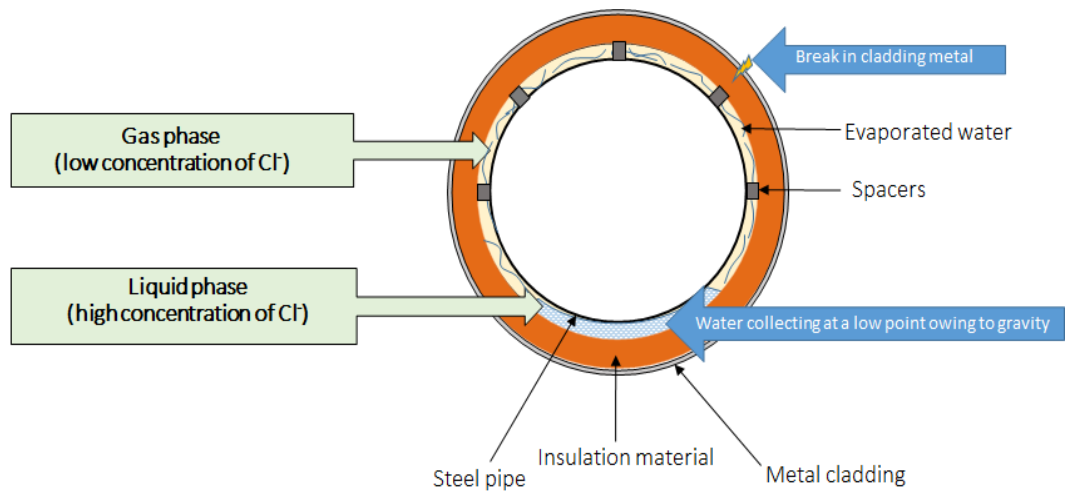


Figure 2-4: Cross-section of an insulated pipe with a breakage, describing water cycling in a closed system.

For carbon steel, the rate of CUI can be 20 times higher than that under naturally aerated atmospheric conditions when water or condensed moisture penetrate the insulation [60]. The CUI of carbon steel can be uniform or localised, whereas the CUI of stainless steel is mainly localised in the form of pits and stress corrosion cracking [61].

In addition, temperature plays a vital role in both anodic and the cathodic reactions. Figure 2-5 shows the polarisation curves for carbon steel in 3.5 wt.% NaCl at different temperatures (20–95 °C) [62]. These data clearly indicate that both the anodic and the cathodic reactions are enhanced at higher temperatures. The increase in the current corrosion rate (I_{corr}) of carbon steel corresponds to the decrease in the corrosion resistance of carbon steel with increasing temperature.

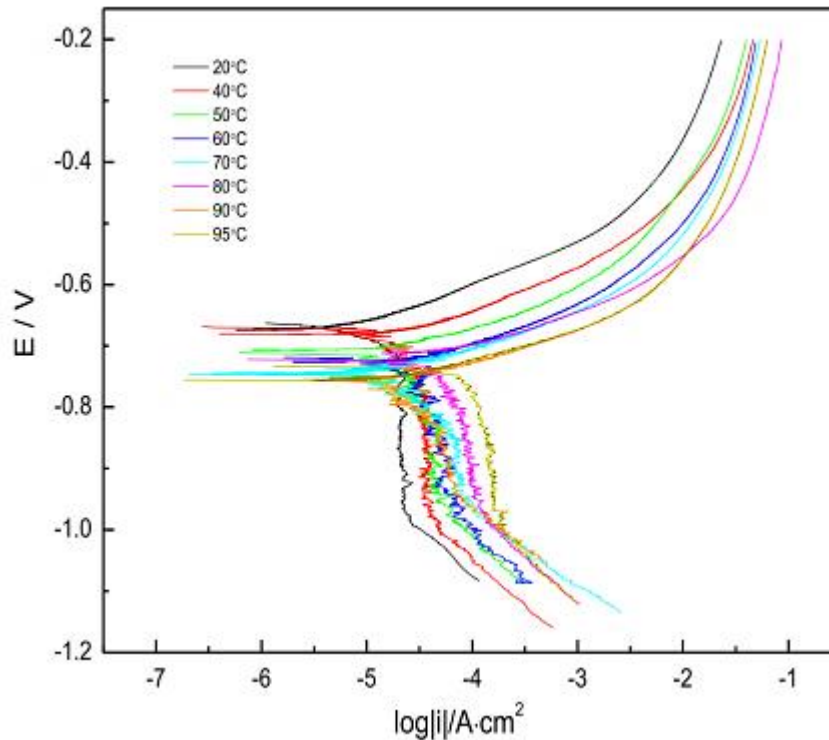


Figure 2-5: Potentiodynamic polarization curves of carbon steel in 3.5 wt.% NaCl solution at different temperatures [62].

Alkalinity typically decreases the rate of corrosion because the concentration of H^+ and the rate of hydrogen reduction decrease [63]. The pH of an electrolyte considerably depends on its external environment and can be affected by acid rain or condensation processes [56-57]. The pH of sea water ranges between 8.0–8.3. According to the ASTM C871 standard, the pH of an insulation material can be between 6–14 depending on its type as illustrated in Figure 2-6 [64]. The pH of water in the ballast tank of a ship during its voyage from the Baltic Sea to the open Atlantic Coast of Europe for 15 days was 7.34–8.17 [65]. The pH of the ballast water collected from container ships that travelled from Mexico to Japan was between 7.44–8.25 [66].

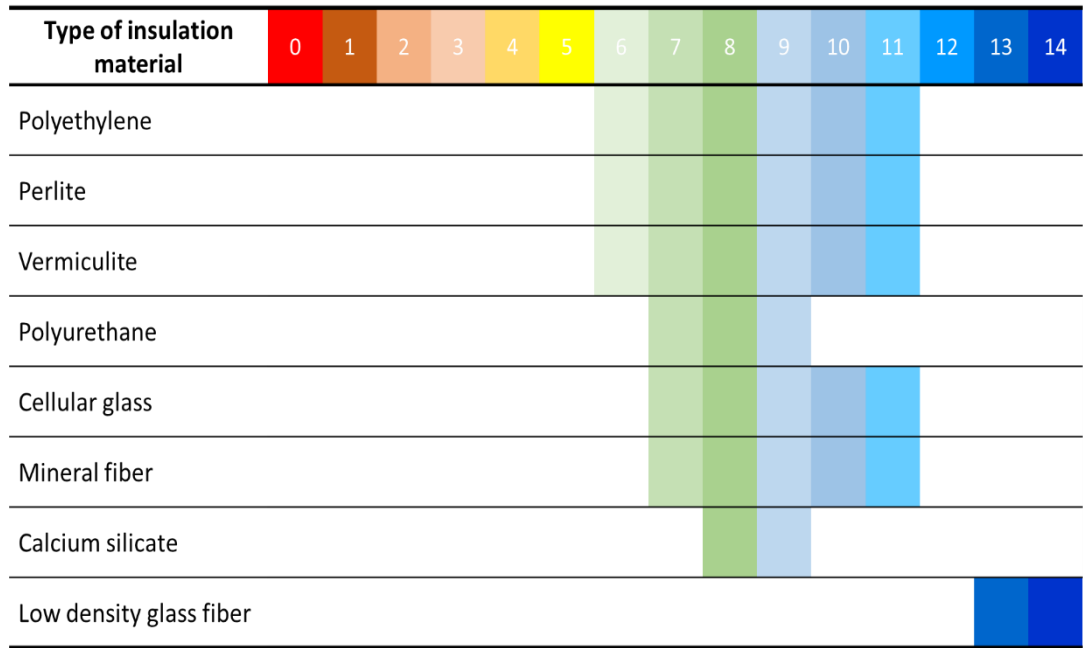


Figure 2-6: Level of pH for different insulation materials.

2.3 Protective coatings

Protective coatings are an effective way to reduce corrosion in humid conditions. Such coatings protect the metal surface from moisture [57] and prevent the infiltration of oxygen and corrosive electrolytes [67-69].

The following paragraphs introduce various types of coatings and their limitations. They also describe the standards that are used to evaluate the performance of the coatings.

Thermal spray aluminium (TSA) is a metallic coating that can be applied to process equipment, storage containers, and pipes. TSA has a service life of more than 25 years and offers a high degree of adhesion and corrosion resistance to the exposed steel substrate [70-71]. However, TSA needs to be closely monitored, as premature failures (as early as 8–15 years) have been reported, particularly in insulation systems [59]. Damage to the TSA coating on steel can accelerate its degradation, with a subsequent reduction in its service life [72].

Polysiloxane polymers (or high-build silicones) comprise synthetic compounds of repeating siloxane units and have excellent tolerance to high temperatures and ultraviolet radiation. Polysiloxane thermal coatings have been evaluated for CUI mitigation [73]. However, a second-generation polysiloxane coating exhibited blistering and cracking after exposure to CUI conditions and thermal cycling [73].

All coatings deteriorate over time, especially under wet insulation where moisture is trapped inside the annular space, resulting in water accumulation. Excessive water and

corrosive electrolytes can further corrode the metal substrate if the protective coating is damaged during use [74].

Researchers have used various test configurations to evaluate the coating performance under CUI conditions. For instance, a vertical pipe system was employed to investigate the coating performance under insulation. In this process, an insulated pipe was placed on a hot platform, and the coating performance was evaluated along the length of the pipe under a temperature gradient [75]. Furthermore, a high-temperature test apparatus was developed to investigate the coating performance on a square pipe under insulation [76]. In another study, a steam heating system and a test loop were employed to assess the performances of three different coatings (high-temperature inorganic copolymer, phenolic epoxy, and TSA) at 140 °C [60]. The results showed that the phenolic epoxy coating was the most effective among the tested coatings.

NACE SP0198 recommends that phenolic epoxy, novolac epoxy, and high-build epoxy should be used as thermal insulation coatings for metals [57]. Phenolic epoxy coatings provide protection against CUI over a long period of time in the temperature range of 3–150 °C [60]. However, these coatings may degrade during operation at temperatures outside this range or when exposed to excessive moisture with corrosive components and high pH [77].

Figure 2-7 gives a short summary of a few coating types currently used to protect the metals against corrosion at elevated temperatures. The organic coatings include benzoxazine, phenolic and novolac epoxies. These coatings provide excellent protection against water and salt damage but can degrade at high temperatures. The inorganic coatings include zinc silicates, which offer higher thermal resistance than organic coatings and can provide good corrosion resistance. Historically, these coatings have been used on insulated pipes with some success; however, they degrade prematurely in wet and hot conditions. At temperatures above 60 °C, zinc and zinc oxide have a very high dissolution rate, and under certain pH levels, the polarity between zinc and iron changes. Consequently, iron starts protecting zinc instead of the opposite, as intended. This results in the rapid degradation of the coating system and the corrosion of steel. Thin-film silicone is an inorganic silicate with excellent thermal properties. It does not possess the disadvantages associated with zinc silicates owing to the absence of the zinc pigment. Metallic coatings, including TSA, Si₃N₄ and zinc, have great anti-corrosive properties and are the optimal choice for long-term protection. However, these coatings are expensive and difficult to apply consistently, particularly in maintenance settings, making them unsuitable for many applications [78].

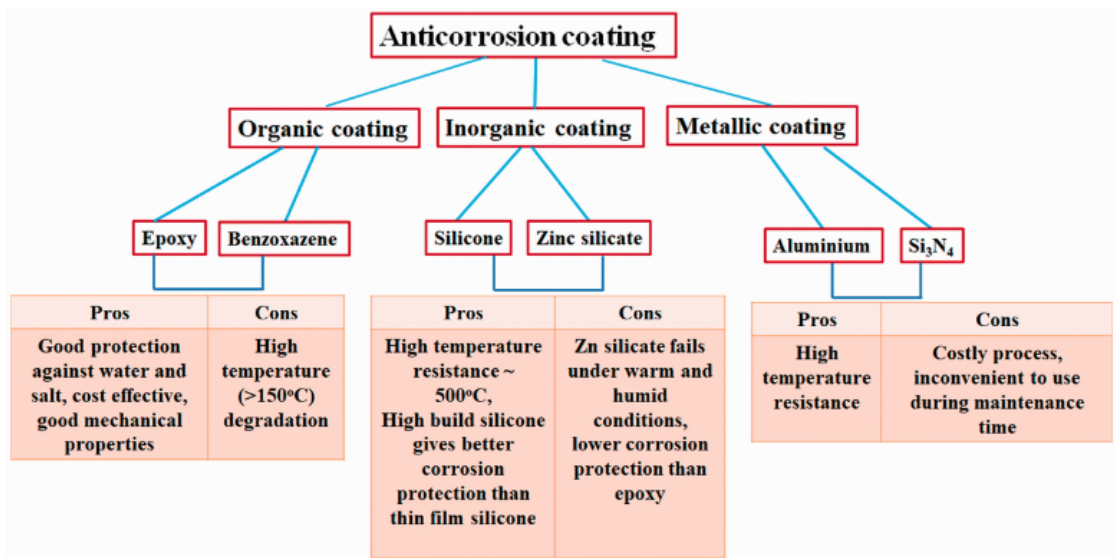


Figure 2-7: Some of anticorrosive coatings for protecting metallic materials against elevated temperatures [79].

A new methodology for assessing the structural integrity of coatings was developed by examining the morphology of blisters, cracks, and rust layers formed after corrosion [80]. A cyclic test plan that includes wet and dry tests, heating and cooling, and regular exposure to corrosive electrolytes such as, NaCl or $(\text{NH}_4)_2\text{SO}_4$ solutions, was designed to simulate inland industrial settings. This test plan is recommended as the most effective simulation method for evaluating the interactions between different environmental elements [81]. IMO PSPC [82], ASTM D5894 [83], proposed ISO 12944-6 [84], and modified NACE TM-0184 [85] are widely used standards to evaluate coated metal under cyclic weathering conditions. However, the issues regarding coating degradation in enclosed environments are still unresolved, and no agreements on standardised test apparatus for coating degradation in closed environments have been made.

2.3.1 Phenolic-epoxy coatings

In the early 1900s, Leo Baekeland first synthesized phenolic resins via the condensation reaction of para-phenylphenol with formaldehyde. Phenolic resins are classified according to the conditions used in their preparation. Figure 2-8 shows the chemical structure of novolac resins, which are prepared via condensation under acidic conditions. However, resole resins (Figure 2-9) are prepared via alkaline polymerisation (Figure 2-9). Phenolic resins are often combined with other resins, which increases their resistance towards acidic and salt solutions [86-87]. However, strong alkaline solutions can reduce their hardness by attacking their exposed hydroxyl groups [87-88]. The combination of phenolic resins and alkyds provides enhanced resistance against solvents [87].

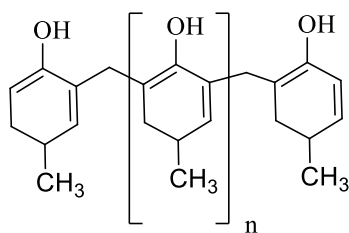


Figure 2-8: Chemical structure of novolac phenolic resin [89].

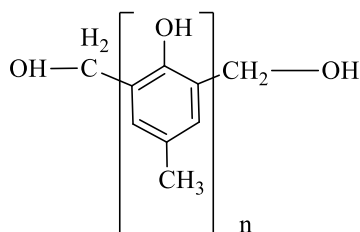


Figure 2-9: Chemical structure of resole phenolic resin (prepared from para-cresol) [89].

Figure 2-10 shows the condensation reaction between bisphenol-A and epichlorohydrin to form epoxy materials.

The reactivity of these materials is caused by the oxirane ring, which reacts with acidic and alkaline compounds to produce a thermoset resin through polymerisation. Polymer chains composed of diglycidyl ether of bisphenol A (DGEBA) are formed with diglycidyl ethers as end groups. Other potential epoxy sites that could be reactive are the epoxy hydroxyl groups, which have some steric freedom to bond with other polymer chains and form hydrogen bonds. The molecular weight (MW) of epoxy resins determines their state and viscosity. When the number of repeating units, $n=24$, the epoxy resin solidifies. In addition, epichlorohydrin can react with phenolic or polyhydroxy aromatic compounds to form novolac epoxies (Figure 2-11) [90-91].

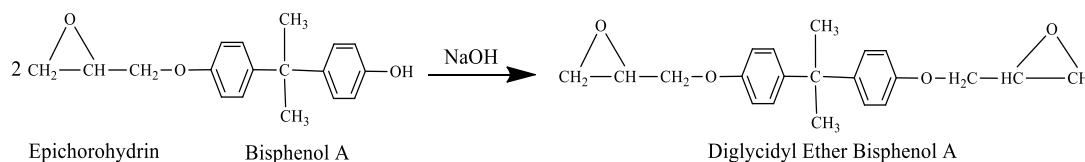


Figure 2-10: Chemical reaction of bisphenol-A with epichlorohydrin to form DGEBA [91].

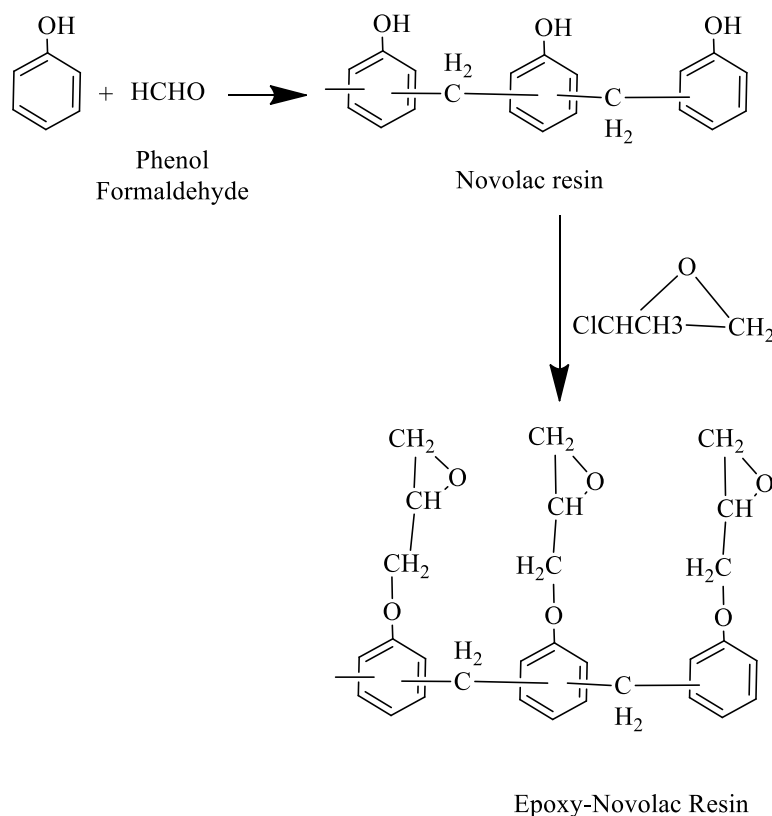


Figure 2- 11: Chemical reaction to form epoxy-novolac [91].

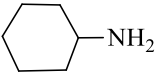
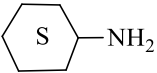
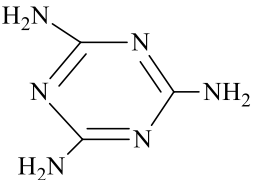
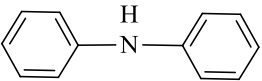
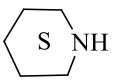
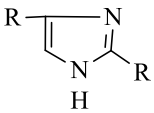
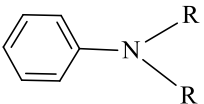
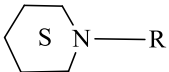
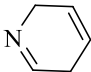
As the MW of the epoxy resin is increased, the chemical and solvent resistances increase, along with the flexibility and impact resistance [92]. Increasing the amount of phenolic resin improves the overall chemical and solvent resistance of phenolic-epoxy coatings while enhancing the flexibility and providing resistance to alkaline solutions [92].

Epoxy polymerisation can occur by heteropolymerisation or homopolymerisation reactions. Heteropolymerisation involves the addition of a hardener (curing agent) to the epoxy to form a macromolecular network. The efficiency of the hardener depends on the polymer curing or ageing conditions (temperature and time) [90-91]. Phenolic epoxy coatings are cured properly when exposed to a high dry temperature, as discussed later in this thesis. A stoichiometric amount of hardener is used so that the rate of the polymerisation reaction is maintained until its completion. However, some unreacted groups can become trapped between the macromolecules and adversely affect the polymer product [90]. The amount of hardener used determines the curing properties of the epoxy network. In contrast, homopolymerisation uses a catalyst that initiates polymerisation between resin monomers.

Amine compounds are widely used as curing agents for epoxy coatings. They provide rapid curing at room temperature (usually within 1-2 h), which is accelerated at higher temperatures [91]. The produced coatings have excellent electrical properties, chemical and

solvent resistance, and thermal and vacuum stability. These characteristics are improved when the coatings are postcured or cured at high temperatures. Amine compounds used to cure epoxies are categorized into twelve distinct types (Table 2-2). Aliphatic (straight chain) and aromatic amines react readily with epoxy resins, as shown in Figure 2-12, when the epoxy is cured using ethylenediamine [91].

Table 2-2: Formations of amine hardeners and catalysts [91].

Type	Aliphatic	Aromatic	Alicyclic	Heterocyclic
Primary	$R-NH_2$			
Secondary	$R-NH-R$			
Tertiary	$R-N(R)-R$			

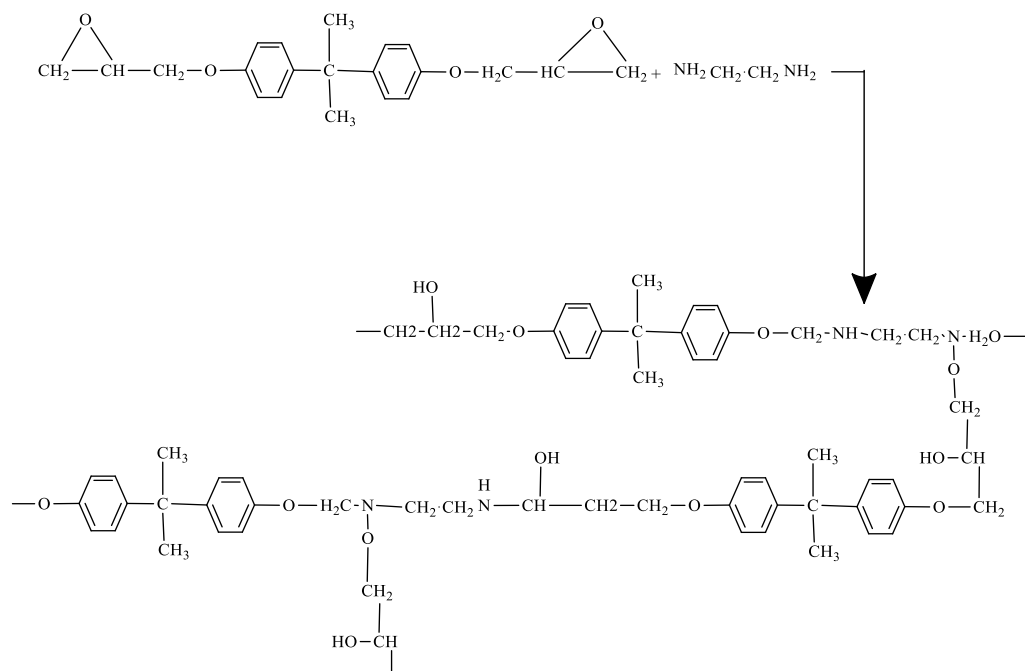


Figure 2-12: Cross-linking reaction between DGEBA and ethylenediamine [91].

In phenolic-epoxy systems, the density of the polymer is directly related to its glass transition temperature (T_g) [93-94]. Cross-linking is important because it also impacts the polymer packing coefficient (ratio of van der Waals volume to the molar volume of the structural unit) and free volume. The lengths of the DGEBA polymeric chains increased when it was cured with tetrafunctional metaphenylene. The amount of curing agent was increased according to its physical dimensions during thermal expansion [94]. A study on the relationship between functionalisation and mechanical properties in epoxies cured with diaminodiphenyl sulfone (DDS) revealed a direct correlation between the improved network structure and increased polymer strength [95].

The adhesion of epoxy resins can be attributed to the highly polar and surface-active epoxy molecules, which form chemical bonds and allow mechanical interlocking with the substrate. The numerous ether bonds in epoxy resin and their available electron pair (from oxygen atoms) allow for hydrogen bonding between the coating and the metal substrate [91]. The aromatic ether moieties in the epoxy resin form stronger hydrogen bonds because the oxygen in the resin is more electronegative [91]. Moreover, the hydroxyl groups of the epoxy resin provide hydrogen atoms that bond together. Each hydrogen bond has a force of attraction of ~5 kcal/mol; therefore, the adhesive force between the epoxy coating and the substrate is strong [91].

2.3.2. Permeation of corrosive species through organic coatings

Organic coatings protect metal surfaces by providing a physical barrier to the diffusion of water, oxygen, and ions that lengthens diffusion pathways of corrosive species between the environment and metal surface [96]. Electrochemical reaction under a coating can only occur if there is sufficient penetration and accumulation of water and oxygen at the substrate/coating interface to enable the cathodic oxygen reduction reaction to occur [97]:



However, these coatings consist of networks of polymer chains with associated free-volume, pores, and defects. The porosity and defects can form channels for the transport of corrosive species to the metal surface, which can decrease the resistance and barrier properties of the coating and ultimately lead to adhesive failure [97].

2.3.2.1 Water transport through coatings

Water can permeate a coating by three mechanisms: (1) a concentration gradient of ions is created upon immersion in an aqueous solution or exposure to high relative humidity, resulting in true diffusion through the polymer; (2) osmosis due to impurities or corrosion products at the interface between the metal and coating; and (3) pores and defects in the coating formed by poor curing, improper solvent evaporation, poor interaction between binder and additives, or entrapment of air during application enable diffusion by capillary action [97-98]. The permeation of water through the coating and subsequent accumulation at the substrate-coating interface can lead to adhesion loss, blister formation, and pathways for ionic transport. It was demonstrated that water transport through a substrate-organic-coating interface could be approximately two orders of magnitude faster than that through a bulk coating, although hydrated ions have similar transport rates at the interface and coating [98-99].

The coating capacitance is crucial for determining the water barrier properties of an organic coating [100]. Moreover, it can be used to evaluate the volume fraction of water in the coating and the kinetics of water uptake [101]. Figure 2-13 shows that there are three distinct stages of water uptake: (1) homogeneous diffusion of water into the coating, (2) a steady-state plateau of little-to-no water uptake (coating saturation), and (3) a further increase in water uptake due to local bulk water accumulation and swelling [102-103]. Swelling of the coating can then lead to adhesion loss, blister formation, and corrosion reactions at the substrate-coating interface.

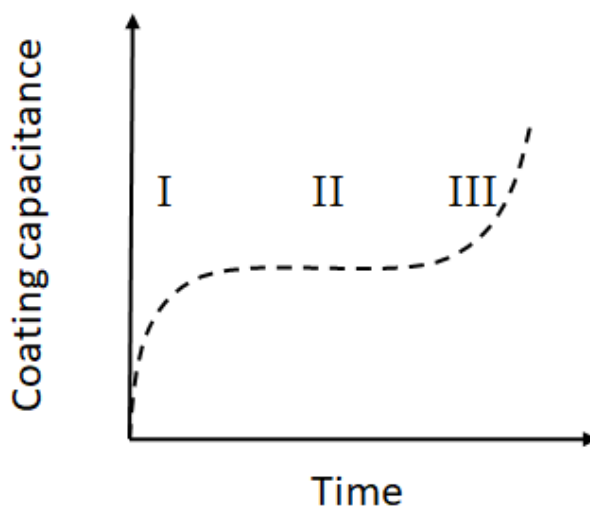


Figure 2-13: Trend of capacitance vs. time in an aqueous solution [103].

Numerous studies have investigated the penetration of water into coatings [102-104]. Initial studies on water uptake used single-layer systems and AC measurements to determine the changes in coating capacitance and the water uptake by coating [102]. Other studies investigated coating systems with two organic layers (primer and topcoat), each with a distinct role, swelling behaviour [105-106], hydrolysis properties [107], and effect on lowering of T_g [108-109]. It was reported that the quality of the interface between the two organic coatings greatly influences the impedance of the system [110]. Later, the in situ wetting and drying behaviour of a primer–top-coat interface was evaluated by EIS using embedded electrodes and a two-layer model was developed [111]. It was confirmed that the assumptions generally applied to single-layer systems do not hold for the primer–top-coat interface.

2.3.2.2 Oxygen penetration

Oxygen is a key component in the oxygen reduction reaction shown by reaction (2-11) [112]. The primary mechanism of oxygen transport is diffusion through pores and defects in the coating [96]. However, as in the case of water, oxygen can also permeate through dense coatings due to the free volume of the polymer. In contrast to water, oxygen does not interact as readily with the polymers in the coating during transport to the interface. Negligible swelling or rearrangement of the polymer chains occurs during oxygen transport. Therefore, oxygen diffusion is primarily due to the properties of the polymeric structure, such as the polarity, degree of cross-linking, and T_g . A hydrophilic polymer can limit oxygen permeation by promoting hydrogen bonding, which can enhance the crystallinity and dense packing of the structure. It has been shown that the addition of polar groups to a hydrophobic backbone can significantly decrease oxygen permeability [96,113-114]. Similarly, cross-linking can limit oxygen diffusion by decreasing the polymer chain mobility and increasing the MW [96].

Finally, as T_g increases, the free volume of the coating decreases, thereby reducing the oxygen diffusion rate.

2.3.2.3 Ionic transport

For corrosion to occur under a coating, there must be an electrochemical double-layer (build-up of ionic species) at the metal surface [112]. It has been shown that the diffusion rate of ions through an intact coating is small due to the low dielectric constant of the coating [115]. During the initial stages of water penetration through the coating, ionic transport is limited to the ionization of fixed polymeric groups that allow for the transport of oppositely charged ions. As water penetration substantially increases, the dielectric constant of the coating increases, creating pathways for hydrated ions to the substrate–coating interface [115-116]. Therefore, any ionic species present at the substrate–coating interface before primer application cannot diffuse away from the interfacial region and may exacerbate corrosion [117].

2.3.3 Adhesive failure

A coating system must adhere well to the metal substrate to provide adequate protection. It was postulated that the degree of corrosion protection provided by a coating depends more on maintaining adhesion at the substrate–coating interface than providing a physical barrier [118]. Adhesion can be achieved through five mechanisms: (1) mechanical interlocking, (2) chemical bonding, (3) electrostatic effects, (4) adsorption, and (5) diffusion [119-120]. The primary adhesion mechanisms for organic coatings on metal surfaces are mechanical and chemical bonding.

Mechanical adhesion involves the interlocking of the coating with surface irregularities provided by a rough substrate surface [90]. With an absence of surface roughness, interfacial attractive forces are the only forces binding the substrate and coating. With the addition of surface roughness, the coating fills the indentations and hence, the substrate or coating material must be broken for delamination to occur. In addition, surface roughness increases the surface area available for bonding, which requires that more bonds are broken upon delamination. Therefore, the adhesion strength increases with increasing surface roughness. However, the coating must be able to fully penetrate all of the undercuts in the substrate, otherwise, corrosive species can accumulate and attack the bare substrate upon permeation through the coating [121].

Chemical adhesion is primarily based on the bonding between the polymer chains in the organic coating (polar group) (R–OH) and the hydroxide layer on the steel surface (Me–OH). The latter is part of a thin oxide–hydroxide passivation layer formed on the metal surface

due to environmental oxidation, which is a polar (hydrophilic) layer [122]. When an organic coating is immersed in an aqueous solution or exposed to high humidity, the most common failure modes are poor wet adhesion [98,121], blistering [123], and filiform corrosion [118,124]. The primary method for minimising failure under humid conditions is to reduce the relative humidity, although this is not always simple or practical.

2.3.3.1 Wet adhesion loss

Wet adhesion loss refers to the loss of adhesion between a metal substrate and coating in the presence of an electrolyte or water, without the formation of a blister [98,119,121]. Leidheiser and Funke refer to wet adhesion loss as “water disbondment” to emphasise the loss of adhesion including water vapour as an additional factor [125]. Current knowledge of the effects of water accumulation at the substrate–coating interface is based on the work of Haagen and Funke [126], who proposed that water permeating through a coating could cause delamination of the coating, which is defined as poor wet adhesion [121]. The permeation of water into a coating only results in corrosion of the underlying metal if the coating delaminates from the substrate [90,122,126]. Wet adhesion loss occurs when the attractive forces between the substrate and water or between the coating and water are stronger than the adhesion force between the substrate and coating [98], resulting in the displacement of the coating [119,127]. Figure 2-14 shows the chemical bonding occurring at the substrate–coating interface under dry and wet conditions. Furthermore, the debonding process is not instantaneous and there are intermediate stages in which wet adhesion loss can be partially recovered if the coating is dried [119,122,128].

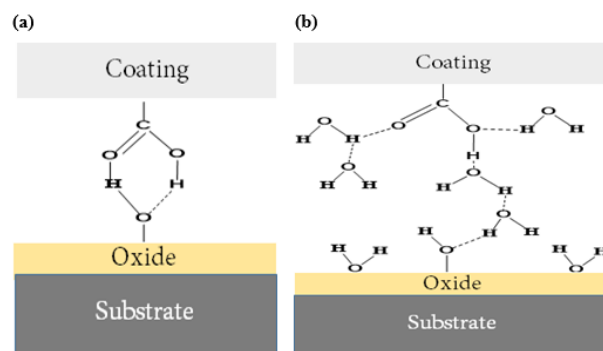


Figure 2-14: Schematic of the substrate–coating interfacial bonds under (a) dry and (b) wet conditions. Adapted from [119].

In 1987, Leidheiser and Funk [125] confirmed that wet adhesion loss is a consequence of a continuous or discontinuous water layer at the substrate–coating interface. Water permeates through the coating and gathers at the interface. In support of Haagen and Funk [126], the authors stated that water accumulation requires local areas where the substrate and

coating are not well bonded. Finally, they noted that the water layer grows laterally due to stress associated with water condensation.

The mechanical properties of a polymer, such as its T_g , determine the quality of a polymer coating and must be considered in both dry and wet conditions [129]. It was shown that to achieve a high-quality coating system, the layer adjacent to the substrate should have a T_g above ambient temperature. If the T_g of the polymer is too low, the high chain mobility facilitates the sliding of adhesive bonds at the substrate–coating interface and displacement of the coating in the presence of water.

2.3.3.2 Blistering

Blistering is considered a crucial coating failure mode for steel systems [130]. It is the first visible sign of failure of an organic coating immersed in an aqueous solution or exposed to high humidity and indicates insufficient corrosion protection [123]. Upon water uptake and subsequent swelling of the coating, localised coating delamination can occur along the substrate–coating interface. Absorbed water then accumulates at the delamination sites to form a blister. There are two primary mechanisms of blister initiation, although others have been suggested: (1) osmotic pressure at the interface and (2) mechanical stresses. The former refers to the chemical activity of water above and below the coating, where the difference is typically caused by atmospheric contaminants or residual salts at the interface that lower the water activity. Water transport is driven by the difference in chemical potential between the outside coating surface and internal blister surface [131]. Van der Meer-Lerk and Heertjes showed that the accumulation of salt at the interface dictated the formation of blisters [132]. The osmotic pressure mechanism is considered to be the most significant and should be accompanied by an associated visible release of internal pressure upon rupture. However, in practice, no visible release of internal pressure has been observed [123]. It was proposed that instead, this process should be thought of as continual build-up and release of pressure, which supports the lack of a noticeable pressure release. In addition, absorbed water at the interface can produce mechanical stresses (compressive stress inside a blister and tensile stress outside the blister) that stretch the interfacial bonds between the substrate and coating. This stress can form blisters, especially at weakly adhered points along the interface. However, this mechanism is frequently criticised. It was suggested that the mechanical stresses from small amounts of absorbed water are probably relieved before blistering [123].

Coating applications should meet the minimum industrial requirements for substrate surface preparation and the specified wet-film and dry-film thicknesses, which are essential for ensuring appropriate coating performance. A coating will not provide its intended service life if it is applied over salt/ corrosive medium due to contamination (lack of surface

preparation). The adhesion strength between the coating and substrate may decrease if the substrate surface is not adequately prepared (Figure 2-15). Surface contamination decreases adhesion and create initiation points for osmotic gradients associated with soluble salts in the bulk solution, resulting in the degradation of the coating [145].

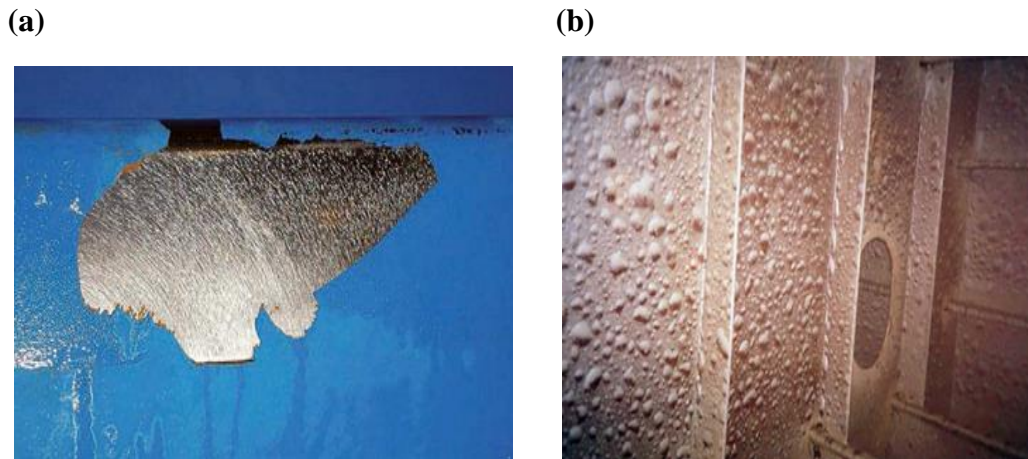


Figure 2-15: Coating degradation in poor surface preparation. (a) Adhesion failure of the coating result of surface contamination. (b) Blistering on the coating caused by chlorides ions on substrate surface prior to metal coating [133].

2.3.3.3 Filiform corrosion

Sharman [134] was the first to study “filiform corrosion” in 1944. Sharman observed this phenomenon under coatings on steel substrates and noted that it spread quite rapidly (~2.5 cm per month). Filiform corrosion is characterised by the development of filaments with an “active head” filled with liquid and a “tail” of solid corrosion products that lifts and penetrates the organic coating [118]. Corrosion occurs in the active head, while the tail is thought to be inactive, although, there is no distinct boundary between the two regions [135]. Filiform corrosion is initiated at defect sites in the coating, such as scratches, edges, and areas of adhesion loss. Water and oxygen are necessary components for the oxygen reduction reaction to occur. Finally, there must be an aggressive ionic environment, where chlorides enhance filiform corrosion. Figure 2-16 shows a filament travelling across the metal substrate with the filament head acting as an anode and the filament tail acting as a cathode. The driving force for this type of growth is believed to be an oxygen gradient cell between the anodic head and cathodic tail [118].

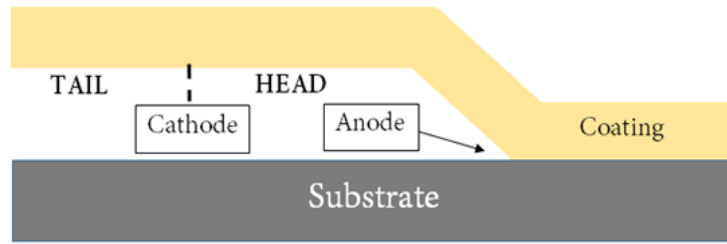


Figure 2-16: Schematic of the structure of a filament in filiform corrosion [136].

In 1959, Kaesche proposed a mechanism to describe water and oxygen transport to the active head through a mass-transfer pathway in the porous tail [136]. It was observed that oxygen was prevalent at the back of the active head, but no verification of this hypothesis was given. In 1983, Ruggeri and Beck [135] experimentally confirmed the mechanism proposed by Kaesche [136]. By cutting the filament tail, peeling back the coating, and closing off the part of the tail emerging from the surface, the corrosion process was effectively terminated [135]. Similarly, when the pathway was reopened, the corrosion process started again.

2.3.3.4 Cracking failure of coating

Cracking failure occurs when a dry coated film begins to degrade before its expected life span due to the formation of cracks on one or more coating layers.[137]. Cracking is the term used to describe damage to the coating during operation. Generally, it is caused by various product and material factors such as an excessive film thickness, which results in film shrinkage due to excessive application, poor product formulation, inadequate application intervals, and incorrect surface preparation [138-139]. Cracking is an undesirable characteristic of the protective coating due to embrittlement or the loss of flexibility of the coating as it ages.

Ringsberg et al. [140] investigated the rate at which coatings disintegrate after they were applied to steel substrates. They used a four-point bend test on two coatings to determine the loss of flexibility with ageing. They wanted to find out if there was a way to measure how long coatings last over time. They suggested that cracking is caused by the stress produced inside the coating because of environmental factors, such as changes in temperature, water exposure, and wet and dry cycling. [140].

Organic coatings are often used in ballast tanks to prevent corrosion [16]. The limited literature on ballast tank coating, particularly on coating failure assessment, makes this a difficult subject area. Cracking failure is a common occurrence in ballast tanks. [141]. According to Mills and Elliasson [142] the deterioration of the coating in the ballast tank from

both wet and dry cycling (mechanical fatigue) leads to a decrease in the protective efficacy of the coating.

Dei et al. [143] confirmed that cracking in epoxy coatings on the ballast tank surface occurs because of stress due to temperature variations.

Zhang et al. [144] proposed that the deterioration of the epoxy-based coatings resulted from the accumulation of thermal stress during the ballast operation. In addition, they confirmed that the performance characteristics of coatings largely depend on the environment in which they are applied (in-service environment). The cohesive strength of the coating decreases as the immersion period increases; hence, the breaking of hydrogen bonds due to water results in the degradation of the coating.

Ringsberg [145] stated that thermal fatigue caused by corrosive conditions (e.g. seawater) may considerably damage ballast tank coatings. Therefore, it is important to emphasize that the combined effects of seawater and temperature may increase the likelihood of cracking failure.

Pederson et al. [78] evaluated the performance of various coatings, including organic epoxy and inorganic silicone, under insulating conditions. The coated panels were subjected to a range of temperatures, spanning from 300 °C to 650 °C, for a 24 h duration at each temperature level. Subsequent to each thermal cycle, the panels were inspected for the presence of cracks. Extensive micro-cracking was observed in thin-film silicone after 18 d of exposure to 650 °C. High-build silicone exhibited its first signs of cracking at 300 °C. Novolac epoxy developed cracks after 9 d when exposed to a temperature of 250 °C. Failure in the form of cracks in epoxy mastic material was noted at 200 °C after a 20 d exposure period.

2.4 Typical methods for investigating protective properties and degradation mechanisms.

2.4.1 Surface characterisation methods

2.4.1.1 Time of flight–secondary ion mass spectroscopy

This technique analyses the secondary particles emitted from a target surface bombarded by primary particles, i.e., ions, electrons, neutral atoms, and high-energy photons (usually between 1–15 keV). Most emitted particles are neutral. Secondary ions can be positively or negatively charged and are analysed using mass spectrometry. The fragment peaks of the spectrum may be characteristic of the substrate material itself, materials adsorbed on the substrate, or surface contaminants and impurities. Figure 2-17 illustrates the sputtering process in a schematic manner [146].

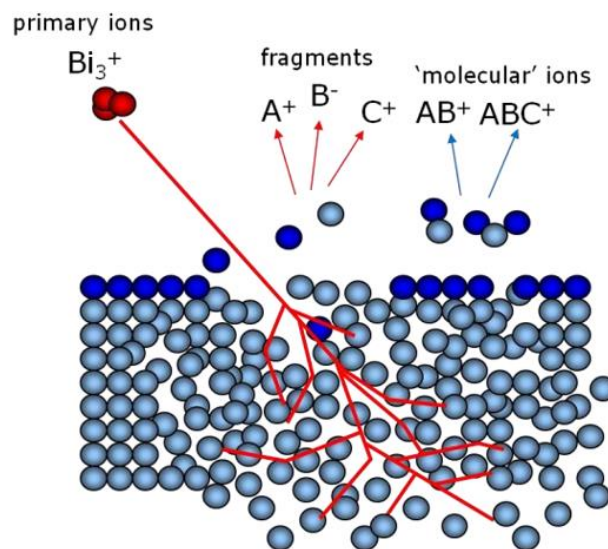


Figure 2-17: Schematic of the SIMS process.

There are three different mechanisms by which secondary particles are released from the surface after impact by a primary particle, which depend on the particle energy. (1) Single knock-on (or collisional sputtering) occurs when the energy of the particle is lower than 1 kV and the current flow is also low. After primary-particle collisions, if the atom/particle has enough energy to overcome the surface binding, it is released from the surface. (2) If the energy and current are high enough, an internal flow of moving target atoms passes through the sample surface, which causes a linear cascade or "collision sputtering". (3) A spike regime (thermal sputtering) occurs at a high degree of electron excitation. Figure 2-18 shows the schematics of the sputtering processes involving elastic collisions [147].

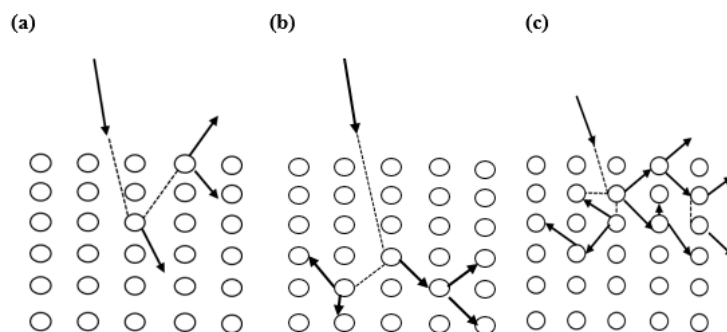


Figure 2-18: Schematics of sputtering by elastic collisions. (a) Single knock-on regime, (b) linear cascade regime, and (c) spike regime.

Spectrometry can be conducted in either static or dynamic modes. Static secondary ion mass spectroscopy (SSIMS) is operated at a lower incident primary-beam current density than dynamic SIMS (DSIMS). In SSIMS, the typical current flux is below 1 nA cm^{-2} . There is very little damage to the surface at chemically sputtered. DSIMS, on the other hand, uses a much more intense primary-beam and etches the sample surface, causing a lot of surface damage. The emitted particulate is continuously determined as a ratio to the depth of the original surface. DSIMS usually only looks at atomic ions. However, there are other methods like SSIMS or DSIMS used for different types of analysis. The main use of SSIMS is to determine the chemical composition of a surface and it's useful for surface science, like adhesion studies. It is also the most widely used for organic material analysis. DSIMS is widely employed for chemical composition analysis as a result of depth (several hundreds of monolayers) because of its etching ability.

SSIMS has proven to be an effective tool for analysing organic materials. These organic materials are chemically bonded, and the primary collision energy is converted into molecular vibrations, resulting in energy exchange within the organic layers through vibrational excitation. SIMS systems mainly consist of a primary ion source and a mass analyser [147], as described in the following sections.

2.4.1.1.1 Primary ion sources

The primary ion beam produced by an ion gun has an ionic energy of 1–15 keV. The ion beam bombards the sample, resulting in the emission of secondary ions via the processes described above. In SIMS, especially SSIMS, an electron-impact ion source is used for analysis. Electrons are generated from a hot filament to provide sufficient energy to ionize the source gas. The primary beam typically comprises caesium (Cs^+) or bismuth (Bi^+) ions. An electrostatic or magnetic field controls the beam. Bi^+ sources with small spot sizes (200 nm) and low beam current (1.1 pA) are used for ToF-SIMS analysis [148].

2.4.1.1.2 Mass analysers

In the case of SIMS, it is essential to obtain the maximum amount of information from a surface. To detect the total yield of secondary ions produced from the surface, the detection system should be optimised. SIMS uses three types of mass analysers: quadrupole, magnetic sector, and ToF [148].

Quadrupole mass analysers operate by applying a direct current (DC) and an alternating current (AC) to four adjacent rods. As the ions pass through the analyser, they are separated by weight. An electrostatic filter is inserted between the sample and the analyser because ions with high kinetic energy cannot be separated. The analyser only permits the transfer of ions in a sequential manner and analyses the target ions in the range of low to high molecular weights [148].

Magnetic sector analysers are typically employed for DSIMM, i.e., depth profile analysis, which is usually combined with imaging. A fixed potential is applied to the ions prior to their entry into the magnetic field. The separation of the ions is determined by their mass to charge (m/z) ratio. The mass resolution depends on the size of the magnets. This analyser has a high transmission resolution and a high mass detection rate. However, it has several limitations, such as slow mass scanning speed and difficulties in generating a true ultrahigh vacuum [148].

ToF mass analysers are suitable for analysing complex organic materials that require a high mass range. ToF analysers are better than magnetic sector analysers because they have better mass resolution, transferability, and sensitivity. The ToF value is directly proportional to the m/z value of the ions, and the mass spectrum is plotted as intensity versus m/z .

2.4.1.1.3. Detection of hydrocarbon polymers

The secondary ion spectra of aliphatic polymers comprise signals from $C_nH_m^+$ clusters, with $m = n \dots 2n+1$. Compared to saturated polymers, there is a greater weighting of the C_n clusters of ions containing more hydrogen atoms. The $C_nH_m^+$ clusters extend to a much higher mass (m/z), which indicates the MW of the polymer chain structure [149].

Yiu et al. [150] examined the surface characteristics of liquid polymers to detect hydrocarbon segments. The mass spectrum of the polymer surface enriched with $C_xH_y^+$ was measured. The hydrocarbon group fragment obtained at the end was $C_{11}H_9^+$.

Treverton et al. [151] identified certain elements of epoxy coating using ToF-SIMS. The study focused on the chemistry and molecular structure of epoxy resins. High-molecular-weight epoxy resins comprise oligomers composed of glycols and phenols.

The curing process of epoxy resin depends on the composition and concentration of the hardener. Firas et al. [152] investigated the curing reactions of epoxy resins by studying the $C_xH_yN_z^+$ ions observed in the mass spectrum of cured resin samples. When the concentration of the aliphatic hydrocarbon hardener ions is higher, the crosslinking density of the resin increases.

2.4.1.2 Raman spectroscopy

Raman spectroscopy was used to investigate the corrosion mechanism under the coating and to identify the iron oxides in the corrosion layer beneath the polymer. Raman spectra of typical iron oxides have been published in the literature and can be used as reference spectra [153-154]. The highest frequencies for different oxides are shown in Table 2-3. These frequencies are based on the spectra of samples recovered from the field. All peaks were matched with those of iron oxide standards. The Raman spectra was interpreted in terms of peak intensity ratios, shape, and frequency. It is possible that hematite and maghemite may be formed from other iron oxides due to heating from the Raman laser; therefore, the laser power was adjusted to reduce the damage.

Table 2-3: Characteristic Raman wavelengths of various iron oxides [153-154].

Raman Frequencies	Feature	Oxides
136-147	Sharp	Akaganeite, Goethite
247-250		Goethite, Lepidocrocite
298-300		Goethite
305-320		Akaganeite
380-400		Akaganeite, Goethite, Lepidocrocite
408-415	Shoulder	Akaganeite
470-480	Weak	Goethite
495-502		Ferrihydrite
510		Green rust
529		Lepidocrocite
532-540	Weak	Akaganeite
545-552		Goethite
667-690	Broad	Goethite, Magnetite
710-725	Broad	Akaganeite, Maghemite

De Faria et al. used Raman spectrometry to study corrosion [155]. Corrosion products of steel when immersed in 0.5 M H₂SO₄ borate buffer (pH = 8.4) and in carbonate/ bicarbonate buffer (pH = 8.9) solutions, iron oxy hydroxides, goethite and lepidocrocite were found [164].

According to numerous research papers, corrosion products typically consist of several layers of iron oxide [86,156-159]. Over time, rust accumulates in layers, and the composition of rust can vary depending on the environmental conditions (e.g. atmosphere, aeration) [160]. In addition, material composition with other corrosive parameters such as chloride ion content, pH, and temperature affects corrosion products [161]. For example, Xin Zhang identified that lepidocrocite (γ -FeOOH) is found in the outer layers exposed to the environment. At the same time, goethite (α -FeOOH) or magnetite (Fe₃O₄) formed in the inner parts, and the thickness of layers depended on the corrosion conditions [162]. Earlier studies by Reguer and coworkers [163] investigated the chloride containing corrosion products. Earlier study by S. Savoye et al. observed through Raman spectroscopy analysis that corrosion products had two layers when exposed to carbonate and oxygen. The inner layer comprises α -FeOOH, while the outer layer forms Fe₂O₃ and Fe₃O₄ [161].

2.4.1.3 Fourier-transform infrared spectroscopy

The chemical and physical behaviour of a coating system must be clarified so that predictions can be made regarding the subsequent properties of the protective coating. Fourier-transform infrared spectroscopy (FTIR) is used to study the chemical bonds initiated under processing conditions that affect the final coating properties [164]. Figure 2-19 illustrates that infrared radiation is generated from a source and travels through an aperture that modulates the irradiance of the sample. The beam passes through an interferometer that converts it into a special signal that contains all IR frequencies. The beam finally reaches the detector, where the final signal is detected and converted into digital data that is then sent to the computer for spectral processing. The resulting spectrum provides information on the chemical bonds of the sample, e.g., an organic coating, to identify changes in the bonds as a function of the experimental/environmental conditions [153].

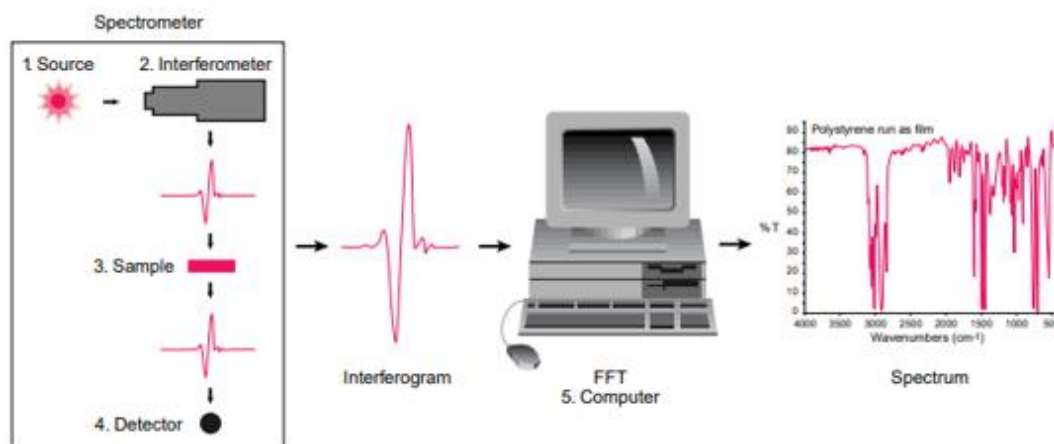


Figure 2-19: Schematic of the working principle of an FT-IR spectrometer [165].

Webb carried out the depth profile studies of solid organic films to measure the time and surface depth of the obtained infrared spectrophotometric data [166]. Hill [167] studied the degradation of plasticized poly(vinyl chloride) using IR spectroscopy. The samples exposed to ultraviolet radiation and natural weathering yielded degradation manifest by absorption bands at 3200 (OH), 1400 (C-H bending), and 1720 cm^{-1} (C=O). The band in the 3700–3100 cm^{-1} range is attributed to the presence of OH groups (from hydrolysis products, alcohol residues, and absorbed water) [168-170] and primary and secondary N-H groups that absorb in this region [171-173]. The bands at 2931 and 2870 cm^{-1} are assigned to the C-H stretching vibrations of the alkyl groups [168-170] and N-H vibrations [171]. The intermediate band at 1640 cm^{-1} is attributed to the bending vibration of water molecules absorbed by the coating [172,174]. The band near 1600 cm^{-1} , more notorious in the high amine cured coatings DETA (1:1) and 3A (1:1), can be assigned to N-H deformation modes in the $-\text{NH}_2$ group, indicating that a small amount of the crosslinking agent remained unreacted [171-172].

2.4.1.4 Thermal analysis

Thermal analysis techniques are employed to determine the correlation between temperature and particular physical characteristics of a material [175]. The thermal methods used in this study were DSC (Differential Scanning Calorimetry) and TGA (Thermal Gravimetric Analysis).

DSC applies a linear temperature ramp to a sample to obtain quantitative calorimetric information. In polymer research, the T_g is obtained from DSC data, which gives information about the mobility of the polymer chains [176]. A polymer state is rubbery above T_g and glassy below T_g [175]. Moreover, a higher T_g indicates a higher cross-link density of the polymer and lower segment mobility.

TGA measures the mass of a polymer sample during heating [177]. Polymers typically lose mass when subjected to a slow rate of heating at low oxidation temperatures [178].

The mass loss can be caused by (1) release of volatile components, such as adsorbed moisture, solvents, or oligomers of low molecular-weight that generally evaporate between 50–100 °C and 300 °C; (2) loss of reaction products (e.g., water or formaldehyde) from phenolic or amino resins curing (~100–250 °C); (3) chain scission is the process of creating volatile degradation products that usually need temperatures higher than 200 °C but not higher than 800 °C [175]. TGA can observe all these mass loss processes to get data on thermal stability and ageing caused by thermal and thermo-oxidation processes [175].

2.4.1.5 Microscopy and elemental analyses

Scanning electron microscopy (SEM) was used to investigate the morphology of the sample surfaces. SEM focuses a beam of high-energy electrons over the specimen surface, and signals are emitted from the interaction between the specimen and the electron beam, including low-energy secondary electrons, high-energy backscattered electron sources, and characteristic X-rays from the constituent elements. These signals are used to form three-dimensional images that provide information about the topography, morphology, chemical composition, and grain or crystallographic orientation [194].

Energy-dispersive X-ray spectroscopy (EDS) is used to characterise the elemental composition of a specimen. EDS systems are often combined with an adequately equipped SEM. The primary electron beam causes the emission of X-rays from the sample surface. The X-rays emitted correspond to the atomic states of the elements. An energy dispersion detector analyses the X-rays and the EDS spectrum, showing the peaks corresponding to the elements. This study used a 15 keV energy to SEM-EDS for elemental analysis on the substrate and coated samples [194]. SEM–EDS provides valuable information about the failure mode of a coating, which is specifically related to surface structure, microcracks, contaminants, and corrosion products. The analysis of prepared cross-sections can focus on the areas of a coating containing microcracks, blisters, and delamination, which provide information about its morphology and elemental composition.

2.4.2 Electrochemical technique

2.4.2.1 Electrochemical impedance spectroscopy

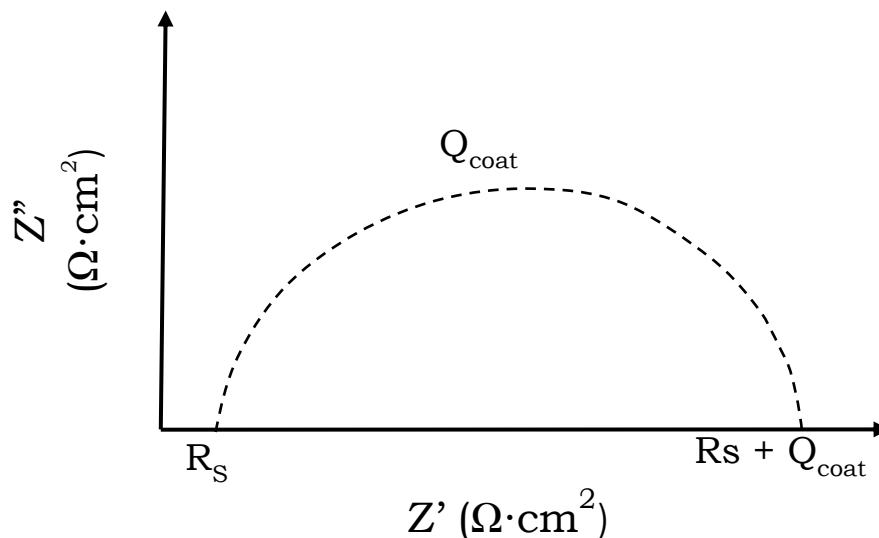
As corrosion is an electrochemical process, many electrochemical techniques have been employed over the years to study corrosion of coated metals [43]. However, owing to the high resistance of organic coatings, traditional direct-current (DC) methods cannot be used

to analyse coated metal systems [118]. Therefore, alternating current (AC) techniques, such as EIS must be used. EIS is often used to characterise corrosion protection of coated-metal systems because it is a simple and non-destructive test [102]. Experiments are conducted using a potentiostat with a standard three-electrode setup consisting of the coated sample as the working electrode (WE), a counter electrode (CE), and a reference electrode (RE). By applying a small AC sinusoidal potential to the working electrode (WE), the voltage signal (usually 10–20 mV) on the coated metallic sample can be detected [179-180]. The current of the coated sample can be measured over a range of frequencies from 100 kHz to a few mHz [97,181]. Hence, the impedance, which is the resistance to the flow of AC of an electrochemical system, can be calculated according to an extension of Ohm’s law for AC circuits:

$$Z(\omega) = V(\omega, t)/I(\omega, t) \quad (2-12)$$

Here, Z is the impedance (Ω), ω is the angular frequency (rad/s), V is the applied AC voltage (V), t is time, and I is the measured AC (A). The absolute impedance, $|Z|$, has a real component (Z') due to resistance (energy loss) and an imaginary component (Z'') due to capacitive reactance (energy storage). EIS results are typically reported in the form of a Bode plot: $|Z|$ (Ω) vs. frequency (Hz), or a Nyquist plot: $-Z''$ (Ω) vs. Z' (Ω) [181], as shown in Figure 2-20.

(a)



(b)

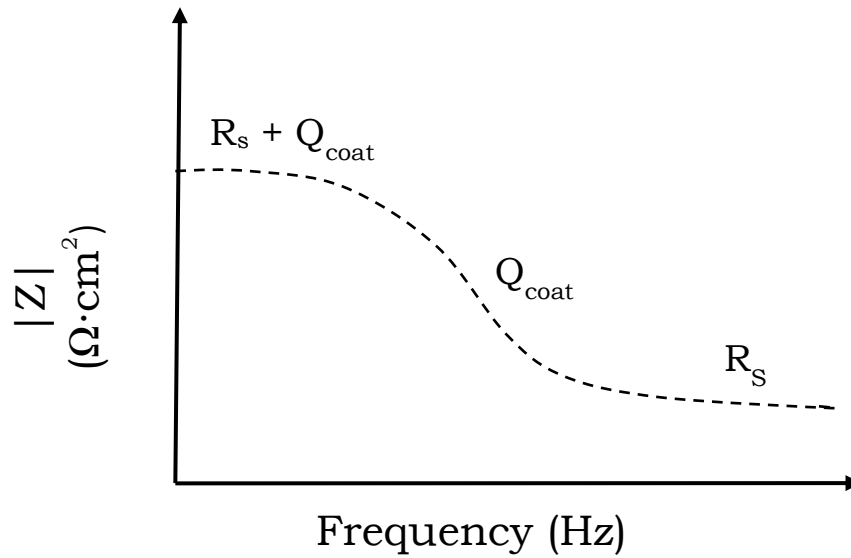


Figure 2-20: Examples of a (a) Nyquist plot and (b) Bode plot for a single time constant of the coating (Q_{coat}).

Subsequently, the EIS data are analysed using electrical equivalent circuit models. An intact coating is well described by the Randles model (Figure 2-21). EIS data are commonly modelled using the constant phase element (Q) because ideal capacitors cannot be used to model experimental data because of non-uniform coatings, surface roughness, or the inhomogeneous distribution of the current. As the coatings become more porous or local defects occur, the model becomes more complex (Figure 2-22a), and the Warburg impedance in the equivalent circuit is added to represent electrochemical and diffusion processes that deteriorate the coating, as illustrated in (Figure 2-22b) [182-183].

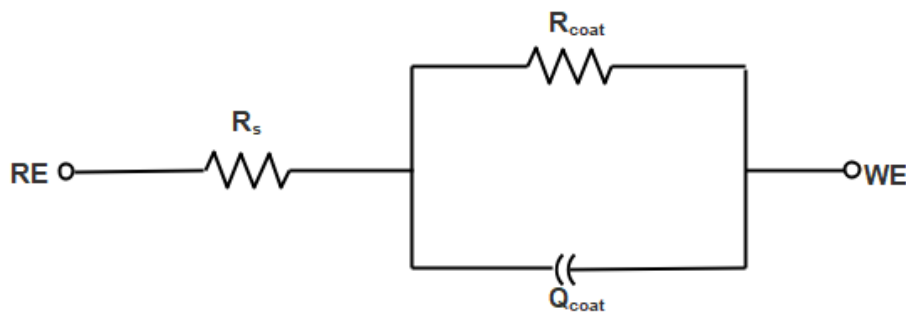
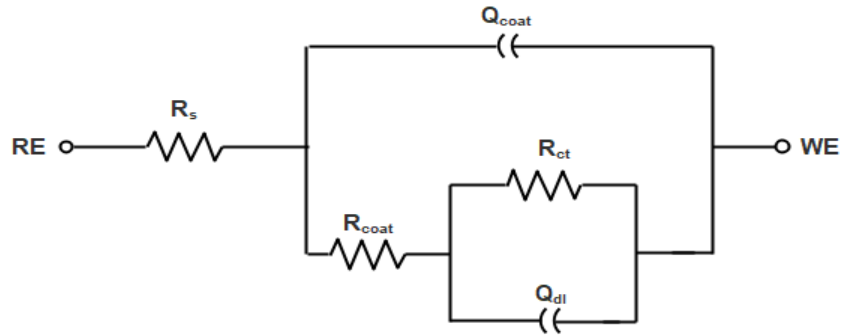


Figure 2-21: Equivalent electrical circuit used to describe an intact coating. R_s is the solution resistance, Q_{coat} is the constant phase element of the coating, and R_{coat} is the resistance of the coating.

(a)



(b)

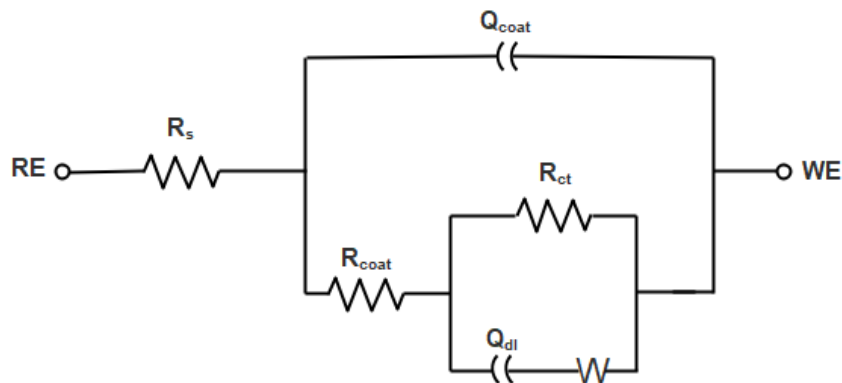


Figure 2-22: Equivalent electrical circuits used to describe defective coatings. Q_{dl} is the constant phase element of the double layer, R_{ch} is the charge-transfer resistance, and W is the Warburg impedance.

EIS is a highly effective method for evaluating the corrosion resistance of a coating applied on the metal surface, and an ISO 16773-1 standard has been issued [184]. EIS is often used to determine the water content and diffusion coefficient of the coating before and after its exposure to environmental conditions. To provide corrosion protection to steel, it has been proposed that a coating barrier should have a minimum initial impedance of $10^8 \Omega \cdot \text{cm}^2$ [182]. In addition, after the exposure of the coating to environmental conditions, the impedance should have decreased by no more than three orders of magnitude [185]. Regardless of coating thickness, blisters were observed when the impedance of the coating dropped below $10^6 \Omega \cdot \text{cm}^2$ [185]. Further in-depth EIS studies [186-187] were conducted to predict the performance of organic coatings, which provide quantitative measurements to determine the failure time and the changes in the system.

2.4.2.2 Electrochemical noise

The electrochemical noise (EN) technique measures spontaneous fluctuations in potential and current and serves as a valuable tool to gaining insights various types of corrosion, including general and localised corrosion.

Iverson [188] was among the pioneers in applying EN for corrosion research in the late 1960s. Concurrently, theoretical investigations into EN induced by electrochemical reactions were undertaken by Fleischmann, Oldfield [189], Tyagai [190] and Baker [191]. Initial efforts in corrosion research focused on examining either potential or current fluctuations in isolation under galvanostatic or potentiostatic conditions [192-195]. Eden and Hladky [196] employed a zero-resistance ammeter (ZRA) to concurrently capture and interpret both potential and current noise data.

Potentiostatic current noise measurements have been particularly informative in the study of passivity and pitting corrosion of diverse materials as well as in understanding corrosion mechanisms [197-199]. Conversely, there exists a limited body of literature on galvanostat potential noise measurements [200-201]. While both methodologies constitute valid research avenues, they may introduce disturbances that do not faithfully represent actual corrosion conditions, thus rendering them less suitable for accurate corrosion monitoring [202-203]. In contrast, ZRA-based and EN measurements permit the simultaneous recording of potential and current noise arising from the electrode's natural corrosion, i.e., at open circuit potential [203]. This methods have gained considerable attention in recent years owing to their ease of setup, non-destructive nature, non-intrusive characteristics, and notably, their capability to detect localized corrosion [204-207].

2.4.3 Physical characterisation techniques

2.4.3.1 Pull-off adhesion tests

A pull-off adhesion test measures the adhesion strength of a coating against a substrate by measuring the maximum vertical tensile force required to pull the coating away from the substrate [208]. For this, a stud or dolly is attached to the coating with an adhesive (Figure 2-23), and then pulled away from the substrate in the standard direction at a specific rate while the force is measured. Adhesive selection is a vital factor that influences adhesion testing. The cohesive strength of the adhesive should be larger than that of the coating–substrate interface [209]. The adhesive should not penetrate or interact with the coating [210]. This method has some limitations. For example, the adhesive components can penetrate the coating and reach coating–substrate interface [211]. Finally, it is important to note that these measurements are usually performed in a dry environment, which do not simulate practical operating conditions.

Therefore, the results do not give a true measure of the durability of a coated sample [212]. The presence of water at the coating–substrate interface is known to reduce adhesion [117]. A few studies have attempts to determine adhesion under wet conditions. However, this does not seem to be a valid approach because when an adhesive is applied to a surface exposed to water, it takes an extended amount of time for the adhesive to recover its properties [213].



Figure 2-23: Photograph of the dolly attached to a specimen ready for pull-off adhesion tests.

2.5 REFERENCES

- [1] P. Letardi, “Electrochemical impedance measurements in the conservation of metals,” in *Radiation in Art and Archeometry*, 2000.
- [2] J. M. Sykes, “BASIC CORROSION TECHNOLOGY FOR SCIENTISTS AND ENGINEERS,” *Surf. Eng.*, 1990.
- [3] N. Perez, *Electrochemistry and corrosion science: Second edition*. 2016.
- [4] “The corrosion of iron. By Dr. J. Newton Friend. Carnegie scholarship memories. vol. XI Pp. vi+161. Published by the iron and steel institute, 28 victoria street, London, S.W. 1. 1922. Price 16s,” *J. Soc. Chem. Ind.*, 1922.
- [5] V. V. Gerasimov and I. L. Rozenfeld, “Effect of temperature on the rate of corrosion of metals,” *Bull. Acad. Sci. USSR Div. Chem. Sci.*, 1957.
- [6] V. M. Liss, “PREVENTING CORROSION UNDER INSULATION.,” *Chem. Eng. (New York)*, 1987.
- [7] J. F. Delahunt, “Corrosion under thermal insulation and fireproofing an overview,” *NACE - Int. Corros. Conf. Ser.*, vol. 2003-April, no. 03022, pp. 1–10, 2003.
- [8] S. Winnik, *Corrosion Under Insulation (CUI) Guidelines: Revised Edition*. 2015.
- [9] Kris De Baere, “Corrosion in ballast tanks on board of merchant vessels,” p. 247, 2011.
- [10] C. P. Gardiner and R. E. Melchers, “Enclosed atmospheric corrosion in ship spaces,” *Br. Corros. J.*, 2001.
- [11] D. Thomas *et al.*, “Developments in smart organic coatings for anticorrosion applications: a review,” *Biomass Conversion and Biorefinery*. 2022.
- [12] L. Goldberg, “Take a systems approach to corrosion under insulation,” *Chem. Eng. Prog.*, 2000.
- [13] NACE International, *SP 0198-2010 Standard Recommended Practice The Control of Corrosion Under Thermal Insulation and Fireproofing Materials—A Systems Approach*, vol. 2010, no. 21084. 2010.
- [14] R. Norsworthy and P. J. Dunn, “Corrosion under thermal insulation,” *Mater. Perform.*, 2002.
- [15] NACE and 6H189, “A State-of-the-Art Report on Protective Coatings for Carbon Steel

and Austenitic Stainless Steel Surfaces Under Thermal Insulation and Cementitious Fireproofing,” in *NACE Publication*.

- [16] H. Hayashibara, E. Tada, and A. Nishikata, “Evaluation of epoxy coating for ballast tanks under thermal cycling by electrochemical impedance spectroscopy,” *ISIJ Int.*, 2016.
- [17] C. Qing, I. Oluwoye, T. Pojtanabuntoeng, H. Farhat, and M. Iannuzzi, “Evaluation of epoxy-based coating degradation under thermal insulation at elevated temperatures on different steel substrates,” *Prog. Org. Coatings*, vol. 180, no. 107544, p. 13, 2023.
- [18] H. Q. Yang, Q. Zhang, Y. M. Li, G. Liu, and Y. Huang, “Effects of Immersion Temperature on the Performance of a Marine Epoxy-Based Organic Coating for Ballast Tanks,” *J. Mater. Eng. Perform.*, 2021.
- [19] K. Haraldsen, “Paper No. 10022,” *NACE Corros. 2010*, vol. 1, no. 10022, pp. 1–11, 2010.
- [20] *Coatings Materials and Surface Coatings*. 2006.
- [21] P. Mani, A. K. Gupta, and S. Krishnamoorthy, “Comparative study of epoxy and polyester resin-based polymer concretes,” *Int. J. Adhes. Adhes.*, 1987.
- [22] J. K. Lancaster, “Abrasive wear of polymers,” *Wear*, 1969.
- [23] A. Wegmann, “Chemical resistance of waterborne epoxy/amine coatings,” *Prog. Org. Coatings*, 1997.
- [24] S. Y. Zhang, Y. F. Ding, S. J. Li, X. W. Luo, and W. F. Zhou, “Effect of polymeric structure on the corrosion protection of epoxy coatings,” *Corros. Sci.*, 2002.
- [25] S. Y. Zhang, S. J. Li, X. W. Luo, and W. F. Zhou, “Mechanism of the significant improvement in corrosion protection by lowering water sorption of the coating,” *Corros. Sci.*, 2000.
- [26] M. C. S. S. Macedo, I. C. P. Margarit-Mattos, F. L. Fragata, J. B. Jorcin, N. Pébère, and O. R. Mattos, “Contribution to a better understanding of different behaviour patterns observed with organic coatings evaluated by electrochemical impedance spectroscopy,” *Corros. Sci.*, 2009.
- [27] X. Zhang, Q. He, H. Gu, H. A. Colorado, S. Wei, and Z. Guo, “Flame-retardant electrical conductive nanopolymers based on bisphenol F epoxy resin reinforced with nano polyanilines,” *ACS Appl. Mater. Interfaces*, 2013.

- [28] M. O'Donoghue, V. Datta, and I. Fletcher, "CUI mitigation with a hot spread epoxy phenolic coating," *Corros. Manag.*, 2021.
- [29] G. Quilez-Badia *et al.*, "On board short-time high temperature heat treatment of ballast water: A field trial under operational conditions," *Mar. Pollut. Bull.*, 2008.
- [30] M. Jackson, M. Kaushik, S. Nazarenko, S. Ward, R. Maskell, and J. Wiggins, "Effect of free volume hole-size on fluid ingress of glassy epoxy networks," *Polymer (Guildf.)*, 2011.
- [31] M. T. Aronhime, X. Peng, J. K. Gillham, and R. D. Small, "Effect of time-temperature path of cure on the water absorption of high Tg epoxy resins," *J. Appl. Polym. Sci.*, 1986.
- [32] C. L. Soles, F. T. Chang, B. A. Bolan, H. A. Hristov, D. W. Gidley, and A. F. Yee, "Contributions of the nanovoid structure to the moisture absorption properties of epoxy resins," *J. Polym. Sci. Part B Polym. Phys.*, 1998.
- [33] C. L. Soles, F. T. Chang, D. W. Gidley, and A. F. Yee, "Contributions of the nanovoid structure to the kinetics of moisture transport in epoxy resins," *J. Polym. Sci. Part B Polym. Phys.*, 2000.
- [34] G. D. Shay, K. R. Olesen, and J. L. Stallings, "Predicting the water-sensitivity of film-forming coatings additives by water vapor sorption: With application to thickeners and rheology modifiers," *J. Coatings Technol.*, 1996.
- [35] B. J. Roulstone, M. C. Wilkinson, and J. Hearn, "Studies on polymer latex films: II. Effect of surfactants on the water vapour permeability of polymer latex films," *Polym. Int.*, 1992.
- [36] T. Suzuki *et al.*, "Novolac epoxy resins and positron annihilation," *J. Appl. Polym. Sci.*, 1993.
- [37] T. Suzuki *et al.*, "Free-volume characteristics and water absorption of novolac epoxy resins investigated by positron annihilation," *Polymer (Guildf.)*, 1996.
- [38] E. M. Goldstein, "The Corrosion and Oxidation of Metals: Scientific Principles and Practical Applications (Evans, Ulick R.)," *J. Chem. Educ.*, 1960.
- [39] E. E. Stansbury and R. A. Buchanan, *Fundamentals of Electrochemical Corrosion*. 2000.
- [40] R. G. Kelly, J. R. Scully, D. Shoosmith, and R. G. Buchheit, *Electrochemical Techniques in Corrosion Science and Engineering*. 2002.

- [41] R. W. Revie and H. H. Uhlig, *Corrosion and Corrosion Control: An Introduction to Corrosion Science and Engineering: Fourth Edition*. 2008.
- [42] P. E. Schweitzer, *Corrosion-Resistant Linings and Coatings*. 2001.
- [43] R. A. Dickie and F. L. Floyd, "POLYMERIC MATERIALS FOR CORROSION CONTROL: AN OVERVIEW.," in *ACS Symposium Series*, 1986.
- [44] W. S. Tait, "Principles of electrochemical corrosion important to electrochemical corrosion testing," *Test. Pr. Eng. Sci.*, pp. 1–16, 1994.
- [45] R. E. Wilson, "The Mechanism of the Corrosion of Iron and Steel in Natural Waters and the Calculation of Specific Rates of Corrosion," *Ind. Eng. Chem.*, 1923.
- [46] G. L. Cox and B. E. Roetheli, "Effect of Oxygen Concentration on Corrosion Rates of Steel and Composition of Corrosion Products Formed in Oxygenated Water," *Ind. Eng. Chem.*, 1931.
- [47] Y. Yao, L. Qiao, and A. Volinsky, "Hydrogen effects on stainless steel passive film fracture studied by nanoindentation," *Corros. sci.*, vol. 53, no. 9, pp. 2679–2683, 2011.
- [48] T. P. Hoar, "The breakdown and repair of oxide films on iron," *Trans. Faraday Soc.*, 1949.
- [49] C. W. Borgmann, "Initial Corrosion Rate of Mild Steel Influence of The Cation," *Ind. Eng. Chem.*, 1937.
- [50] K. De Baere, H. Verstraelen, P. Rigo, S. Van Passel, S. Lenaerts, and G. Potters, "Study on alternative approaches to corrosion protection of ballast tanks using an economic model," *Mar. Struct.*, 2013.
- [51] T. Shinohara, Y. Hosoya, W. Oshikawa, and S. I. Motoda, "Effect of thickness of water film on atmospheric corrosion behavior of carbon steel," in *Proceedings - Electrochemical Society*, 2005.
- [52] E. mesogios Ltd, "Ballast tank corrosion," <https://eneconmesogios.com/project/ballast-tank-pipe-work-protection/>. .
- [53] "corrosion under insulation," <https://russeltech.com/>. .
- [54] M. Wu, Z. Gao, S. Wu, Y. Liu, and W. Hu, "Effect of temperature on corrosion behavior of X70 pipeline steel in 3.5% NaCl solution," *Int. J. Electrochem. Sci.*, 2021.
- [55] J. Li, "Study on corrosion protection of organic coatings using electrochemical techniques: Thermal property characterization, film thickness investigation, and

- coating performance evaluation,” no. June, 2002.
- [56] “API RP 583; Corrosion Under Insulation and Fireproofing,” *Am. Petroleum Inst.*, 2021.
- [57] PR0198, “Control of Corrosion under Thermal Insulation and Fire Proofing Materials—A Systems Approach,” 2017.
- [58] M. F. Hamad, H. D. Abdul Kader, H. A. Alabdly, B. O. Hasan, and I. S. M. Ali, “Corrosion of Carbon Steel in Oxygen and NaCl Concentration Cells: the Influence of Solution Temperature and Aeration,” *Iraqi J. Chem. Pet. Eng.*, 2019.
- [59] G. De Landtsheer, *Corrosion Under insulation (CUI) Guidelines: Technical Guide for Managing CUI*. San Diego: Elsevier Science & Technology, 2020.
- [60] Q. Cao *et al.*, “A Review of Corrosion under Insulation: A Critical Issue in the Oil and Gas Industry,” *Metals*. 2022.
- [61] W. Geary and R. Parrott, “Two corrosion under insulation failure case studies,” *Loss Prev. Bull.*, 2016.
- [62] Y. Liu, Z. Gao, X. Lu, and L. Wang, “Effect of temperature on corrosion and cathodic protection of X65 pipeline steel in 3.5% NaCl solution,” *Int. J. Electrochem. Sci.*, 2019.
- [63] I. H. Rhee, H. Jung, and D. Cho, “Evaluation of pH control agents influencing on corrosion of carbon steel in secondary water chemistry condition of pressurized water reactor,” *Nucl. Eng. Technol.*, 2014.
- [64] “Standard Test Methods for Chemical Analysis of Thermal Insulation Materials for Leachable Chloride , Fluoride , Silicate , and Sodium Ions,” *ASTM C871*, 1995.
- [65] S. Olenin, S. Gollasch, S. Jonušas, and I. Rimkutė, “En-route investigations of plankton in ballast water on a ship’s voyage from the Baltic Sea to the open Atlantic coast of Europe,” in *International Review of Hydrobiology*, 2000.
- [66] M. Dickman and F. Zhang, “Mid-ocean exchange of container vessel ballast water. 2: Effects of vessel type in the transport of diatoms and dinoflagellates from Manzanillo, Mexico, to Hong Kong, China,” *Mar. Ecol. Prog. Ser.*, 1999.
- [67] L. Alwis, T. Sun, and K. T. V. Grattan, “Optical fibre-based sensor technology for humidity and moisture measurement: Review of recent progress,” *Measurement: Journal of the International Measurement Confederation*. 2013.
- [68] P. Sharma, “Predictive corrosion under insulation monitoring using electro-magnetic guided radar,” *Corros. Manag.*, 2020.

- [69] P. J. Thomas and J. O. Hellevang, "A distributed fibre optic approach for providing early warning of Corrosion Under Insulation (CUI)," *J. Loss Prev. Process Ind.*, 2020.
- [70] R. Javaherdashti, "Corrosion under Insulation (CUI): A review of essential knowledge and practice," *J. Mater. Sci. Surf. Eng.*, vol. 1, no. 2, pp. 36–43, 2014.
- [71] S. Shrestha and A. Sturgeon, "Characteristics and electrochemical corrosion behaviour of thermal sprayed aluminium (TSA) coatings prepared by various wire thermal spray processes Electrochemical polarisation," *Annu. Congr. Eur. Fed. Corros.*, 2005.
- [72] S. Paul, "Cathodic protection of offshore structures by extreme damage tolerant sacrificial coatings," in *NACE - International Corrosion Conference Series*, 2018.
- [73] J. Reynolds and P. Bock, "Third generation polysiloxane coatings for CUI mitigation," in *NACE - International Corrosion Conference Series*, 2018.
- [74] P. P. Bock, "Service life, reliability and reparability of systems for preventing corrosion under insulation," in *NACE - International Corrosion Conference Series*, 2012.
- [75] M. Halliday, "Developments & testing of new generation high temperature corrosion resistant coatings," in *NACE - International Corrosion Conference Series*, 2005.
- [76] B. T. A. Chang and A. N. Moosavi, "Critical pre-qualification test protocol for external high temperature pipeline coatings," in *NACE - International Corrosion Conference Series*, 2014.
- [77] N. Wilds, "Corrosion under insulation," in *Trends in Oil and Gas Corrosion Research and Technologies: Production and Transmission*, Elsevier Inc., 2017, pp. 409–429.
- [78] L. T. Pedersen, "Corrosion under insulation technologies - High performance solutions," in *Society of Petroleum Engineers - Abu Dhabi International Petroleum Exhibition and Conference, ADIPEC 2015*, 2015.
- [79] A. V. Radhamani, H. C. Lau, and S. Ramakrishna, "Nanocomposite coatings on steel for enhancing the corrosion resistance: A review," *Journal of Composite Materials*. 2020.
- [80] Y. Yang, A. B. Bodington, and B. T. A. Chang, "Evaluation of protective coatings to mitigate corrosion under insulation," *NACE - Int. Corros. Conf. Ser.*, vol. 6, no. 7804, pp. 4412–4426, 2016.
- [81] Y. Korobov and Douglass P. Moore, "performance testing methods for offshore coatings: cyclic, EIS and stress," *Corrosion*, no. 04005, pp. 1–15, 2004.

- [82] The Maritime Safety Committee (IMO), “Resolution MSC.215(82)Performance standard for protective coatings of dedicated seawater ballast tanks on all new ships and of double-side skin spaces of bulk carriers,” 2006.
- [83] ASTM D5894, “Standard Practice for Cyclic Salt Fog / UV Exposure of Painted Metal , (Alternating Exposures in a Fog / Dry Cabinet and a UV / Condensation Cabinet) 1,” *ASTM Stand.*, 2005.
- [84] ISO 12944-6, “Paints and varnishes - Corrosion protection of steel structures by protective paint systems - Part 6: Laboratory performance test methods,” *NSAI Stand.*, 2018.
- [85] NACE TM-0184, “Accelerated Test Procedures for Screening Atmospheric Surface Coating Systems for Offshore Platforms and Equipment,” *NACE*, 1994.
- [86] P. Dillmann, F. Mazaudier, and S. Hoërlé, “Advances in understanding atmospheric corrosion of iron. I. Rust characterisation of ancient ferrous artefacts exposed to indoor atmospheric corrosion,” *Corros. Sci.*, 2004.
- [87] R. B. Seymour, “Plastics vs. corrosives,” *John Wiley Sons, Inc*, 1982.
- [88] I. Suzuki, *Corrosion-resistant coatings technology*. 1989.
- [89] Z. W. Wicks, F. N. Jones, S. P. Pappas, and D. A. Wicks, *Organic coatings: science and technology, Third edition*. 2007.
- [90] Z. W. Wicks, F. N. Jones, S. P. Pappas, and D. A. Wicks, *Organic Coatings: Science and Technology*. 2006.
- [91] J. J. Licari, *Coating Materials for Electronic Applications: Polymers, Processing, Reliability, Testing*. 2003.
- [92] C. G. Munger, “Corrosion prevention by protective coatings.,” 1984.
- [93] M. Ogata, N. Kinjo, and T. Kawata, “effects of crosslinking on physical properties of phenol-formaldehyde novolac cured epoxy resins,” *J. appl. Polym. Sci.*, 1993.
- [94] V. B. Gupta and C. Brahatheeswaran, “Molecular packing and free volume in crosslinked epoxy networks,” *Polymer (Guildf)*., 1991.
- [95] D. Chinn, S. B. Shim, and J. C. Seferis, “Thermal and mechanical characterization of high performance epoxy systems with extended cure times,” *J. Therm. Anal.*, 1996.
- [96] N. S. Sangaj and V. C. Malshe, “Permeability of polymers in protective organic coatings,” *Progress in Organic Coatings*. 2004.

- [97] E. McCafferty, *Introduction to corrosion science*. 2010.
- [98] G. de Wit, J. H. W.; der Weijde, D. H.; Ferrari, "In Corrosion Mechanisms in Theory and Practice: Second Edition, Revised and Expanded," *Org. Coatings*, 2002.
- [99] S. Shreepathi, S. M. Naik, and M. R. Vattipalli, "Water transportation through organic coatings: Correlation between electrochemical impedance measurements, gravimetry, and water vapor permeability," *J. Coatings Technol. Res.*, 2012.
- [100] S. Lindqvist, "Theory of dielectric properties of heterogeneous substances applied to water in a paint film," *Corrosion*, 1985.
- [101] F. Deflorian, L. Fedrizzi, and P. L. Bonora, "Influence of the photo-oxidative degradation on the water barrier and corrosion protection properties of polyester paints," *Corros. Sci.*, 1996.
- [102] D. M. Brasher and A. H. Kingsbury, "Electrical measurements in the study of immersed paint coatings on metal. I. Comparison between capacitance and gravimetric methods of estimating water-uptake," *J. Appl. Chem.*, 2007.
- [103] F. Deflorian, L. Fedrizzi, S. Rossi, and P. L. Bonora, "Organic coating capacitance measurement by EIS: Ideal and actual trends," *Electrochim. Acta*, 1999.
- [104] D. M. Wormwell, F.; Brasher, "Electrochemical studies of protective coatings on metals. II. Resistance and capacitance measurements on painted steel immersed in sea water.," *Iron Steel Inst.*, 1950.
- [105] G. Z. Xiao and M. E. R. Shanahan, "Swelling of DGEBA/DDA epoxy resin during hydrothermal ageing," *Polymer (Guildf)*., 1998.
- [106] A. F. Abdelkader and J. R. White, "Curing characteristics and internal stresses in epoxy coatings: Effect of crosslinking agent," *J. Mater. Sci.*, 2005.
- [107] G. Z. Xiao and M. E. R. Shanahan, "Water absorption and desorption in an epoxy resin with degradation," *J. Polym. Sci. Part B Polym. Phys.*, 1997.
- [108] P. Moy and F. E. Karasz, "Epoxy-water interactions," *Polym. Eng. Sci.*, 1980.
- [109] J. Li, C. J. S, G. P. Bierwagen, D. J. Mills, and D. E. Tallman, "Thermal transition effects and electrochemical properties in organic coatings: part 1 - initial studies on corrosion protective organic coatings," *Corros. Sci.*, 1998.
- [110] A. Miszczyk and T. Schauer, "Electrochemical approach to evaluate the interlayer adhesion of organic coatings," in *Progress in Organic Coatings*, 2005.

- [111] K. N. Allahar, B. R. Hinderliter, D. E. Tallman, and G. P. Bierwagen, "Water Transport in Multilayer Organic Coatings," *J. Electrochem. Soc.*, 2008.
- [112] H. Leidheiser and R. D. Granata, "Ion Transport through Protective Polymeric Coatings Exposed to an Aqueous Phase," *IBM J. Res. Dev.*, 1988.
- [113] N. L. Thomas, "The barrier properties of paint coatings," *Prog. Org. Coatings*, 1991.
- [114] J. Comyn, "Introduction to Polymer Permeability and the Mathematics of Diffusion," in *Polymer Permeability*, 1985.
- [115] M. Svoboda and J. Mleziva, "Penetration of inorganic compounds and ions into coatings," *Prog. Org. Coatings*, 1974.
- [116] B. W. Cherry, *Metallic Corrosion*. London, 1966.
- [117] W. Funke, "Problems and progress in organic coatings science and technology," *Progress in Organic Coatings*. 1997.
- [118] G. Grundmeier, W. Schmidt, and M. Stratmann, "Corrosion protection by organic coatings: Electrochemical mechanism and novel methods of investigation," *Electrochim. Acta*, 2000.
- [119] W. Funke, "The role of Adhesion in Corrosion Protection by Organic Coatings," *J. Oil Colour Chem. Assoc.*, 1985.
- [120] A. J. Kinloch, *The science of adhesion*. 1980.
- [121] H. Leidheiser, "CORROSION OF PAINTED METALS - A REVIEW.," *Corrosion*, 1982.
- [122] V. Palanivel, D. Zhu, and W. J. Van Ooij, "Nanoparticle-filled silane films as chromate replacements for aluminum alloys," in *Progress in Organic Coatings*, 2003.
- [123] W. Funke, "Blistering of paint films and filiform corrosion," *Progress in Organic Coatings*. 1981.
- [124] L. L. Slabaugh, W. H.; DeJager, W.; Hoover, S. E.; Hutchinson, *Filiform corrosion of aluminum*. J. Paint Technol., 1972.
- [125] H. Leidheiser, "Water disbondment and wet adhesion of organic coatings on metals: a review and interpretation," *J. Oil Colour Chem. Assoc.*, p. 70, 1987.
- [126] W. Funke and H. Haagen, "Empirical or Scientific Approach to Evaluate the Corrosion Protective Performance of Organic Coatings," *Ind. Eng. Chem. Prod. Res. Dev.*, 1978.

- [127] B. C. Rincon Troconis, “Blister Test Measurements of Adhesion and Adhesion Degradation of Organic Polymers on AA2024-T3.,” The Ohio State University, 2013.
- [128] T. R. Bullett, “Adhesion of paint films,” *J. Oil Colour Chem. Assoc.*, pp. 46, 441, 1963.
- [129] O. Negele and W. Funke, “Internal stress and wet adhesion of organic coatings,” *Prog. Org. Coatings*, 1996.
- [130] S. Effendy, T. Zhou, H. Eichman, M. Petr, and M. Z. Bazant, “Blistering failure of elastic coatings with applications to corrosion resistance,” *Soft Matter*, 2021.
- [131] K. Pélissier and D. Thierry, “Powder and high-solid coatings as anticorrosive solutions for marine and offshore applications? A review,” *Coatings*. 2020.
- [132] P. M. van der Meer-Lerk, L. A.; Heertjes, “Blistering of varnish films on substrates induced by salts,” *J. Oil Colour Chem. Assoc.*, pp. 79–84, 975.
- [133] B. Fitzsimons and T. Parry, “Coating Failures and Defects,” in *Protective Organic Coatings*, 2018.
- [134] C. F. Sharman, “Filiform underfilm corrosion of lacquered steel surfaces [5],” *Nature*. 1944.
- [135] R. T. Ruggeri and T. R. Beck, “ANALYSIS OF MASS TRANSFER IN FILIFORM CORROSION.,” *Corrosion*, 1983.
- [136] H. Kaesche, “Untersuchungen über die Filigrankorrosion lackierter Stahlbleche,” *Mater. Corros.*, 1959.
- [137] J. Azevedo, “A new approach for ballast & cargo tank coating: A solvent-free and humidity tolerant epoxy system with edge-retentive properties,” in *RINA, Royal Institution of Naval Architects International Conference - Advanced Marine Materials and Coatings - Papers*, 2006.
- [138] R. Towers and J. Eliasson, “The future of ballast tank coatings,” *Nav. Archit.*, 2008.
- [139] M. J. Mitchell, D. Claydon, and D. Ward, “A critical review of current performance tests for offshore anti-corrosive Coatings,” in *NACE - International Corrosion Conference Series*, 2005.
- [140] J. W. Ringsberg, “A study on the influence of ageing of coatings on their mechanical properties and fracture in ballast tanks,” *Ships Offshore Struct.*, 2017.
- [141] Living Oceans, “Tanker Technology: Limitation of Double Hulls,” *Society*, 2011.

- [142] G. Mills and J. Eliasson, "Factors influencing early crack in marine cargo and ballast tank development," *Journal of Protective Coatings and Linings*. 2006.
- [143] D. G. Lee and B. C. Kim, "Investigation of coating failure on the surface of a water ballast tank of an oil tanker," *J. Adhes. Sci. Technol.*, 2005.
- [144] B. J. Zhang, C. S. Lim, B. C. Kim, and D. G. Lee, "Stress analysis and evaluation of cracks developed on the coatings for welded joints of water ballast tanks," in *NACE - International Corrosion Conference Series*, 2005.
- [145] J. Ringsberg, "On Mechanical interaction between Steel and Coating in Welded Structures," *Chalmers Univ. Technol.*, 1997.
- [146] V. Mazel and P. Richardin, "ToF-SIMS Study of Organic Materials in Cultural Heritage: Identification and Chemical Imaging," in *Organic Mass Spectrometry in Art and Archaeology*, 2009.
- [147] A. M. Belu, D. J. Graham, and D. G. Castner, "Time-of-flight secondary ion mass spectrometry: Techniques and applications for the characterization of biomaterial surfaces," *Biomaterials*. 2003.
- [148] A. Brunelle, D. Touboul, and O. Laprévotte, "Biological tissue imaging with time-of-flight secondary ion mass spectrometry and cluster ion sources," *Journal of Mass Spectrometry*. 2005.
- [149] G. Montaudo, *Mass Spectroscopy of polymers*. Florida, 2001.
- [150] Y. T. R. Lau, L. T. Weng, K. M. Nga, and C. M. Chan, "Surface chemical composition and conformation of liquid crystalline polymers studied with ToF-SIMS and XPS," *Surf. Interface Anal.*, 2010.
- [151] J. A. Treverton, A. J. Paul, and J. C. Vickerman, "Characterization of adhesive and coating constituents by time-of-flight secondary ion mass spectrometry (ToF-SIMS). Part 1: Epoxy-terminated diglycidyl polyethers of bisphenol-A and propal-2-ol," *Surf. Interface Anal.*, 1993.
- [152] F. Awaja, G. Van Riessen, G. Kelly, B. Fox, and P. J. Pigram, "ToF-sims investigation of epoxy resin curing reaction at different resin to hardener ratios," *J. Appl. Polym. Sci.*, 2008.
- [153] R. Bhargava, S. Q. Wang, and J. L. Koenig, "FTIR microspectroscopy of polymeric systems," *Advances in Polymer Science*. 2003.
- [154] S. J. Oh, D. C. Cook, and H. E. Townsend, "Characterization of iron oxides commonly

- formed as corrosion products on steel,” *Hyperfine Interact.*, 1998.
- [155] D. F. D.L.A., V. S. S., and D. O. M.T., “Raman microspectroscopy of some iron oxides and oxyhydroxides,” *J. Raman Spectrosc.*, 1997.
- [156] D. C. Cook, “Spectroscopic identification of protective and non-protective corrosion coatings on steel structures in marine environments,” in *Corrosion Science*, 2005.
- [157] D. Neff, L. Bellot-Gurlet, P. Dillmann, S. Reguer, and L. Legrand, “Raman imaging of ancient rust scales on archaeological iron artefacts for long-term atmospheric corrosion mechanisms study,” in *Journal of Raman Spectroscopy*, 2006.
- [158] H. Antonya, L. Maréchalb, L. Legrand, A. Chausséa, S. Perrinb, and P. Dillmann, “Electrochemical study of lepidocrocite reduction and redox cycling for the mechanistic modelling of atmospheric corrosion,” in *EUROCORR 2004 - European Corrosion Conference: Long Term Prediction and Modelling of Corrosion*, 2004.
- [159] M. Yamashita, H. Miyuki, Y. Matsuda, H. Nagano, and T. Misawa, “The long term growth of the protective rust layer formed on weathering steel by atmospheric corrosion during a quarter of a century,” *Corros. Sci.*, 1994.
- [160] L. Bellot-Gurlet, D. Neff, S. Réguer, J. Monnier, M. Saheb, and P. Dillmann, “Raman studies of corrosion layers formed on archaeological irons in various media,” 2009, pp. 8, 147–156.
- [161] S. Savoye *et al.*, “Experimental investigations on iron corrosion products formed in bicarbonate/carbonate-containing solutions at 90°C,” *Corros. Sci.*, 2001.
- [162] X. Zhang, K. Xiao, C. Dong, J. Wu, X. Li, and Y. Huang, “In situ Raman spectroscopy study of corrosion products on the surface of carbon steel in solution containing Cl- and SO₄²⁻,” *Eng. Fail. Anal.*, no. 18, 1981–1989, 2011.
- [163] S. Réguer, D. Neff, L. Bellot-Gurlet, and P. Dillmann, “Deterioration of iron archaeological artefacts: Micro-Raman investigation on Cl-containing corrosion products,” *J. Raman Spectrosc.*, 2007.
- [164] M. Claybourn and P. H. Turner, “Fourier Transform Infrared and Raman Studies of Coatings,” 1993.
- [165] G. Ramaiah, Ramesh.K.P, and D. Bhatia, “Structural analysis of merino wool, pashmina and angora fibers using analytical instruments like scanning electron microscope and infra-red spectroscopy,” *Int. J. Eng. Technol. Sci. Res.* 2394-3386, 2017.

- [166] J. R. Webb, "REACTION PROFILES FOR KINETIC STUDIES OF INHOMOGENEOUS REACTIONS WITHIN SOLID ORGANIC FILMS.," *J Polym Sci Part A-1 Polym Chem.* 1972.
- [167] C. A. S. Hill, "Degradation studies of plasticized PVC. I. Multiple internal reflection infrared spectroscopy," *J. Appl. Polym. Sci.*, 1982.
- [168] M. S. Oliver, K. Y. Blohowiak, and R. H. Dauskardt, "Molecular structure and fracture properties of ZrOX/Epoxy silane hybrid films," *J. Sol-Gel Sci. Technol.*, 2010.
- [169] G. S. Bales, R. Bruinsma, E. A. Eklund, R. P. U. Karunasiri, J. Rudnick, and A. Zangwill, "Growth and erosion of thin solid films," *Science (80-.)*, 1990.
- [170] D. Brezinski, "an infrared spectroscopy atlas for the coating-4th Ed.," *Fed. Soc. coatings Technol.*, vol. 1 & 2, 1991.
- [171] A. J. Vreugdenhil, V. N. Balbyshev, and M. S. Donley, "Nanostructured silicon sol-gel surface treatments for Al 2024-T3 protection," *J. Coatings Technol.*, 2001.
- [172] K. Barton, M. Cullen, and B. Duffy, "Sol-Gel Chemistry Engineering for Corrosion Protection," 2017.
- [173] K. B. Gireesh, K. K. Jena, S. Allauddin, K. R. Radhika, R. Narayan, and K. V. S. N. Raju, "Structure and thermo-mechanical properties study of polyurethane-urea/glycidoxypropyltrimethoxysilane hybrid coatings," *Prog. Org. Coatings*, 2010.
- [174] D. Álvarez, A. Collazo, M. Hernández, X. R. Nóvoa, and C. Pérez, "Characterization of hybrid sol-gel coatings doped with hydrotalcite-like compounds to improve corrosion resistance of AA2024-T3 alloys," *Prog. Org. Coatings*, 2010.
- [175] J. D. Menczel and R. B. Prime, *Thermal Analysis of Polymers: Fundamentals and Applications.* 2008.
- [176] B. Wunderlich, *Thermal analysis of polymeric materials.* 2005.
- [177] *Compositional Analysis by Thermogravimetry.* 1988.
- [178] Bair, *in thermal characterization of polymeric materials*, 2nd ed. San Diego, 1997.
- [179] F. Mansfeld, "Use of electrochemical impedance spectroscopy for the study of corrosion protection by polymer coatings," *Journal of Applied Electrochemistry.* 1995.
- [180] J. N. Murray, "Electrochemical test methods for evaluating organic coatings on metals: An update. Part III: Multiple test parameter measurements," *Prog. Org. Coatings*, 1997.

- [181] S. Cottis, R.; Turgoose, "Electrochemical Impedance and Noise," *NACE Int.*, 1999.
- [182] V. Lavaert, M. De Cock, M. Moors, and E. Wettinck, "Influence of pores on the quality of a silicon polyester coated galvanized steel system," *Prog. Org. Coatings*, 2000.
- [183] M. Özcan, I. Dehri, and M. Erbil, "EIS study of the effect of high levels of SO₂ on the corrosion of polyester-coated galvanised steel at different relative humidities," *Prog. Org. Coatings*, 2002.
- [184] ISO and 16773-1, "Electrochemical impedance spectroscopy (EIS) on coated and uncoated metallic specimens," *ISO Int.*, 2016.
- [185] I. Sekine, "Recent evaluation of corrosion protective paint films by electrochemical methods," *Prog. Org. Coatings*, 1997.
- [186] M. Kendig and J. Scully, "Basic aspects of electrochemical impedance application for the life prediction of organic coatings on metals," *Corrosion*, 1990.
- [187] G. W. Walter, "The application of impedance methods to study the effects of water uptake and chloride ion concentration on the degradation of paint films-I. Attached films," *Corros. Sci.*, 1991.
- [188] W. P. Iverson, "Transient Voltage Changes Produced in Corroding Metals and Alloys," *J. Electrochem. Soc.*, 1968.
- [189] M. Fleischmann and J. W. Oldfield, "Generation-recombination noise in weak electrolytes," *J. Electroanal. Chem.*, 1970.
- [190] V. A. Tyagai, "Faradaic noise of complex electrochemical reactions," *Electrochim. Acta*, 1971.
- [191] G. C. Barker, "Faradaic reaction noise," *J. Electroanal. Chem.*, 1977.
- [192] K. Hladky and J. L. Dawson, "The measurement of localized corrosion using electrochemical noise," *Corros. Sci.*, 1981.
- [193] J. L. Dawson, K. Hladky, and D. A. Eden, "ELECTROCHEMICAL NOISE - SOME NEW DEVELOPMENTS IN CORROSION MONITORING.," 1983.
- [194] J. L. Dawson and M. G. S. Ferreira, "Electrochemical studies of the pitting of austenitic stainless steel," *Corros. Sci.*, 1986.
- [195] H. T. C Gabrielli, F Huet, M Keddou, "Application of electrochemical noise measurements to the study of localized and uniform corrosion," *Eur. Congr. Corros.*, vol. 8th, 1985.

- [196] D. Eden and K. Hladky, “electrochemical noise - simultaneous monitoring of potential and current noise signals from corroding electrodes,” 1987.
- [197] Y. Miyata, T. Handa, and H. Takazawa, “An analysis of current fluctuations during passive film breakdown and repassivation in stainless alloys,” *Corros. Sci.*, 1990.
- [198] W. J. Tobler and S. Virtanen, “Effect of Mo species on metastable pitting of Fe18Cr alloys-A current transient analysis,” *Corros. Sci.*, 2006.
- [199] A. R. Trueman, “Determining the probability of stable pit initiation on aluminium alloys using potentiostatic electrochemical measurements,” *Corros. Sci.*, 2005.
- [200] F. Safizadeh and E. Ghali, “Monitoring passivation of Cu-Sb and Cu-Pb anodes during electrorefining employing electrochemical noise analyses,” *Electrochim. Acta*, 2010.
- [201] C. Gabrielli and M. Keddam, “Review of applications of impedance and noise analysis to uniform and localized corrosion,” *Corrosion*, 1992.
- [202] R. A. Cottis, “4- Electrochemical noise for corrosion monitoring A2,” *Woodhead*, pp. 86–110, 2008.
- [203] J. L. Dawson, “Electrochemical noise measurement: The definitive in-situ technique for corrosion applications?,” *ASTM Spec. Tech. Publ.*, 1996.
- [204] F. Hass, A. C. T. G. Abrantes, A. N. Diógenes, and H. A. Ponte, “Evaluation of naphthenic acidity number and temperature on the corrosion behavior of stainless steels by using Electrochemical Noise technique,” *Electrochim. Acta*, 2014.
- [205] A. Chen *et al.*, “Study of pitting corrosion on mild steel during wet-dry cycles by electrochemical noise analysis based on chaos theory,” *Corros. Sci.*, 2013.
- [206] R. A. Cottis, M. A. Al-Ansari, G. Bagley, and A. Pettiti, “Electrochemical noise measurements for corrosion studies,” *Mater. Sci. Forum*, 1998.
- [207] E. C. Rios *et al.*, “Corrosion of AISI 1020 steel in crude oil studied by the electrochemical noise measurements,” *Fuel*, 2015.
- [208] ASTM, “D4541-09: Standard Test Method for Pull-Off Strength of Coatings Using Portable Adhesion,” *ASTM Int.*, 2014.
- [209] R. Francis, “Comprehending coating adhesion: Part 2: Pull-off adhesion testing,” in *Corrosion and Prevention 2017*, 2017.
- [210] S. Kambhampati and T. Pojtanabuntoeng, “a systemic study on the effects of key influencing factors on pull-off adhesion test of organic coatings,” *Corros. Sci.*

engineering, vol. 1, p. 11, 2023.

- [211] P. R. Chalker, S. J. Bull, and D. S. Rickerby, "A review of the methods for the evaluation of coating-substrate adhesion," *Mater. Sci. Eng. A*, 1991.
- [212] M. Niknahad, S. Moradian, and S. M. Mirabedini, "The adhesion properties and corrosion performance of differently pretreated epoxy coatings on an aluminium alloy," *Corros. Sci.*, 2010.
- [213] B. C. Rincon Troconis and G. S. Frankel, "Effect of Roughness and Surface Topography on Adhesion of PVB to AA2024-T3 using the Blister Test," *Surf. Coatings Technol.*, 2013.
- [214] J. S. M. Carter, "Capter 5- Microscopy," in *Res. Tech. Neurosci.*, 2015.

CHAPTER 3

S. Ahmed, Y. Hou, K. Lepkova, T. Pojtanabuntoeng, Investigation of the effect chloride ions on carbon steel in closed environments , Journal of corrosion and materials degradation, 4, 364-381 (2023) .

This chapter presents the published paper with modified formats and contents that match the overall style of the thesis.

Effect of Chloride Ions and Temperature on the Corrosion of Carbon Steel in Closed Environments

Abstract

This case study investigated carbon steel corrosion in an enclosed environment, where one set of steel specimens was immersed in 3.5 wt. % NaCl solution and another was exposed to humid (condensation) conditions. Electrochemical noise and electrochemical impedance spectroscopy techniques were used to monitor real-time corrosion behaviour. The samples were evaluated with surface characterisation techniques including optical light microscopy, SEM–EDS, and Raman spectroscopy. The results showed that carbon steel immersed in the liquid phase at a constant temperature exhibited the highest weight loss. However, the carbon steel exposed to water condensation (gas phase) at 80 °C exhibited extensive localised corrosion.

Keywords: Carbon steel; SEM; EIS; EN; Localised corrosion and weight loss

3.1. Introduction

Carbon steel is a widely used engineering material owing to its cost-effectiveness and high strength, accounting for approximately 85% of the annual steel production worldwide [1]. Despite its limited corrosion resistance, carbon steel is used in marine applications, desalination plants, pipelines, and ballast tanks in ships [2]. Carbon steel is electrically conducting, so its corrosion process is influenced by the properties of the solution in which it is immersed or exposed to, such as the salt concentration [3], humidity [4], dissolved oxygen content [5], and temperature [6]. In areas such as ballast tanks or insulated metal structures, carbon steel can be exposed to two distinct environments, i.e., immersion and condensation. Thus, different corrosion behaviours are observed in these two scenarios. Previous studies showed that the temperature, relative humidity, and chloride ion concentration affect the corrosion rate of materials, and complex interactions exist among these factors [7-10]. It was reported that the immersion time and chloride concentration are the critical factors determining the severity of corrosion [4]. However, another study argued that the temperature and relative humidity were more important [11]. Because of these conflicting conclusions, further investigation is required.

Sodium chloride (NaCl) solution is a typical electroconductive media that can destroy the dense iron oxide layer formed on steel via reactions with chloride ions (Cl^-) [12]. The nanometre-thick oxide passivation film on the steel resists overall corrosion, but it is susceptible to severe localised attack in certain aggressive media [13]. The most well-known inducer of localised passive film breakdown is chloride ions. Despite the enormous amount of experimental data and diverse hypotheses and models proposed to date [3,14-16], the influence of chloride ions on the corrosion product is still not sufficiently understood and the relationship between the chloride ions and temperature remains one of the most important and basic problems in corrosion science.

The present work aimed to distinguish the two potential environments produced by the constant exposure to water evaporation and condensation in an enclosed space, simulated using a 3.5 wt.% NaCl solution. Several methods were used to characterise corrosion products, including SEM-EDS and Raman spectroscopy. Electrochemical techniques such as electrochemical noise (EN) and electrochemical impedance spectroscopy (EIS) were used to derive insight into localised corrosion activity and obtain real-time corrosion rates. Uniform corrosion rates were determined using a weight-loss technique and the severity of localised corrosion was quantified using a 3D surface profilometer.

3.2. Experimental

3.2.1 Materials and corrosion solutions

Carbon steel (AS 3678/ Grade 250) similar to grade ASTM A 36 [17] was used, with a nominal composition of 0.22 C, 0.55 Si, 1.7 Mn, 0.04 P, 0.03 S (wt.%), and balance of Fe. The specimens were cut to dimensions of 20 mm × 20 mm × 2.5 mm. All specimens were coated with a cationic epoxy using an electrodeposition system (PowerCron 6000 CX). The electrocoated parts were placed in an oven to cure at 170 °C for 20 min. Then, the surface of each sample was wet ground with up to 600-grit SiC paper and rinsed with deionised water and ethanol. The surface was then dried with nitrogen gas and stored in a desiccator until required. The exposed surface area of the specimens was 4 cm². Before testing, the samples were weighed with an analytical balance (0.1 mg precision). In each weight-loss experiment, three samples were prepared for analysis. The electrochemical probe was made with three identical carbon steel coupons (AS 3678/Grade250) with dimensions of 19 mm × 4 mm × 2.5 mm. Each coupon was soldered to an electrical wire. The three metal coupons were placed in parallel and mounted 1 mm apart using epoxy resin as shown in Figure 3-1. The exposed surface area of each coupon was 19 mm × 4 mm, which was wet ground up to 600 grit with SiC paper and rinsed with deionised water and ethanol. The test solution was 3.5 wt.% NaCl, prepared from deionised water and reagent grade NaCl (99.7%). The pH of the solution was 5.5 at 22 °C, as determined by a pH sensor (Hanna Instruments), which was used without further adjustment.

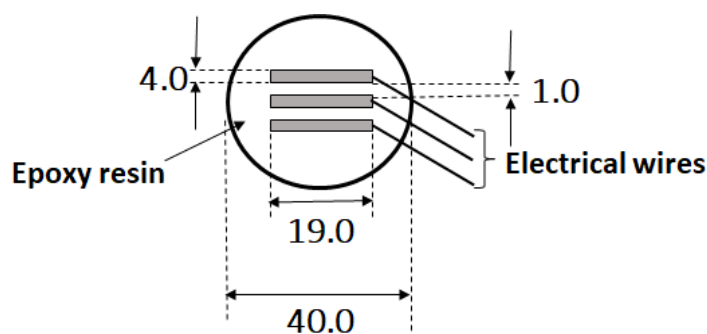


Figure 3-1: Schematic of the three identical steel coupons mounted in resin that were used for electrochemical tests. Dimensions are shown in mm.

3.2.2 Test procedures

A schematic of the test setup is shown in Figure 3-2. Two temperature conditions were applied: either a constant temperature of 80 °C (isothermal) or thermal cycling between 25 and 80 °C (cyclic). For thermal cycling, the temperature of the test solution was maintained at

25 °C for 4 h and then increased to 80 °C at 20 °C/min and maintained for 20 h. The temperature was reduced from 80 to 25 °C at 2.8 °C/min, and the same interval was applied when the temperature was increased from 25 to 80 °C. Two test durations were analysed (5 and 21 d). The initial pH of the test solution was 7.08 after the temperature reached a steady state at 80 °C. The pH of the condensed water in the gas phase was not obtained because the liquid volume was insufficient to measure the pH. Three weight-loss specimens and the electrochemical probe (Figure 3-2) were placed on the top level of a holder made from polytetrafluoroethylene (PTFE), and the samples were then exposed to the humid gas above the solution.

Once the test cell was assembled, the test solution (3.5 wt. % NaCl) was transferred to the cell, where it can come into contact with the samples in the top section. Although the temperature of the solution was 80 °C, the surface of the sample in the gas phase was 75.5 °C, as measured by a thermocouple. The size of the glass cell was 2 L and the height of the liquid was 100 mm. Three samples and an electrochemical probe were placed onto a sample holder 60 mm above the water line, whereas the other specimens and an electrochemical probe were immersed in the solution to a depth of 50 mm below the water line. The test cell was fitted with a condenser to prevent liquid loss. The test solution was mildly agitated with a PTFE-coated magnetic stirring bar to maintain the uniform temperature.

Two electrochemical methods (EIS and EN) were performed using the same probe (Figure 3-1) to monitor the corrosion activity of the steel samples. EIS was performed on the samples immersed in the solution using a multi-channel potentiostat (VSP300, Bio-Logic Science Instruments). The three identical carbon-steel coupons were used as working, reference, and counter electrodes. The sample was stabilised for 30 min at the open circuit potential (OCP) before an AC excitation voltage of 10 mV was applied over a frequency range of 100 kHz to 10 mHz at 10 points per decade. The impedance spectra were analysed using EC-lab software (Bio-logic. Inc.). EIS was conducted twice a day (approximately every 12 h) during the corrosion test period. EN measurements were conducted on both groups of samples (condensation and immersion) using a potentiostat operated in zero-resistance ammeter mode. The sampling frequency was 2 Hz. EN data were obtained over a period of 1 h twice a day (approximately every 12 h) during the corrosion test period.

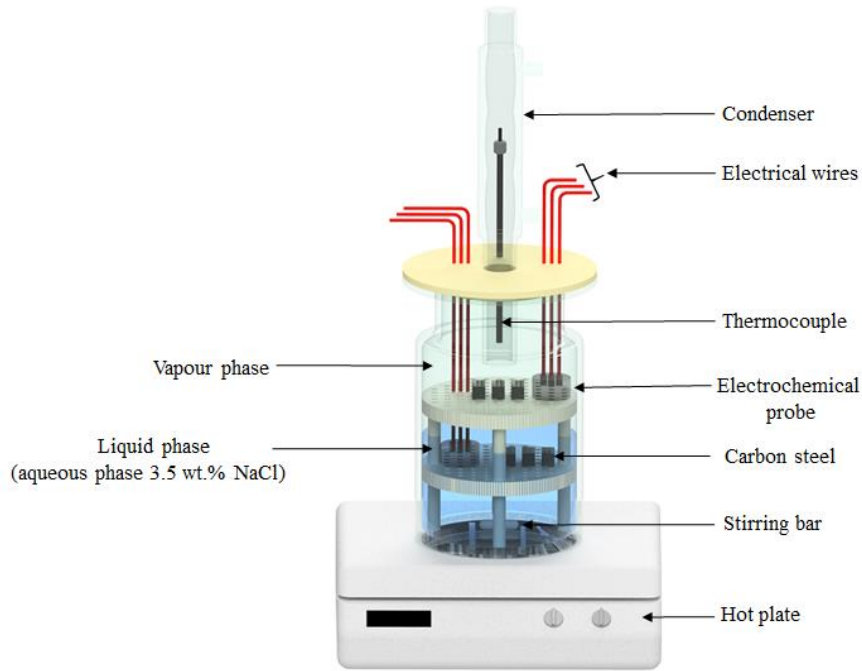


Figure 3-2: Schematic of the corrosion test setup for condensation and immersion conditions.

3.2.3 Post-test analysis

3.2.3.1 Weight loss method for determining the corrosion rate

After exposure to the corrosive environments, the corrosion products formed on the carbon steel surfaces were removed using Clark's solution ($\text{SnCl}_2 \cdot 2\text{H}_2\text{O}$ 59.5 g/L, Sb_2O_3 20 g/L, and 1000 mL of 32 wt. % HCl). The specimens were then air-dried before being weighed on an analytical balance with a precision of 0.1 mg following the procedures described in ASTM G1-03 [17]. The corrosion rate (CR ; $\text{mm} \cdot \text{y}^{-1}$) values were calculated as follows:

$$CR = \frac{K \times (W_0 - W_1)}{A \times T \times D} \quad (3-1)$$

Here, K is a constant corrosion rate ($87600 \text{ mm} \cdot \text{y}^{-1}$), W_0 (g) denotes the initial mass of a sample, W_1 (g) represents the final mass of the sample upon the removal of the rust layer, D ($\text{g} \cdot \text{cm}^{-3}$) is the density of carbon steel, A (cm^2) is the exposed surface area of the sample, and T (h) is the exposure time.

3.2.3.2 Localised corrosion analysed by surface profilometry

Surface profilometry was performed using optical microscopy (Infinite Focus G4, Alicona) to determine the extent of localised corrosion, based on the maximum pit depths. For

each condition, three samples were scanned to measure the maximum pit depth. The time-averaged pitting rate was calculated from Equation (3-2) to determine the penetration rate of the deepest pit on the metal surface for each exposure time (5 and 21 days).

$$\text{Pitting rate } \left(\frac{\text{mm}}{\text{y}} \right) = \frac{\text{pit depth } (\mu\text{m})}{\text{exposure time } (\text{d})} \times .0365 \quad (3-2)$$

3.2.3.3 Corrosion product characterisation

The morphology and elemental composition of the corrosion products were characterised by SEM; Mira Instrument, Tescan) combined with EDS. Aztec software (Oxford Instruments) was used to collect X-ray signals from the metal surface and analyse the elemental composition of the corrosion layers formed on the metal surfaces exposed to both the liquid and gas phases. Test specimens were mounted in resin and then cross-sectioned using an Accutom-50 system (Struers, Denmark), followed by polishing using 1200 grit SiC paper.

The chemical composition of the corrosion products was analysed by Raman spectroscopy (Labram 1B model, France). The samples were excited using a He–Ne laser with an excitation wavelength of 632.82 nm and power of 2 mW (full power). Spectra were collected using a 150 μm slit, 1100 μm confocal hole (fully open), 50 \times objective, 1800 lines/mm diffraction grating, and a Peltier-cooled charge-coupled device detector. The data collection time was 16 accumulations of 60 s each. The Raman shift was calibrated against the Raman line of silicon (wavenumber of 520.7 cm^{-1}).

3.3. Results and discussion

3.3.1 Uniform corrosion

The uniform corrosion rates were obtained from weight-loss measurements of three samples retrieved from the test cells after 5 and 21 days of testing under the different test conditions. The results are shown in Figure 3-3, where the error bars represent the standard deviation from the average of the three samples. After 5 d of exposure, the mean corrosion rate of the specimens immersed in the solution at 80 °C was the lowest (i.e., 0.3 $\text{mm}\cdot\text{y}^{-1}$). However, considering the standard deviations, the corrosion rates under all conditions, except that of the sample immersed at 80 °C, were not significantly different. The corrosion rates increased with time for all the samples under different exposure conditions. However, the highest corrosion rate after 21 d was observed for the immersed samples at 80 °C, with a value of 2.37 $\text{mm}\cdot\text{y}^{-1}$. As the corrosion kinetics are influenced by the exposure temperature, the

differences in the corrosion rates of the steel in the solution under isothermal and cycling conditions are attributed to the different times that the steel was exposed to high temperatures. Several factors affect the rate and extent of corrosion, including time, temperature, and ionic species (such as NaCl). The loss of metal increases over time and the concentration of the ionic species and temperature accelerate the corrosion process. In contrast, the steel samples tested under condensation conditions had similar weight-loss corrosion rates, regardless of the temperature conditions.

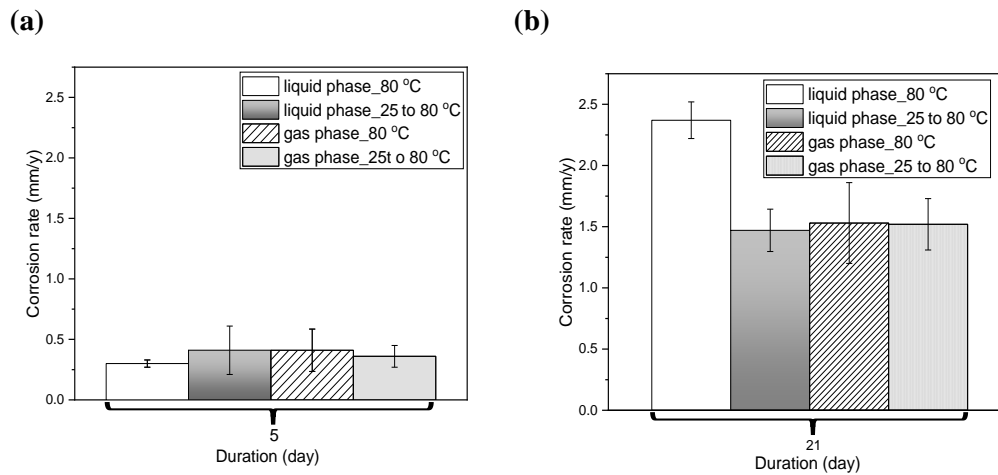


Figure 3-3: Uniform corrosion rates calculated from the weight loss of carbon steel tested under immersed or condensation conditions and isothermal or cyclic temperature profiles after (a) 5 d and (b) 21 d.

3.3.2 Localised corrosion

Figure 3-4 shows profilometry images of the corrosion samples after 21 d of exposure. The colour variations indicate features of different heights on the metal surface, where red indicates the deepest pits. Pitting corrosion was apparent for all samples, except those immersed in solution and subjected to thermal cycling. The most aggressive localised corrosion was observed for the condensation conditions, both isothermal and cyclic, as shown in Figure 3-4a and Figure 3-4c, respectively, and Table 3-1. The pit depth increased over time. For instance, the maximum pit depth measured for the isothermal condensation sample was 51 μm after 5 d of exposure, which increased to 185 μm after 21 d (Figure 3-5). The pitting rates determined from the pit depth and exposure time (Table 3-1) were lower for the immersion conditions than the condensation conditions. For instance, the pitting rate was 1.1 $\text{mm}\cdot\text{y}^{-1}$ for the isothermal immersion samples, while a rate of 3.7 $\text{mm}\cdot\text{y}^{-1}$ was measured for the isothermal condensation samples. A decrease in the pitting rate over time was observed for all conditions, except for the cyclic condensation samples, which exhibited an increase in the pitting rate over time from 1.6 to 2.2 $\text{mm}\cdot\text{y}^{-1}$. The calculated pitting factors, defined as the pitting rate divided by the weight-loss corrosion rate (ASTM G46 [17]), were 1.04 and 1.02

for the immersed samples after 21 d of exposure to isothermal and cycling conditions, respectively. The pitting factors close to one indicate uniform corrosion. For the condensation samples, the pitting factors were 1.96 and 1.32 for isothermal and cyclic conditions, respectively. Thus, the samples exposed to condensation conditions were more prone to localised corrosion than the immersed samples.

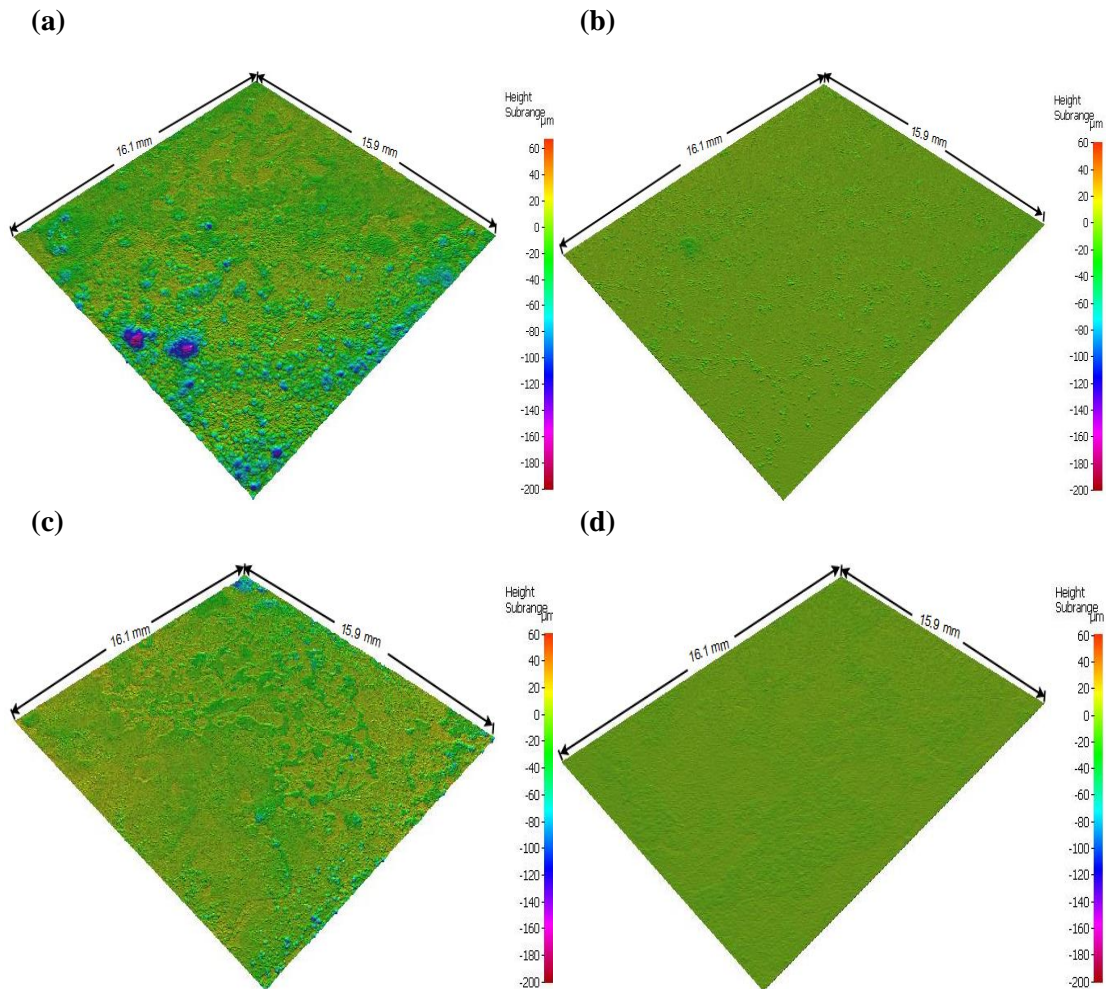


Figure 3-4: Surface height profiles of the carbon steel samples after 21 d of exposure to (a) isothermal condensation, (b) isothermal immersion, (c) cyclic condensation, and (d) cyclic immersion conditions

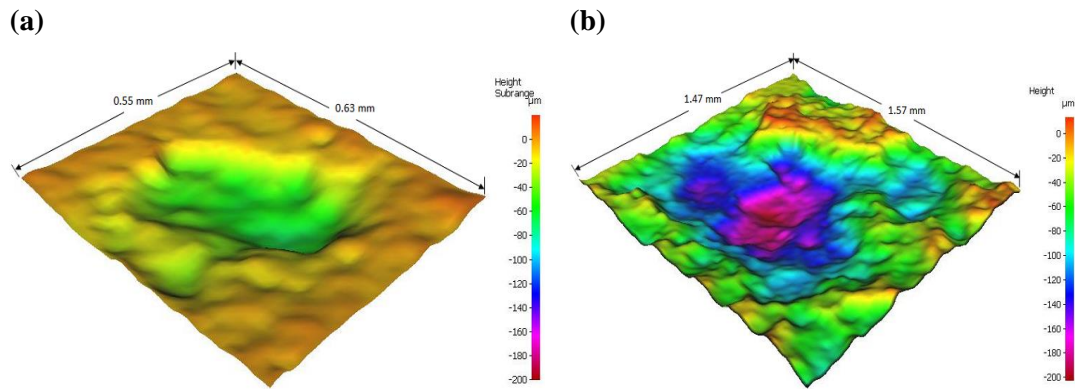


Figure 3-5: Surface height profiles of the deepest pit in the carbon steel exposed to isothermal condensation conditions after (a) 5 d and (b) 21 d of exposure

Table 3-1: Maximum pit depths and local corrosion rates of the samples exposed to various corrosion conditions.

<u>Condition</u>	<u>Exposure time</u>	
	<u>5 d</u>	<u>21 d</u>
	Depth (μm)/ pitting rate ($\text{mm}\cdot\text{y}^{-1}$)	Depth (μm)/ pitting rate ($\text{mm}\cdot\text{y}^{-1}$)
Isothermal immersion	15 / 1.1	43 / 0.7
Cyclic immersion	6 / 0.4	16 / 0.3
Isothermal condensation	51 / 3.7	185 / 3.2
Cyclic condensation	22 / 1.6	124 / 2.2

3.3.3 Corrosion product layer

3.3.3.1 Morphology and composition

Figure 3-6 shows cross-sectional SEM images of the steel coupons after corrosion tests. Local corrosion (circled areas) is observed for all samples, except the cyclic immersion group, which shows a uniform oxide layer covering the metal surface with no observable pits. Three layers of corrosion product are apparent on this sample. The inner and outer layers are uniform and compact, while the intermediate film is porous. The thickness of the corrosion product is $\sim 75\text{--}100\ \mu\text{m}$, which is markedly thicker than those formed under other conditions. An SEM image of the top surface of this sample is shown in Figure 3-7. A uniform corrosion-product film creates a physical barrier against the diffusion of oxygen and corrosive ions, which reduces the corrosion rate and the tendency for local corrosion.

The cross-sectional SEM images show that the corrosion product layers are thinner than that of the cyclic immersion group for all other test conditions. The layer thicknesses

varied from a few μm to 20 μm and some areas showed no visible corrosion products. In addition, cracks were observed in the corrosion product layer, as shown in Figure 3-8. Although the cracks could have developed as the samples dried, it is worth noting that all specimens were prepared and processed the same way and no cracks were observed for the samples without localised corrosion.

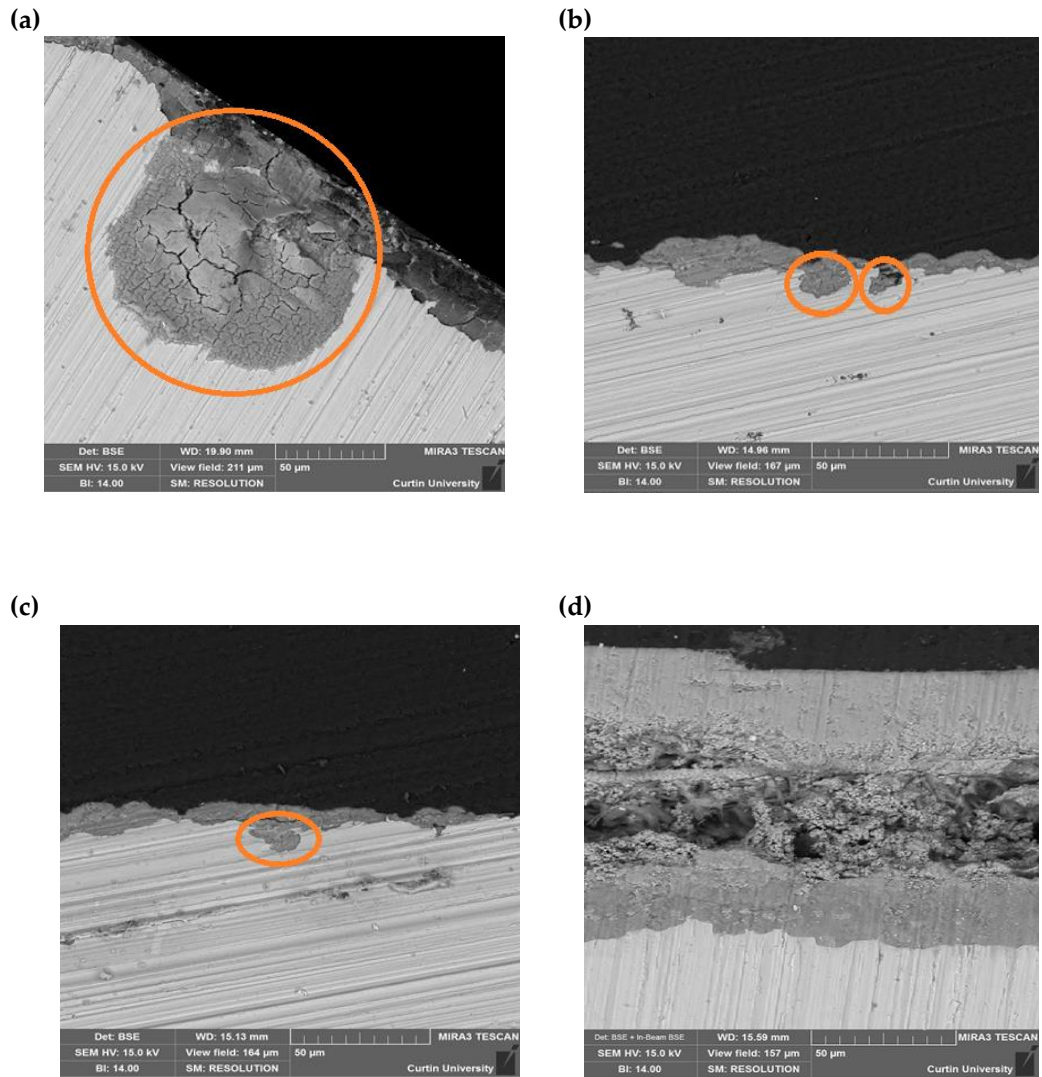


Figure 3-6: Cross-sectional SEM images of corrosion-product layers formed on the (a) isothermal condensation, (b) isothermal immersion, (c) cyclic condensation, and (d) cyclic immersion samples. The circled areas indicate areas of local corrosion.

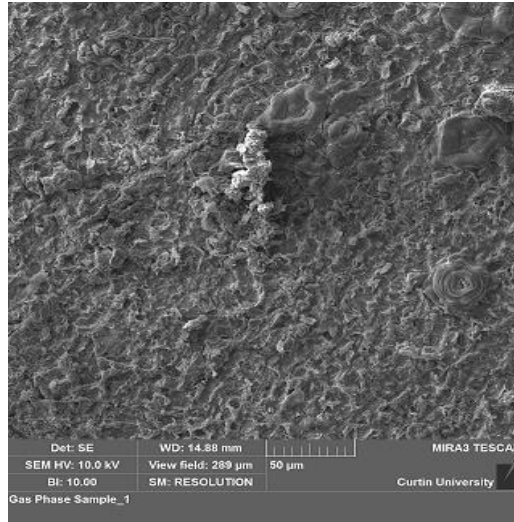


Figure 3-7: SEM image of the surface of the corrosion product layer on the cyclic immersion sample after 21 d.

Figure 3-7 and 3-8 show the corrosion morphologies of carbon steel exposed to different concentrations of the NaCl solution and temperature. The corrosion product became heavier and thicker in higher concentrations of NaCl and under thermal cycling. The corrosion morphologies are consistent with the corrosion rates and localised corrosion depths. The highest corrosion rate was observed for the samples with thinner and cracked corrosion-product layers.

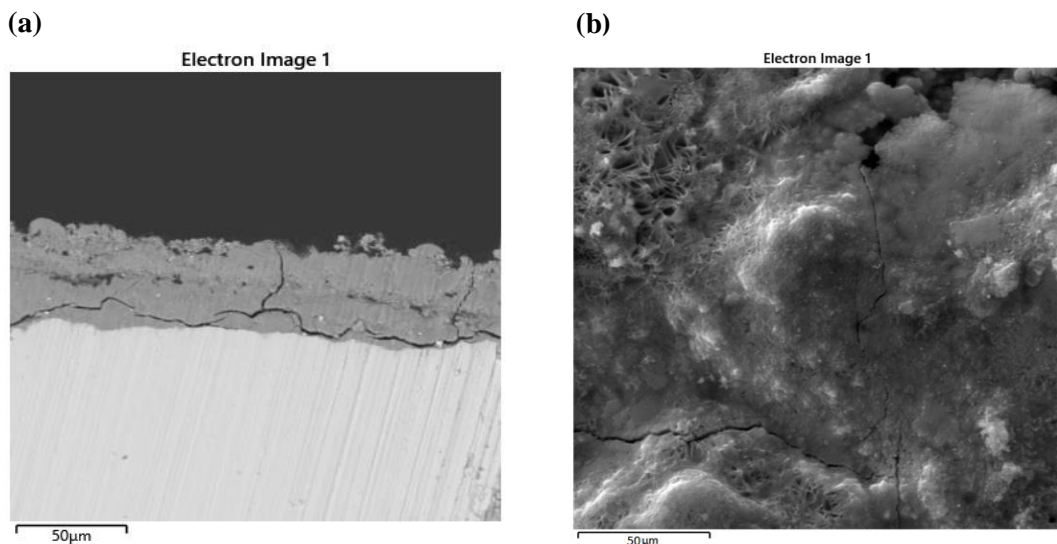
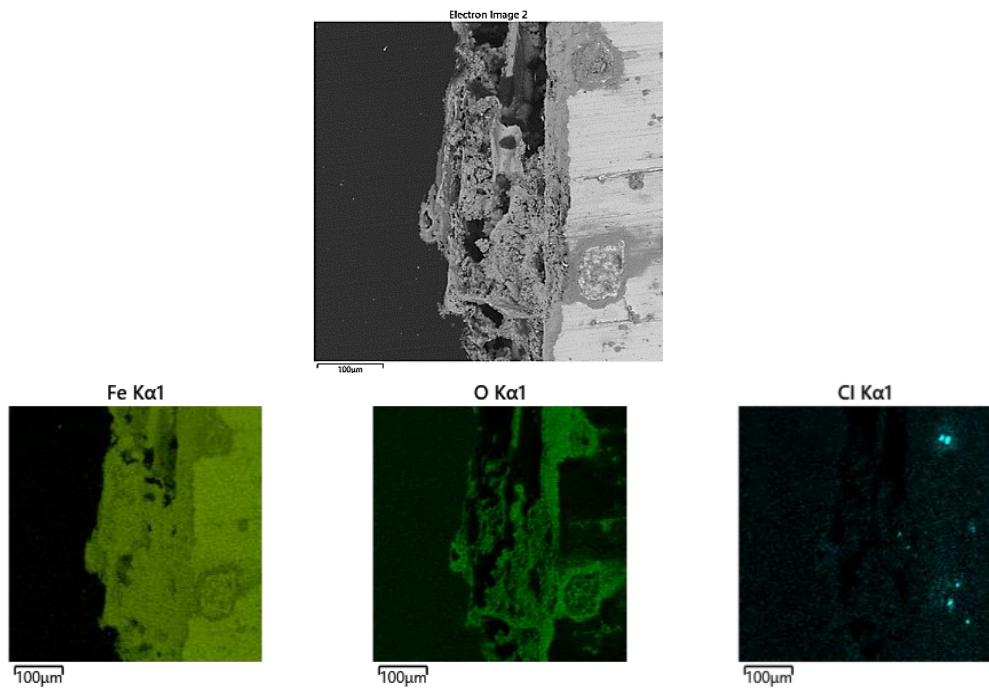


Figure 3-8: (a) Cross-sectional and (b) surface SEM images of carbon steel after 21 d of isothermal immersion.

EDS maps of the corrosion products formed on the samples exposed to isothermal immersion and condensation conditions are shown in Figure 3-9a and 3-9b, respectively. The colour intensity is proportional to the concentration of the target element in the analysed region. In both cases, the corrosion product layer consists of only iron and oxygen, consistent with iron oxide. Chloride was identified only inside the corrosion pits and its concentration was highest at the bottom of the pit and decreased consistently toward the pit edges. A previous study showed that during pitting corrosion of carbon steel exposed to chloride ions, FeCl_3 accumulated in the centre of the pit cavity and was laterally walled by iron oxides [4]. The diffusion of iron ions away from the active pit surface controls further pit growth. Iron oxides form the exterior wall of the pit, creating a diffusion barrier for mass transport that maintains concentrated local chemistry, thereby providing suitable conditions for pit growth.

(a)



(b)

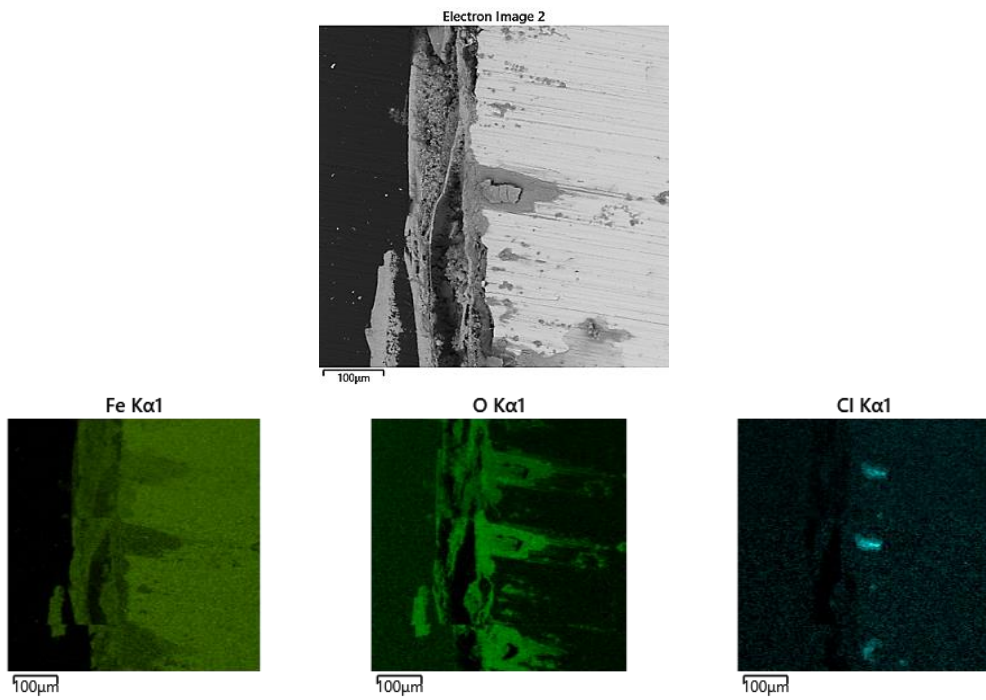


Figure 3-9: EDS maps of the corrosion product layers formed on the metal surfaces after 21 d of exposure to isothermal (a) immersion and (b) condensation conditions.

3.3.4 Chemical composition

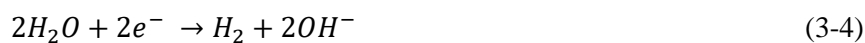
Figure 3-10 shows the Raman spectra of the top layer of the corrosion products formed on the specimen surfaces after 21 d of exposure to the various corrosion conditions. Strong peaks are observed at 225, 250, 290, 293 and 379 cm^{-1} , and moderate peaks are observed at 411, 412, 528, 611 and 650 cm^{-1} . These peaks are consistent with those of hematite ($\alpha\text{-Fe}_2\text{O}_3$) and lepidocrocite ($\gamma\text{-FeOOH}$) as the major corrosion products on steel surfaces [18-22]. For all specimen groups, the strongest peaks in the Raman spectra are narrow doublet peaks at 225 and 290–293 cm^{-1} , with weaker broad peaks formed at approximately 411, 412 and 415 cm^{-1} . These findings indicate that the major corrosion product on the steel specimens was $\alpha\text{-Fe}_2\text{O}_3$ [19-20]. In the case of the cyclic immersion sample (Figure 3-10d), additional characteristic peaks are observed at 250, 379, and 528 cm^{-1} , indicating the presence of $\gamma\text{-FeOOH}$ [18-22] in addition to $\alpha\text{-Fe}_2\text{O}_3$. Note that other iron corrosion products could have formed within the corrosion-product layer or near the metal surface, which could not be detected by Raman spectroscopy due to its limited depth range.

It is also noted that under isothermal conditions, the pH of the immersion liquid at the end of the experiment was 5.19 (measured at 80 °C), which is more acidic than the original solution. In contrast, the solution used for cyclic tests had a final pH of 6.43 (at 80 °C). This variation in solution acidity may have contributed to the observed differences in the local corrosion tendency under the two different temperature profiles.

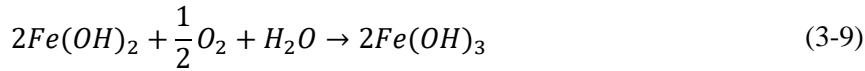
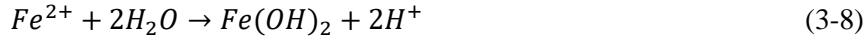
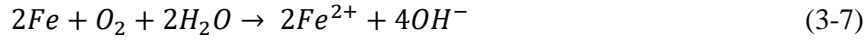
From the analysis of the pits and corrosion products, the following corrosion reaction at the anode is proposed:



Three main cathodic reactions can occur (equations (3-4) to (3-6)). At neutral pH and OCP, water and hydrogen reduction reactions (equations (3-5) and (3-6)) can be neglected. Thus, oxygen reduction (equation (3-4)) was the dominant cathodic reaction under the conditions used in this study.



The formation of $\text{Fe}(\text{OH})_2$ as the corrosion product (equation (3-8)) results in the production of H^+ [23-24]. $\text{Fe}(\text{OH})_2$ is then further oxidised in the presence of dissolved oxygen (equation (3-9)). Equation (3-7) is equivalent to equations ((3-3) and (3-6))



Then, the following reaction occurs to form an initial rust layer composed of $\gamma\text{-FeOOH}$:



On the initial rust layer, $\gamma\text{-FeOOH}$ steadily forms in a solution containing NaCl. The $\gamma\text{-FeOOH}$ corrosion layer played a major role in the development of the corrosion-product layer in wet conditions. Akaganeite ($\beta\text{-FeOOH}$) starts to form after the formation of $\gamma\text{-FeOOH}$ in the presence of chloride ions [25], which were detected in the centre of the corrosion pits in this study (Figure 3-9). The local acidification due to the diffusion of chloride ions balances the positive charge of Fe^{2+} generated by corrosion [13]. The microenvironment in the pit is characterised by a low pH and high Cl^- concentration, which aggravate corrosion [26]. Finally, $\gamma\text{-FeOOH}$ is transformed into $\alpha\text{-Fe}_2\text{O}_3$ as a more stable oxide [27-28].



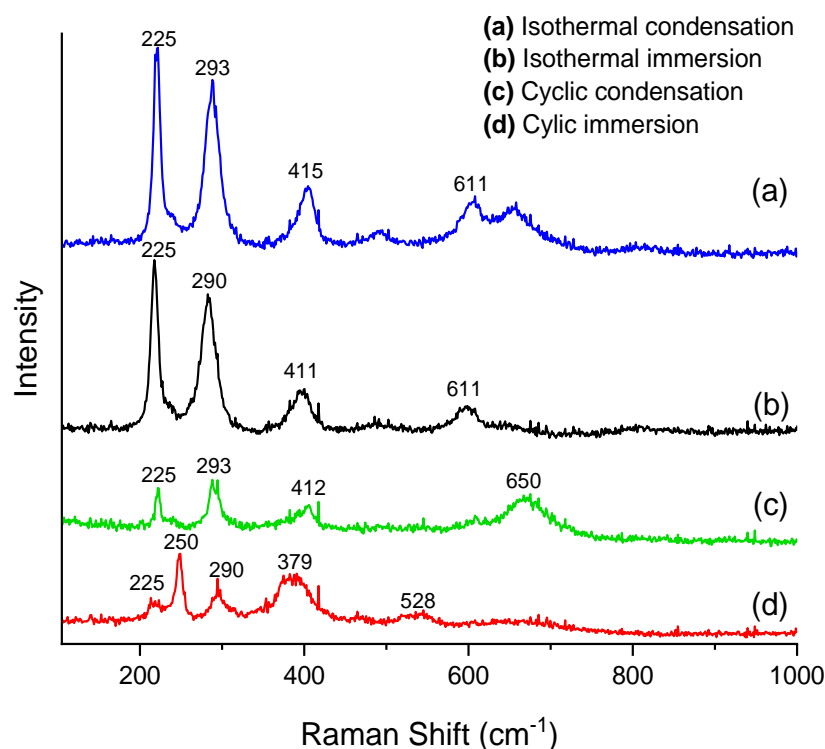


Figure 3-10: Raman spectra of corrosion-product layers formed on the steel specimens after 21 d of exposure to the various corrosion conditions.

3.3.5 Electrochemical behaviour

The Nyquist curves in Figure 3-11 show only one semicircle, related to double-layer capacitance, which varies significantly as a function of immersion time. The impedance magnitude of the semicircle in the curves measured for the cyclic corrosion samples increased gradually, implying a decrease in the corrosion rate, which could be attributed to a thicker rust layer (Figure 3-6). It is inferred that the corrosion rate of carbon steel in a 3.5 wt. % NaCl solution during thermal cycling is limited by the diffusion of the electrolyte through the oxide layer. The effect of this layer became significant after 9 d, evidenced by the high impedance (Figure 3-11). The corrosion product did not effectively reduce the corrosion rate during the first 5 d, but a significant reduction was observed after 21 d for the isothermal immersion samples, with a rate of $0.8 \text{ mm}\cdot\text{y}^{-1}$ (Figure 3-3). Under isothermal immersion conditions, the impedance changes between 14 and 21 d could indicate changes in the corrosion layer, such as the growth of cracks, as shown in Figure 3-8. As the layer of corrosion products formed under these conditions was porous and thin, it was likely ineffective in hindering the diffusion of chloride ions, resulting in localised corrosion.

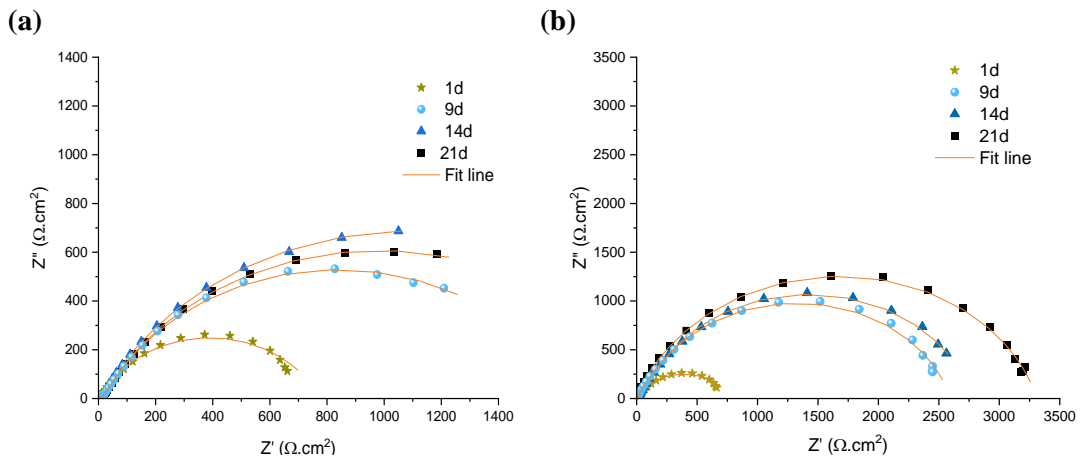


Figure 3-11: Nyquist plots of steel specimens after immersion for various periods in 3.5 wt. % NaCl solution under (a) isothermal or (b) cyclic conditions.

The electrical equivalent circuit shown in Figure 3-13 was used to fit the EIS curves, and the good fits prove that this circuit is suitable [29-30]. In the circuit, Q_C is a constant phase element (CPE) of a corrosion product, R_S is the solution resistance, and R_C is the resistance of the corrosion product. The CPE of the electrical double layer is denoted as Q_{dl} and the charge transfer resistance is represented as R_{ct} . The extracted parameters are listed Table 3-2 and Table 3-3 for the isothermal and cyclic immersion data, respectively. In the case of the isothermal samples, R_S is between 5.0 and 5.81 $\Omega \cdot \text{cm}^2$ and did not change significantly over time. Comparing the R_C values shows that thermal cycling resulted in the highest resistance (1132 $\Omega \cdot \text{cm}^2$ after 21 d), consistent with a thicker corrosion product. After 14 d, R_C decreased (300 $\Omega \cdot \text{cm}^2$), indicating a less homogeneous and more porous iron oxide film, consistent with the intermediation layer in the cross-sectional SEM image in Figure 3-6d. However, the R_C values of the isothermal samples fluctuated, consistent with the changes in the morphology and thickness of the corrosion product (e.g., Figure 3-6b). The R_{ct} increased from 478 to 2177 $\Omega \cdot \text{cm}^2$ after 21 d of thermal cycling, which is attributed to a decrease in weight loss compared with that of the isothermal sample. In the case of the isothermal sample, compared to day 1, the R_{ct} values were lower after 9 and 14 d of corrosion, confirming an increase in weight loss over time (Figure 3-3b).

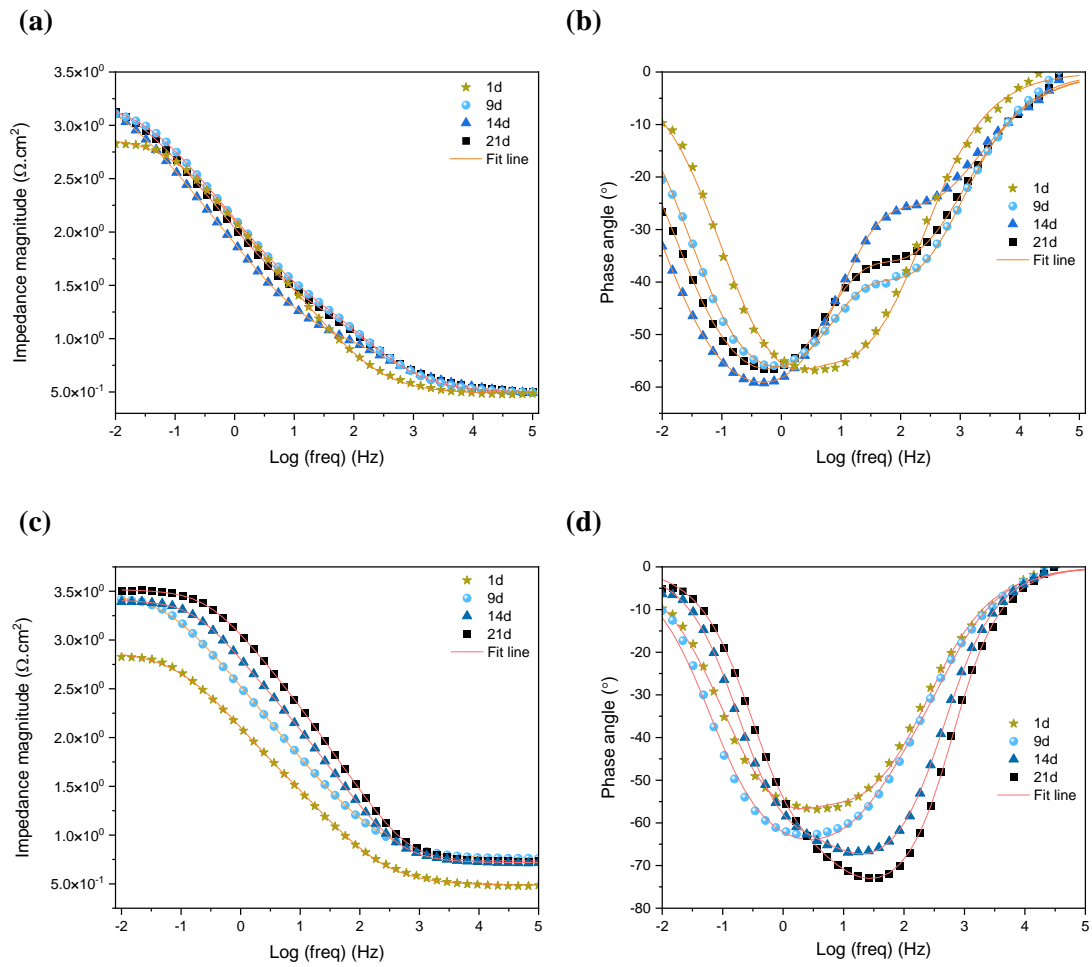


Figure 3-12: Bode plots: (a,c) impedance and (b,d) phase angle of steel specimens after immersion for various periods in 3.5 wt.% NaCl solution under (a,b) isothermal or (c,d) cyclic conditions.

The final curves measured after 21 d of immersion were fit using the circuit shown in Figure 3-13.

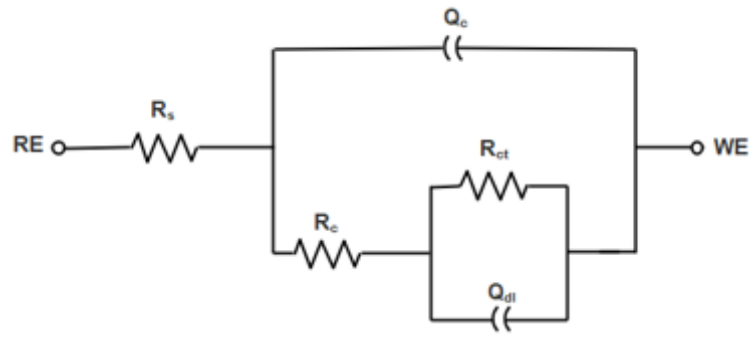


Figure 3-13: Equivalent circuit used for fitting the EIS data.

Table 3-2: EIS fitting parameters for the cyclic immersion samples.

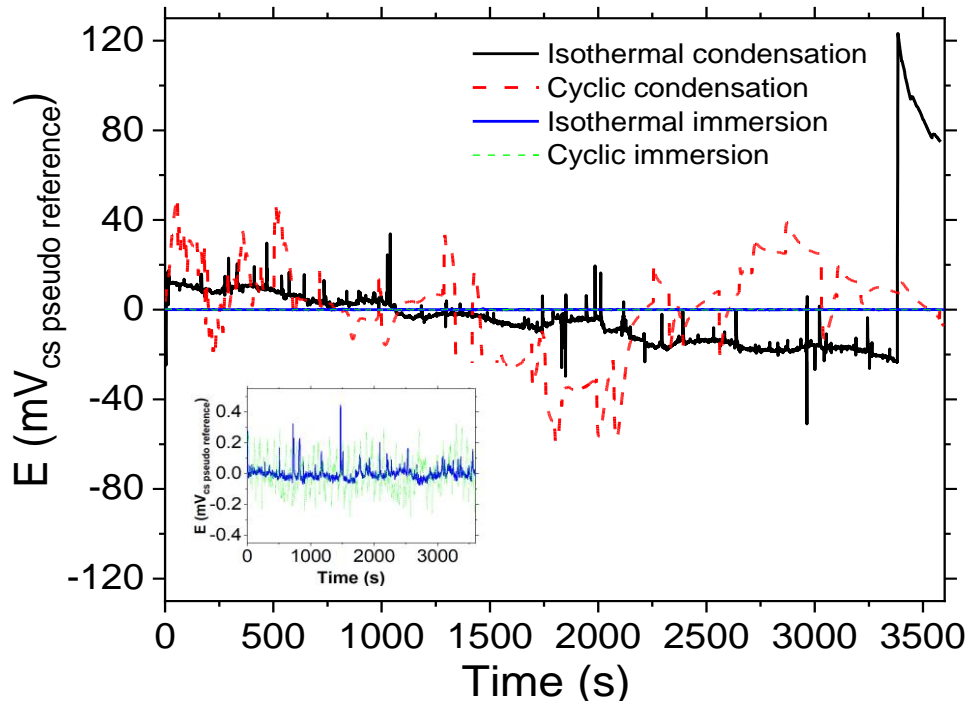
<i>Duration</i> (day)	R_s ($\Omega \cdot \text{cm}^2$)	Q_c ($\text{F} \cdot \text{s}^{\alpha-1} \cdot \text{cm}^{-2}$)	n_c	R_c ($\Omega \cdot \text{cm}^2$)	Q_{ct} ($\text{F} \cdot \text{s}^{\alpha-1} \cdot \text{cm}^{-2}$)	n_{ct}	R_{ct} ($\Omega \cdot \text{cm}^2$)	X^2
1	5.05	0.18×10^{-2}	0.76	296.2	0.27×10^{-3}	0.71	478.4	0.104
9	5.21	0.24×10^{-3}	0.84	737	0.151×10^{-3}	0.82	1854	0.044
14	5.81	0.39×10^{-3}	0.85	300	0.41×10^{-3}	0.84	2470	0.027
21	5.42	0.114×10^{-3}	0.89	1132	0.125×10^{-3}	0.74	2177	0.036

Table 3-3: EIS fitting parameters for the isothermal immersion samples.

	R_s ($\Omega \cdot \text{cm}^2$)	Q_c ($\text{F} \cdot \text{s}^{\alpha-1} \cdot \text{cm}^{-2}$)	n_c	R_c ($\Omega \cdot \text{cm}^2$)	Q_{ct} ($\text{F} \cdot \text{s}^{\alpha-1} \cdot \text{cm}^{-2}$)	n_{ct}	R_{ct} ($\Omega \cdot \text{cm}^2$)	X^2
1	3.0	0.79×10^{-3}	0.76	33.1	0.58×10^{-1}	0.97	900	0.455
9	3.01	0.12×10^{-2}	0.75	1466	0.015×10^{-1}	0.94	106.2	0.035
14	3.02	0.71×10^{-3}	0.72	1426	0.24×10^{-1}	0.86	1629	0.024
21	3.13	0.88×10^{-3}	0.703	1390	0.157×10^{-3}	0.743	885.3	0.0046

Typical EN signals obtained for the specimens treated under the various corrosion conditions are shown in Figure 3-14. The magnitudes of the potential signals are significantly lower for the immersion samples than the condensation samples (inset of Figure 3-14a). The measured potential is the potential difference between a couple of carbon steel electrodes and the third steel electrode (same material and geometry). The condensation samples had a thinner electrolyte layer on the surface of the three electrodes and the surface coverage of electrolyte may be different between samples, resulting in a larger potential difference. In contrast, when the test probe comprising the three steel electrodes was fully immersed in the liquid phase, the electrolyte coverage of all three electrodes is the same, resulting in a small potential difference. The magnitudes of the current signals show an opposite trend, i.e., a larger current signal was measured for the immersion case than the condensation case.

(a)



(b)

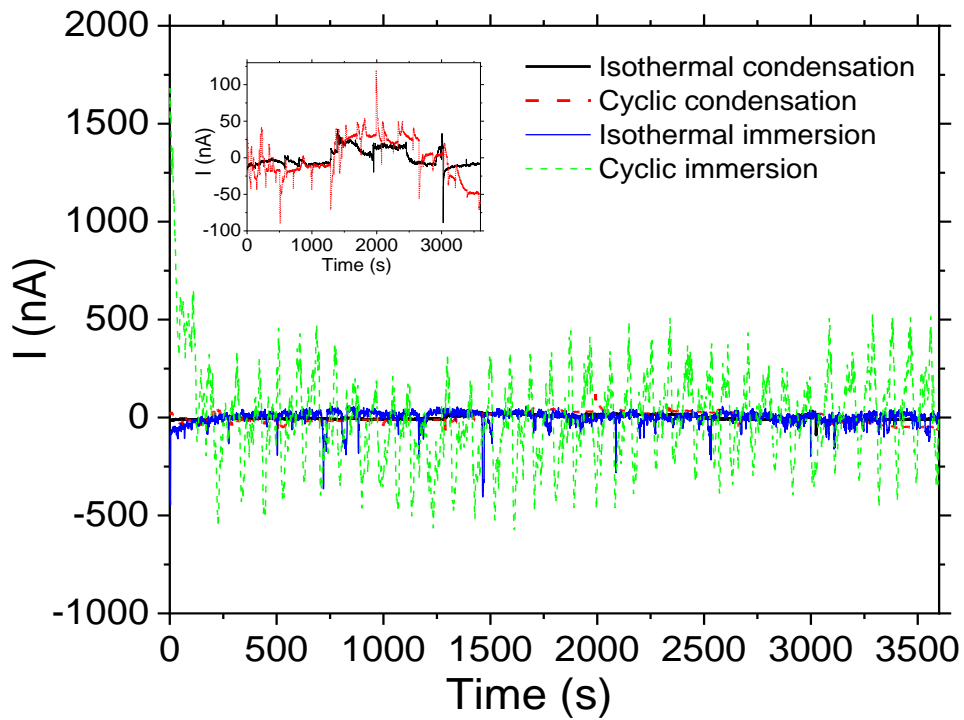


Figure 3-14: EN (a) potential difference and (b) current signals recorded on day 21 for immersed and condensation conditions. The insets show magnified views of selected data to aid readability.

In EN signals, the shape and frequency of the transients are correlated with different corrosion mechanisms. Figure 3-15 shows the details of the typical transients extracted from the EN signals displayed in Figure 3-14. The sharp increase/decrease followed by a slow decrease/increase in current and potential indicate the initiation and propagation of pitting [31]. Such transients were observed for all samples (Figure 3-15(a-c)) as indicated by the green boxes, except for the cyclic immersion sample (Figure 3-15 (d)). Therefore, it is inferred that the steel samples exposed to thermal cycling and immersion underwent uniform corrosion [32], while the other systems were dominated by localised corrosion over the test period. In the case of isothermal immersion (Figure 3-15 (c)), the duration of the current transient indicated by the green box is ~30 s, and the current decreased to the baseline before the next transient began. In comparison, for the condensation samples (Figure 3-15 (a, b)), the high current was not able to return to the original value before the next current increase event occurred. This could be related to the growth of the pit, resulting in larger localised corrosion depths [33]. This is consistent with the maximum localised corrosion depth values measured for the weight loss samples (Table 3-1), which show that the steel samples exposed to condensation conditions had deeper corrosion pits than those exposed to immersion conditions.

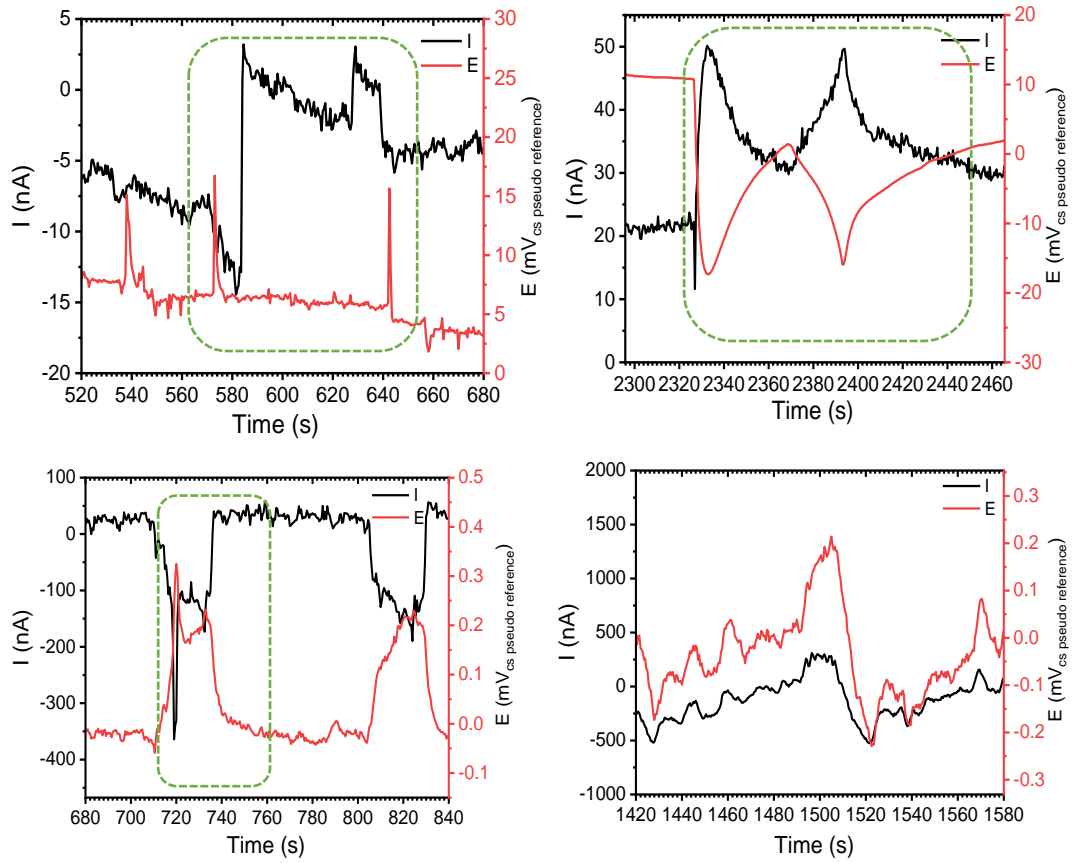


Figure 3-15: Typical current and potential transients associated with the EN signals for steel samples subjected to (a) isothermal condensation, (b) cyclic condensation, (c) isothermal immersion, and (d) cyclic immersion corrosion conditions.

3.4. Conclusions

This case study investigated the corrosion behaviour of carbon steel under simulated closed environments (fully immersed in 3.5 wt. % NaCl solution or exposed to condensation conditions). The effect of isothermal or cyclic temperature conditions (up to a maximum temperature of 80 °C) was investigated. Based on the results, the following conclusions were drawn.

- Localised corrosion was observed on the surfaces of the samples corroded under condensation conditions, while uniform corrosion was dominant for the immersed samples.
- Thermal cycling appears to promote the formation of a protective corrosion-product layer on the carbon steel surface, thus creating an effective barrier and reducing the extent of localised corrosion under immersion conditions.
- Hematite was the dominant corrosion product under all conditions. Lepidocrocite was detected only on the immersed sample under thermal cycling.

3.5. References

- [1] M. May, "Corrosion behavior of mild steel immersed in different concentrations of NaCl solutions," *J. Sebha Univ.*, vol. 15, p. 13, 2016.
- [2] F. S. Kadhim, "Investigation of Carbon Steel Corrosion in Water Base Drilling Mud," *Mod. Concepts Mater. Sci.*, vol. 5, pp. 224–229, 2011.
- [3] O. J. Murphy, J. O. Bockris, T. E. Pou, L. L. Tongson, and M. D. Monkowski, "Chloride Ion Penetration of Passive Films on Iron," *J. Electrochem. Soc.*, no. 130, 1792-1794, 1983.
- [4] Q. Song, X. Wang, B. Pan, and L. Wan, "Effect of relative humidity on corrosion of Q235 carbon steel under thin electrolyte layer in simulated marine atmosphere," *Anti-Corrosion Methods Mater.*, no. 67, 187-196, 2020.
- [5] S. L. Clegg and P. Brimblecombe, "The solubility and activity coefficient of oxygen in salt solutions and brines," *Geochim. Cosmochim. Acta*, no. 54, 3315-3328, 1990.
- [6] K. Gao, S. Shang, Z. Zhang, Q. Gao, J. Ma, and W. Liu, "Effect of Temperature on Corrosion Behavior and Mechanism of S135 and G105 Steels in CO₂/H₂S Coexisting System," *Metals (Basel)*, no. 12, 1848., 2022.
- [7] M. Esmaily *et al.*, "Influence of temperature on the atmospheric corrosion of the Mg-Al alloy AM50," *Corros. Sci.*, no. 90, 420–433, 2015.
- [8] M. Chiba, S. Saito, H. Takahashi, and Y. Shibata, "Corrosion of Al alloys in repeated wet-dry cycle tests with NaCl solution and pure water at 323 K," *J. Solid State Electrochem.*, no. 19, 3463–3471, 2015.
- [9] M. Chiba, S. Saito, K. Nagai, H. Takahashi, and Y. Shibata, "Effect of NaCl concentration on corrosion of Al alloy during repeated wet–dry cycle tests at 323 K—comparing with corrosion in immersion tests-," in *Surface and Interface Analysis*, 2016, pp. 48,767-774.
- [10] Y. Cai, Y. Zhao, X. Ma, K. Zhou, and Y. Chen, "Influence of environmental factors on atmospheric corrosion in dynamic environment," *Corros. Sci.*, no. 137, 163–175, 2018.
- [11] B. Zhang *et al.*, "Unmasking chloride attack on the passive film of metals," *Nat. Commun.*, no. 9, 2559, 2018.
- [12] T. P. Hoar, "The production and breakdown of the passivity of metals," *Corros. Sci.*,

- no. 7, 341–355, 1967.
- [13] T. P. Hoar, D. C. Mears, and G. P. Rothwell, “The relationships between anodic passivity, brightening and pitting,” *Corros. Sci.*, no. 5, 279–289, 1965.
- [14] N. Sato, “A theory for breakdown of anodic oxide films on metals,” *Electrochim. Acta*, no. 16, 1683–1692, 1971.
- [15] J. R. Galvele, “Transport Processes and the Mechanism of Pitting of Metals,” *J. Electrochem. Soc.*, no. 123,464, 1976.
- [16] Astm a 36/a 36M-05, “Standard Specification for Carbon Structural Steel,” *ASTM West Conshohoken, PA, USA*, 2005.
- [17] ASTM G1-03, “ASTM G1 - 03 Standard practice for preparing, cleaning, and evaluating corrosion test specimens.,” *ASTM West Conshohoken, PA, USA*, 2003.
- [18] L. Bellot-Gurlet, D. Neff, S. Réguer, J. Monnier, M. Saheb, and P. Dillmann, “Raman studies of corrosion layers formed on archaeological irons in various media,” 2009, pp. 8, 147–156.
- [19] R. M. Cornell and U. Schwertmann, *The Iron Oxides: Structures, Properties, Reactions, Occurrences and Uses*. Germany: Wiley-VCH:, 2003.
- [20] F. Froment, A. Tournié, and P. Colomban, “Raman identification of natural red to yellow pigments: Ochre and iron-containing ores,” *J. Raman Spectrosc.*, no. 39, 560–568, 2008.
- [21] B. Lafuente, R. T. Downs, H. Yang, and N. Stone, *RRUFFTM Project*. De Gruyter: Berlin, Germany, 2015.
- [22] M. Hanesch, “Raman spectroscopy of iron oxides and (oxy)hydroxides at low laser power and possible applications in environmental magnetic studies,” *Geophys. J. Int.*, no. 177, 941–948, 2009.
- [23] L. Xu, Y. Xin, L. Ma, H. Zhang, Z. Lin, and X. Li, “Challenges and solutions of cathodic protection for marine ships,” *Corrosion Communications*. 2, 33-40, 2021.
- [24] J. Jiang, Y. Xie, M. A. Islam, and M. M. Stack, “The Effect of Dissolved Oxygen in Slurry on Erosion–Corrosion of En30B Steel,” *J. Bio- Tribo-Corrosion*, no. 3, 45, 2017.
- [25] J. Jun, G. S. Frankel, and N. Sridhar, “Further Modeling of Chloride Concentration and Temperature Effects on 1D Pit Growth,” *J. Electrochem. Soc.*, no. 163, C823, 2016.

- [26] G. S. Frankel, "Pitting Corrosion of Metals: A Review of the Critical Factors," *J. Electrochem. Soc.*, vol. 145, 2186, 1998.
- [27] X. Zhang, K. Xiao, C. Dong, J. Wu, X. Li, and Y. Huang, "In situ Raman spectroscopy study of corrosion products on the surface of carbon steel in solution containing Cl⁻ and SO₄²⁻," *Eng. Fail. Anal.*, no. 18, 1981–1989, 2011.
- [28] E. Paterson, "The Iron Oxides. Structure, Properties, Reactions, Occurrences and Uses," *Clay Miner.*, 1999.
- [29] M. Yang and J. Liu, "In Situ Monitoring of Corrosion under Insulation Using Electrochemical and Mass Loss Measurements," *Int. J. Corros.*, vol. 2022, 668-, 2022.
- [30] C. Li, Y. Ma, Y. Li, and F. Wang, "EIS monitoring study of atmospheric corrosion under variable relative humidity," *Corros. Sci.*, no. 52, 3677–3686, 2010.
- [31] R. A. Cottis, "Interpretation of electrochemical noise data," *Corrosion*, vol. 57, no. 3, p. 22, 2001.
- [32] A. Legat and V. Doleček, "Corrosion Monitoring System Based on Measurement and Analysis of Electrochemical Noise," *CORROSION*, no. 51, 295–300, 1995.
- [33] C. Comas, F. Huet, K. Ngo, M. Fregonese, H. Idrissi, and B. Normand, "Corrosion propagation monitoring using electrochemical noise measurements on carbon steel in hydrogenocarbonated solution containing chloride ions," *Corros. Sci.*, no. 193, 109885, 2021.

CHAPTER 4

S. Ahmed, K. Lepkova, Xiao Sun, T. Pojtanabuntoeng, The performance of phenolic epoxy coating after exposure to high temperatures, Journal of corrosion and materials degradation, under revision.

This chapter presents the submitted manuscript with modified formats and contents that match the overall style of the thesis.

Performance of Phenolic-Epoxy Coatings after Exposure to High Temperatures

Abstract

Phenolic-epoxy coatings, which are designed to protect substrates from thermal damage, are widely applied in many fields. There remains an inadequate understanding of how such coatings change during their service life after exposure to various temperature conditions. To further elucidate this issue, this case study investigated the effects of high temperatures on carbon steel panels coated with phenolic epoxy and exposed to different heating conditions. A general trend of decreasing barrier performance was observed after exposure to 150 °C for 3 d, as evidenced by the appearance of cracks on the panel surfaces. In contrast, the coating performance improved after exposure to isothermal conditions (120 °C) or thermal cycling from room temperature to 120 °C, as indicated by the increased low-frequency impedance modulus values of the coating. This unexpected improvement was further examined by characterising the coatings using FTIR, TGA, DSC, pull-off adhesion tests, and ToF-SIMS. The maximum pull-off adhesion force (24.9 ± 3.6 MPa) was measured after thermal cycling for 40 d.

Keywords: Carbon steel; EIS; ToF-SIMS; Phenolic epoxy; Pull-off adhesion.

4.1 Introduction

Corrosion protection of metallic substrates is a traditional application of organic coatings, which remains one of the most cost-effective means of providing practical corrosion protection. Controlling corrosion by applying coatings is very important, especially for structures that are subjected to corrosive environments during use. If failure of the protective coating occurs, the functionality of the coated structure can be threatened. The main goal of corrosion-protection coatings is to provide long-term protection to increase the practical service life of the substrate [1]. In certain applications, the coating must be sufficiently flexible to withstand deformation due to thermal expansion/contraction. Cracks must not occur during heating after the coating is cured, as this indicates the degradation of the polymer coating, which may result in eventual adhesive failure [2].

Epoxy coatings are two-component systems consisting of an epoxy compound and a hardener, which react to form a cured network [3]. Phenolic epoxy coatings are an effective and inexpensive method for providing protection against thermal damage and CUI [4]. The polymer cross-links to form a network during curing, resulting in a coating with high resistance to heat and the diffusion of corrosive substances, which is considered an important factor governing the physical properties of the cured resin and corrosion resistance, particularly for amine- or anhydride-cured epoxy resins [5]. However, there is no clear consensus on the effect of cross-linking on the coating performance, partly because the methods for changing the cross-linking density introduce problems, such as changes in the chemical structure of epoxy resin or hardener when exposed to high temperatures [6]. This can damage the polymer network by chemical bond scission (chain scission), which creates small molecular fragments [2].

The aim of this case study was to evaluate the behaviour of a phenolic epoxy under thermal exposure. Many methods were used to characterise the chemical and physical changes in the phenolic epoxy, such as pull-off adhesion, EIS, TGA, DSC, FTIR, and ToF-SIMS. These methods provided information about the cross-linked structures after the degradation of the epoxy coatings and the thermal stability of the coatings under different conditions.

4.2 Experiments

4.2.1 Materials

Carbon steel plates (A3678/ Grade 250) with a nominal composition of 0.04 C, 0.2 Si, 5.5 M, 0.005 P, 0.003 S, 0.03 Al, 0.22 Mo, 0.30 Ni, 0.39 Cr, and balance of Fe (wt.%), and dimensions of 170 mm × 50 mm × 6 mm were used as substrates. The steel plates were coated with a commercial amine-cured phenolic-epoxy coating (Dulux coating company, Australia).

The chemical composition of the hazardous constituents from the SDS of the coating is shown in Table 4-1. The supplier applied one layer of the epoxy coating to the carbon steel substrates using an airless spray gun. The coating thickness was measured using a digital gauge (PosiTector 6000) with the appropriate gauge and calibration standards (MP 2527). Measurements were performed at a minimum of five points on the sample surface. The maximum operating temperature of the coating is 120 °C (dry heat).

Table 4-1: Composition of the phenolic epoxy coating.

Phenolic epoxy	Proportion
Bisphenol-A epoxy resin	10-30%
Benzyl alcohol	1-10%
Bisphenol-F epoxy resin	1-10%
Methylisobutyl ketone	1-10%
Xylene	1-10%
Ingredient determined to be non-hazardous or below reporting limits	Balance
Amine hardener	Proportion
Isophorone diamine	>60%

4.2.2 Exposure conditions

The coated panels were divided into two groups (six samples each) and exposed to dry heat in an oven (Binder GmbH, FDL 115, Germany). The isothermal group was dried at a constant temperature (120 °C), while for the cyclic group was subjected to thermal cycling (22 to 120 °C) following ISO 19277:2018 (dry thermal cycling) [7]. The thermal cycling process is illustrated in Figure 4-1

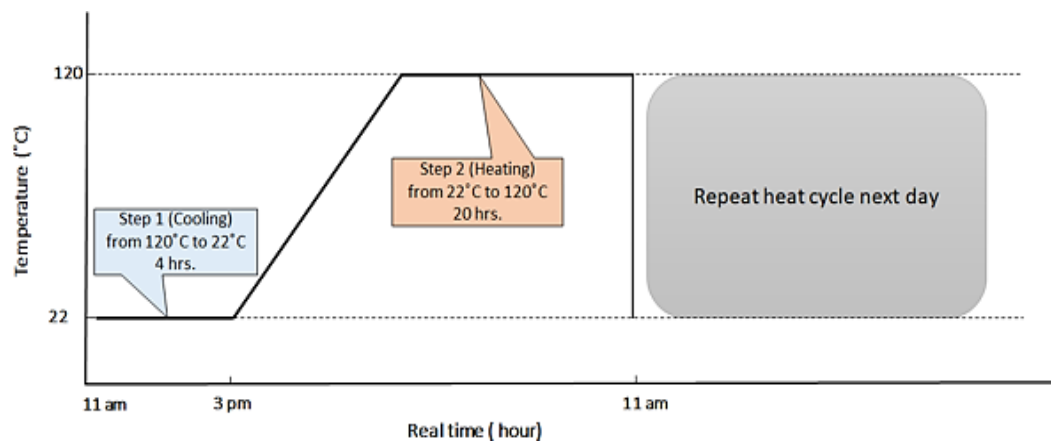


Figure 4-1: Dry thermal cycling profile (temperature vs time).

The samples for thermal cycling were removed from the oven, cooled at room temperature for 4 h and then placed into the oven again at 120 °C for 20 h. The isothermal and cycled samples were taken out of the furnace for examination after 20, 40, and 60 d. Additionally, one coated panel was exposed to 150 °C under isothermal conditions to accelerate the thermal degradation.

4.3 Characterisation techniques

4.3.1 Pull-off adhesion strength

During adhesion-strength testing, the force required to pull a specified test diameter of a coating away from its substrate using a hydraulic pump is measured. Adhesion tests were conducted using an automatic adhesion tester (PosiTest® AT-A), following ASTM D4541-02 [8]. The aluminium dolly was 14 mm in size. All dollies and the coating surface were abraded with 1200 grit SiC paper to enhance the mechanical anchoring with the adhesive. The dollies were cleaned with acetone to remove any contamination before they were affixed to the coating. The adhesion tests were performed 24 h after the dollies were affixed on the coated panels with epoxy adhesive (Resinlab EP11 HT). The measurements were conducted in triplicate. Before attaching the dolly to the coating surface, the coating around the dolly was cut using a hole saw and removed. Equation (4-1) was used to calculate the percentage change in the adhesion strength of the coating, which compares the strengths before (pre-exposure) and after (post-exposure) the sample was exposed to dry heating.

$$\text{Adhesion strength change (\%)} = \frac{\text{post exposure}^* - \text{pre exposure}}{\text{post exposure}} \times 100 \quad (4-1)$$

* The pre-exposure adhesion strength was 11.6 ± 1.1 MPa.

4.3.2 EIS

The performance of the coating before and after thermal exposure was evaluated using EIS. A glass tube with an exposed area of 14.6 cm² and 8 cm height was placed on the coated panel and tightly sealed with a mechanical clamp, as shown in Figure 4-2. The electrolyte was 3.5 wt% NaCl solution at 24 ± 1 °C and the total volume of electrolyte in the glass cell was 100 mL. A conventional three- electrode cell was used, consisting of an ionode probe filled with 3 M of KCl electrolyte as a reference electrode (with its tip placed 1–3 mm from the coating surface), a platinum mesh as a counter electrode, and the coated carbon steel as the

working electrode. EIS measurements were conducted using a Gamry potentiationstat (Interface 1010E™) at the OCP. A 20 mV (r.m.s) sinusoidal perturbation was applied in the frequency range of 100 KHz to 10 mHz, and six points per decade were measured. The EIS curves were analysed using Gamry Echem Analyst™ software.

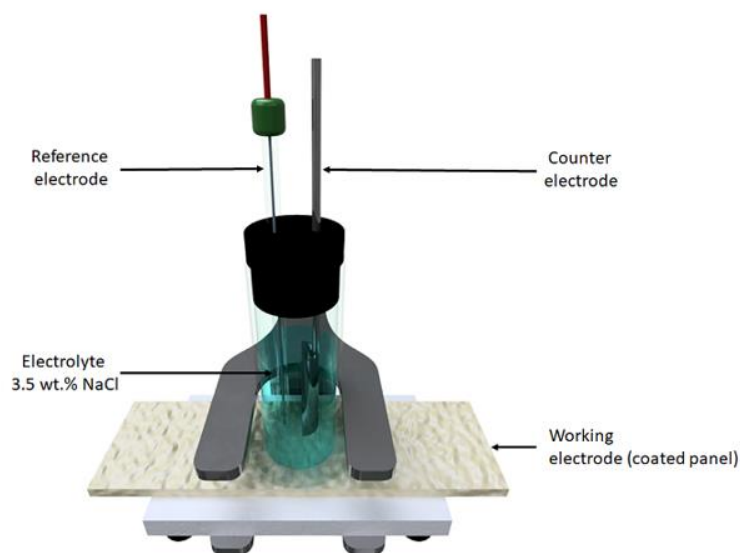


Figure 4-2: Schematic of the electrochemical cell used for testing the epoxy-coated metal sheets.

4.3.3 Thermal analysis

A Mettler Toledo AG (Switzerland) system was used for both TGA and DSC. The measurements were conducted in the temperature range of 35–800 °C at the heating rate of 10 °C min⁻¹ under an air flow (0.01 L min⁻¹). First, 5 mg samples scraped from the top layer of the coating surface were placed in a 40 µL platinum open pan. For TGA analysis, the sample weight as a function of temperature was measured. At the end of each run, the experimental data were used to plot the percentage of undegraded sample (1-*D*) % as a function of temperature, where $D = (W_0 - W)/W_0$; W_0 and W are the masses of sample at the starting point and during scanning. The experiments were performed in duplicate to obtain weight loss data. The initial weight loss of the pre-exposed sample was related to water loss [9]. For DSC analysis, the heat flow of the samples was measured to evaluate the enthalpy and temperature of the observed phase transitions.

4.3.4 FTIR

FTIR was used to determine the chemical changes in the polymer chains and the behaviours of all bands that are generated in hydrocarbon chains as a result of thermal exposure. A Nicolet iS50 was used to obtain the FTIR spectra, which is fitted with a dedicated

single-bounce diamond ATR purged with dry nitrogen. Specimens were obtained by scraping several milligrams of material from the surface of the coating, which was then finely ground in an agate mortar. All samples were measured using 64-scan data accumulation over the range of 500–4000 cm^{-1} at a spectral resolution of 4 cm^{-1} .

4.3.5 ToF-SIMS

ToF-SIMS analyses were performed using an IONTOF M6 ToF-SIMS system operated with a Bi_3^+ primary ion source (30 keV) and an electron flood source for charge compensation. The pulsed primary ion beam current was 1.1 pA and the primary ion dose density was below the static SIMS limit of 10^{13} ions cm^{-2} . Positive ion mass spectra were acquired from $100 \mu\text{m} \times 100 \mu\text{m}$ areas with a cycle time of 100 μs . The spectroscopy analytical mode was used, resulting in a mass resolution above 7500 at $m/z=29$. SurfaceLab software (IONTOF GmbH, Germany; version 7.2) with integrated multivariate statistical analysis was used to analyse the data. Principle component analysis was used to identify variations between spectra obtained from different samples.

Three coated panels were subjected to ToF-SIMS analysis, namely, a fresh sample used as a control, the sample exposed to 150 °C, and a selected sample after thermal exposure to cycling at 22 to 120 °C. Cross-sectional samples were prepared using a sandwich method (Figure 4-3) to minimise edge effects, which are deleterious for ToF-SIMS. The surface was prepared for analysis by wet grinding using SiC paper up to 1200 grit and then rinsing with deionised water and ethanol, followed by air drying.

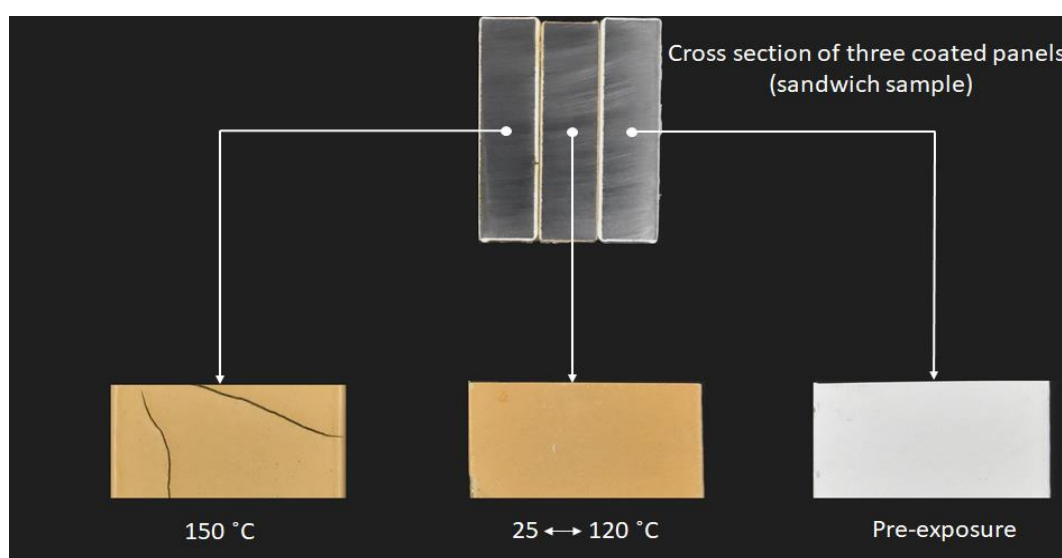


Figure 4-3: Arrangement of the three coated panels used for ToF-SIMS measurements.

4.4 Results and discussion

4.4.1 Pull-off adhesion strength

The pull-off strength measurements were conducted on the samples before and after 20, 40, and 60 days of exposure to isothermal or cyclic conditions (maximum temperature of 120 °C). Table 4-2 presents the adhesion strengths of the epoxy coatings as a function of time and dry heating condition. All tests were performed on duplicate coating panels with three measurements on each panel. As the exposure time increased from 0 to 60 d, the adhesion strength of all specimens increased. The highest value was ~24.9 MPa for the sample cycled for 40 d, corresponding to an increase of 53.4% compared to the initial condition. Moreover, the adhesion strength of the isothermal specimen after 40 d was high (20.2 MPa) with an increase of 42.6%. Furthermore, phenolic epoxy showed similar adhesion strengths (13.7–14.2 MPa) for all other exposure conditions and times. These results confirm that the adhesion properties of the organic coatings on the substrate improved for all samples after dry heat exposure. A previous study reported that the pull-off strength between the coating and metal substrate increases as the coating thickness decreases [10]. To confirm this, the coating thickness around the dolly was measured using a digital PosiTector 6000, which indicated that the distance from the dolly to the edge of the coated panel was 16.0 ± 1 mm. Figure 4-4 compares the pull-off strength with the coating thickness around the dolly for all coated panels. The thickness varied between 163 and 320 μm . No obvious correlation between the coating thickness and pull-off strength was observed for the various samples and most of the data points were under the fit line.

Table 4-2: Pull-off adhesion strengths for all tested samples.

Duration (day)	Adhesion strength (MPa) at constant temperature	Adhesion increase (%)	Adhesion strength (MPa) at cycling temperature	Adhesion increase (%)
20	13.7 ± 0.8	15.3	14.3 ± 1.6	18.9
40	20.2 ± 2.9	42.6	24.9 ± 3.6	53.4
60	14.2 ± 2.4	18.3	13.1 ± 2.2	11.5

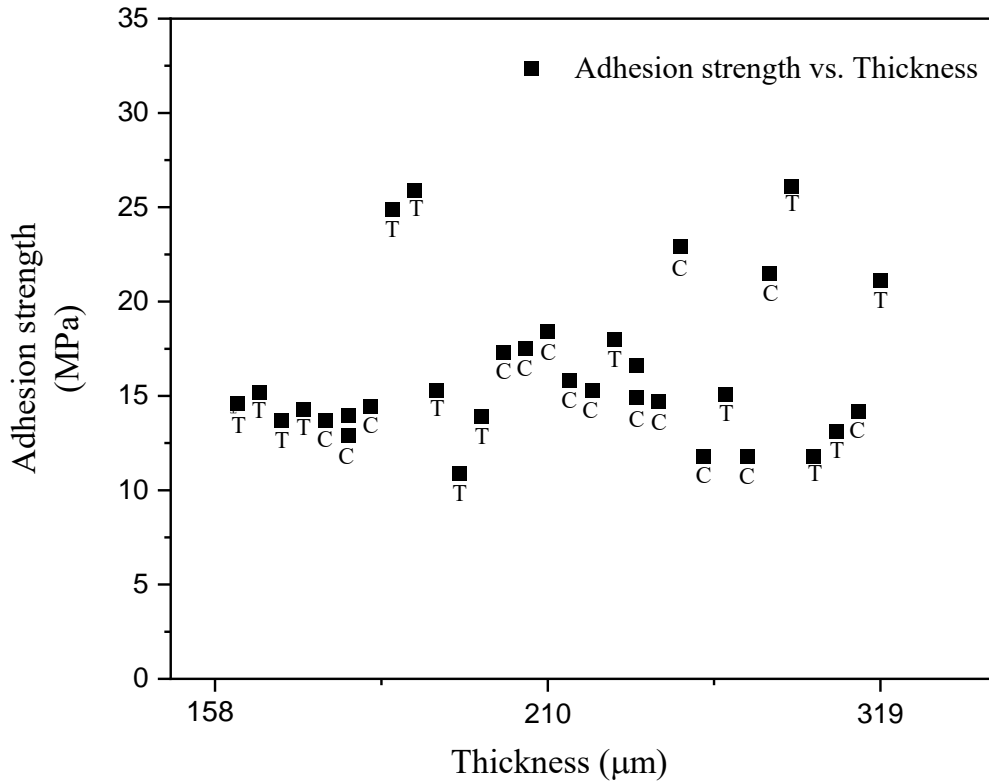


Figure 4-4: Pull-off adhesive strength as a function of the coating thickness for isothermal (C) and cycled (T) samples.

The area fractions of certain failure modes (cohesion, adhesion, and glue) of the detached adhesive surfaces after pull-off tests were calculated using ImageJ software [11]. Cohesion is defined as the internal strength of a coating resulting from the various interactions within the coating (single material), while adhesion refers to the bonding between the coating and metal substrate (two materials). Furthermore, a mixed failure mode describes the case when failure of cohesion and adhesion occurs simultaneously. In this case, the ratio between adhesive and cohesive areas can be determined. Additionally, failure can also occur in the adherent (i.e., the glue between the coating and dolly in these tests) if the coating adhesion is stronger than the adherent and the coating remains intact after test. Figure 4-5 shows the area fractions of the three failure modes (glue, cohesion, and adhesion) expressed as percentages. For the control sample (pre-exposure), adhesive failure is dominant. However, after thermal exposure, loss of cohesion is the major failure mode. As the pull-off adhesion tests measure the weakest bond among the coating/steel, coating, and coating/dolly, the results indicated that the bond strength between the coating/substrate increased after thermal exposure.

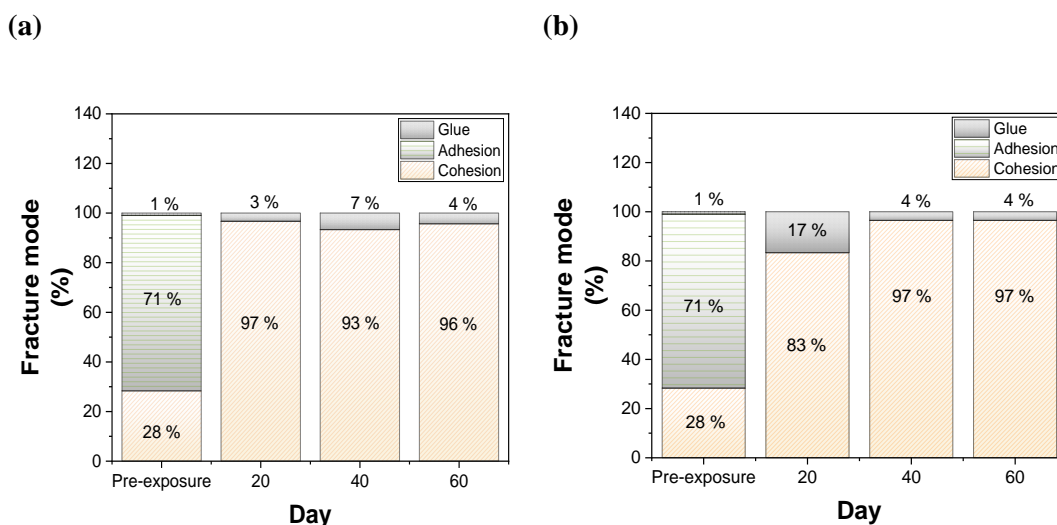


Figure 4-5: Area fractions of the failure modes of (a) isothermal and (b) cycled samples after pull-off adhesion tests.

In conclusion, it was found that the pull-off strength increased after thermal exposure and the failure mode changed from failure mainly at the metal/adhesive interface to failure mainly within the coating, indicating that the interfacial bond strength between the substrate and coating improved after heating. The water-induced weakening of the adhesive could induce a reduction in adhesive energy at the metal interface [12]. After the coating was exposed to heat, the moisture content within the coating system decreases, thereby driving a shift in the dominant failure mode from adhesion to cohesion.

4.4.2 Electrochemical properties

The Nyquist plots of the electrochemical impedance of the coated panels show three distinct features, representing three different mechanisms (Figure 4-6). The pre-exposure sample showed low resistance. The EIS plots show semi-circles as capacitive loops that differ at high frequency and an oblique line at low frequency. These findings imply that a corrosive medium diffused into the coating–metal interface. The plot for the 120 °C isothermal sample is characterised by a single semi-circle with high impedance, suggesting that water penetrated the coating but did not reach the coating–metal interface. In contrast, the plot for the 150 °C isothermal sample shows double capacitive loops, indicating that the coating delaminated from the substrate (Figure 4-3).

Figure 4-7 shows the evolution of Bode plots over time for the various thermal treatments. All coatings exhibited capacitive behaviour, with a single time constant covering a wide range of frequencies and a high impedance modulus at low frequency (indicating the

resistance of the system) between $10^8 \Omega \cdot \text{cm}^2$ for the pre-exposed samples and almost $10^{10} \Omega \cdot \text{cm}^2$ for the coated samples after thermal treatment. The higher impedance of the coating after thermal treatment implies that exposing the coated panels to 120°C forms a more durable barrier to the penetration of electrolytes. A simple equivalent circuit used for fitting the EIS data is shown in Figure 4-8a, comprising R_s , coating resistance R_{coat} , and CPE of the coating Q_{coat} . This circuit is commonly used for systems with a single time constant [13-14]. After 3 d of isothermal exposure to 150°C , large cracks appeared on the coating (as shown in Figure 4-3), which may have resulted in the corrosion of the metal surface under the cracks due to electrolyte penetration before EIS was conducted. To account for the coating degradation, the EIS curves for this sample were fit using the modified equivalent electrical circuit presented in Figure 4-8b [15]. The shape of the plots for a coated metal, with two minima for the phase plot. The one at high frequency reflects the physical behaviour of the coating (Q_{coat} , R_{coat}), while the one at intermediate frequencies corresponds to the corrosion reactions at the coating–substrate interface (Q_{dl} , R_{ct}). The low R_{coat} and R_{ct} values indicate a low resistance to electrolyte diffusion through the coating and a significant corrosion reaction at the interface, respectively. The reactive impedance is equal to the sum of R_{ct} and R_s , i.e., $2.51 \times 10^4 \Omega \cdot \text{cm}^2$.

The data in Table 4-3 and Table 4-4 summarise the resistance and capacitance values. The R_{coat} value increases from $10^8 \Omega \cdot \text{cm}^2$ for the pre-exposure sample to $10^{10} \Omega \cdot \text{cm}^2$ after thermal treatment. The maximum value of R_{coat} after 40 d of isothermal treatment was $3.18 \times 10^{10} \Omega \cdot \text{cm}^2$, while the highest equivalent value after thermal cycling was $3.38 \times 10^{10} \Omega \cdot \text{cm}^2$. Progressive improvement in the dielectric properties over time is also indicated by the Q_{coat} data. The Q_{coat} values for the coatings ($10^{-10} \text{F} \cdot \text{cm}^{-2}$) exposed to isothermal treatment at 120°C are much lower than that of the control ($10^{-9} \text{F} \cdot \text{cm}^{-2}$). In addition, the Q_{coat} and Q_{dl} values for the coating exposed to isothermal heating at 150°C for 3 d increased compared to the control, implying the diffusion of corrosive species through the coating and contact with the metal substrate (Table 4-5).

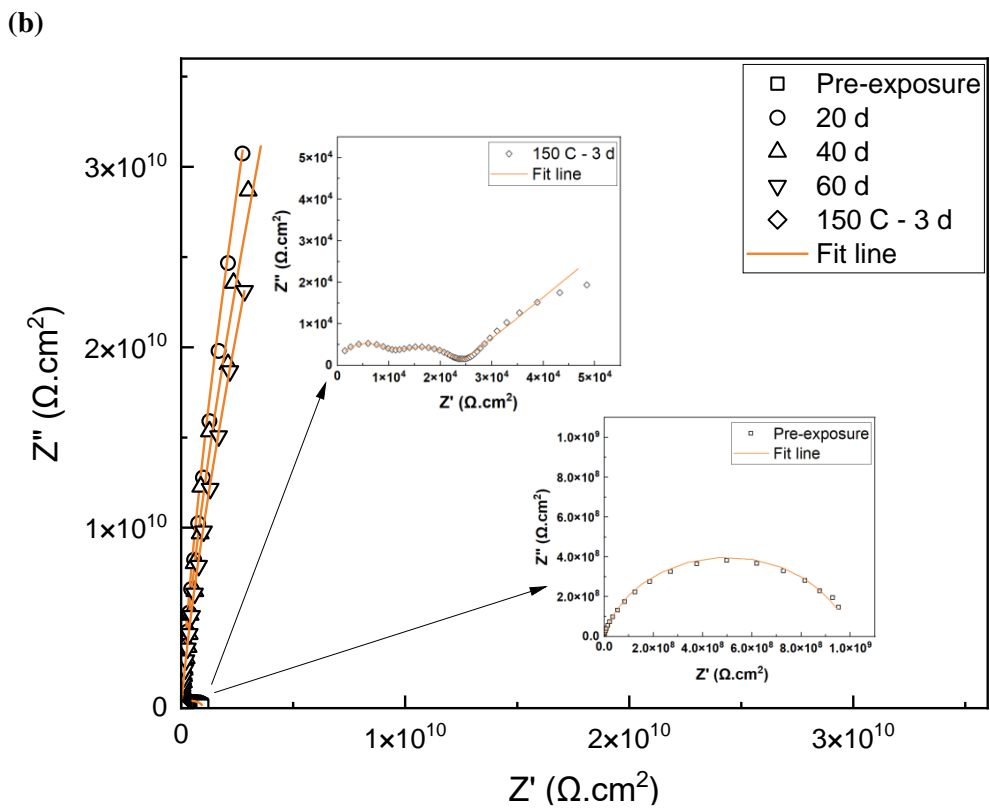
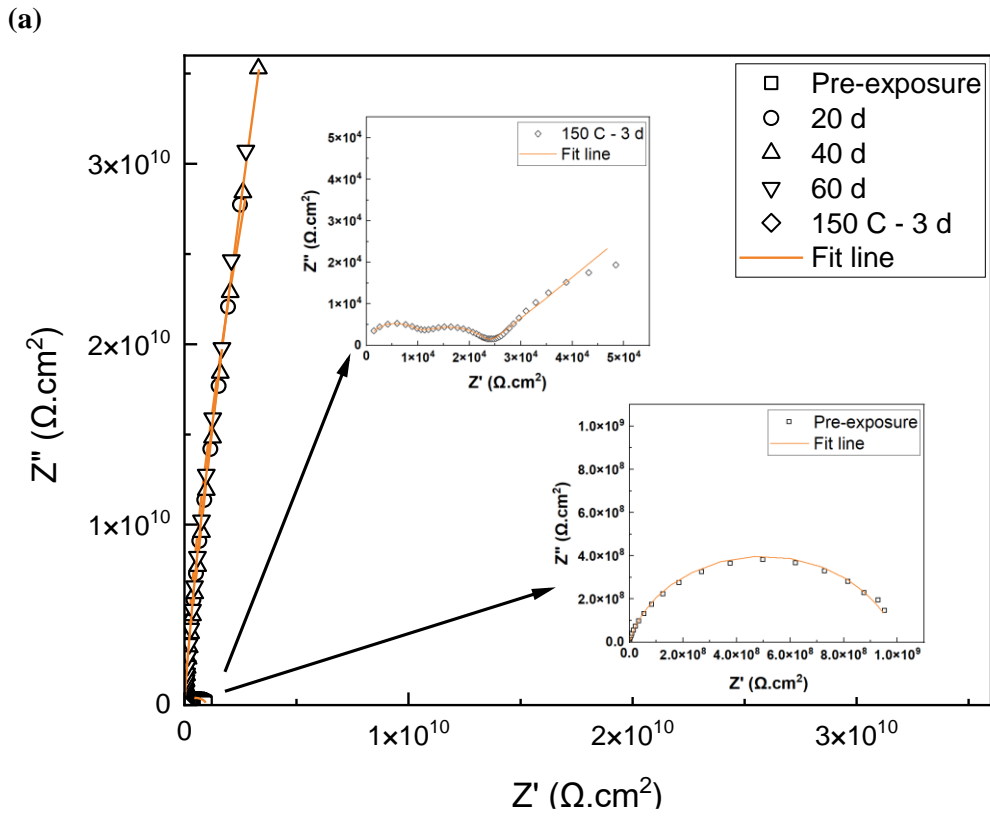
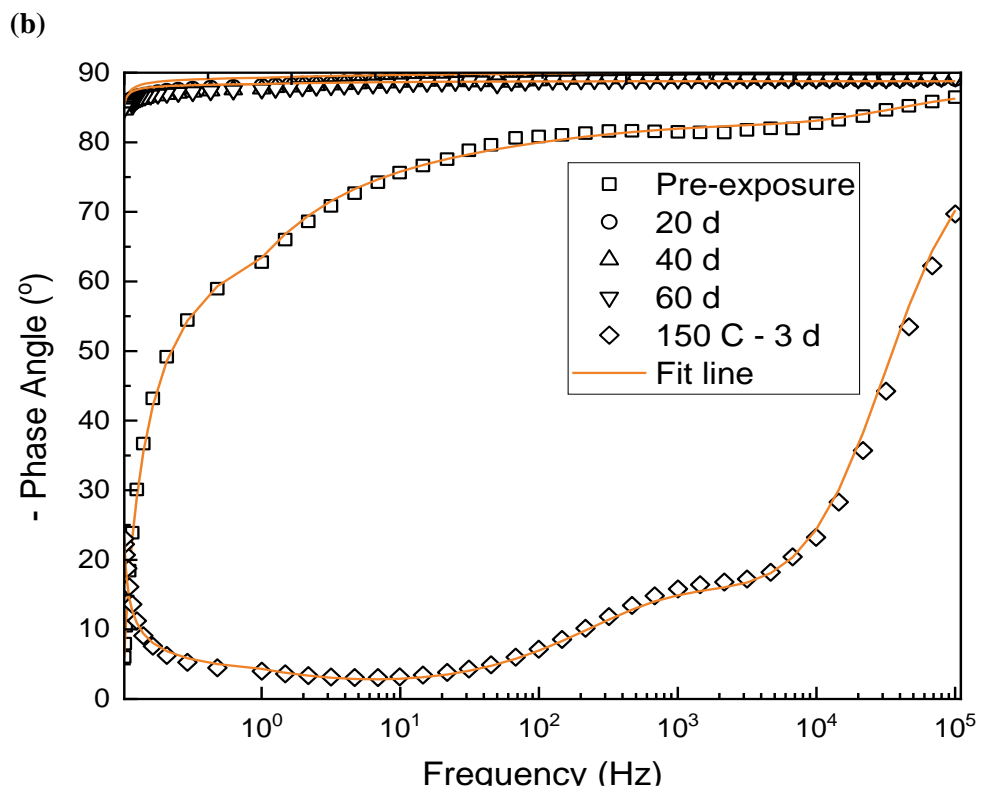
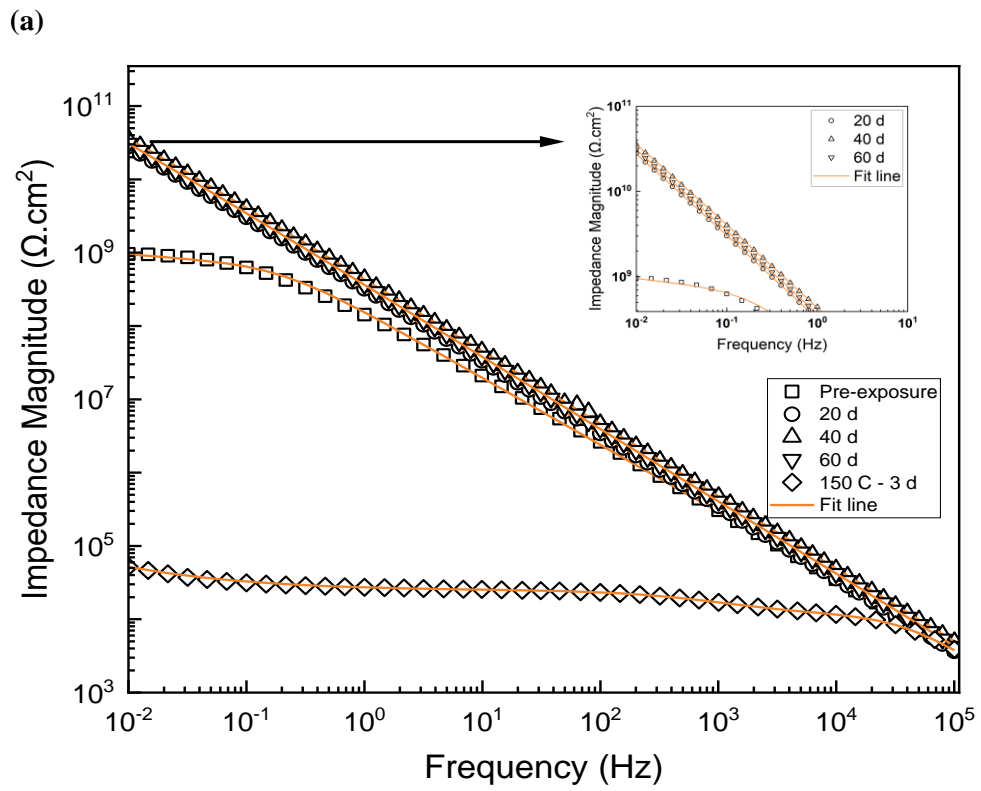


Figure 4-6: Nyquist plots of phenolic-epoxy-coated steel samples after immersion in 3.5 wt% NaCl solution: (a) cycled and (b) isothermal heat treatment (120 °C maximum temperature).



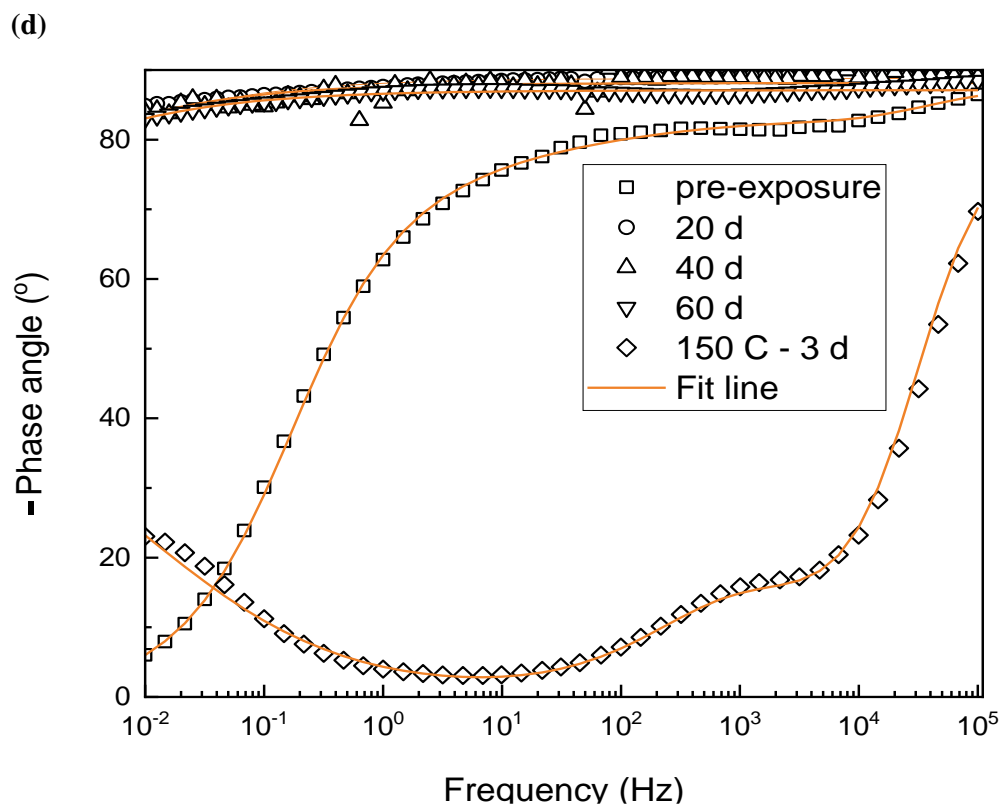
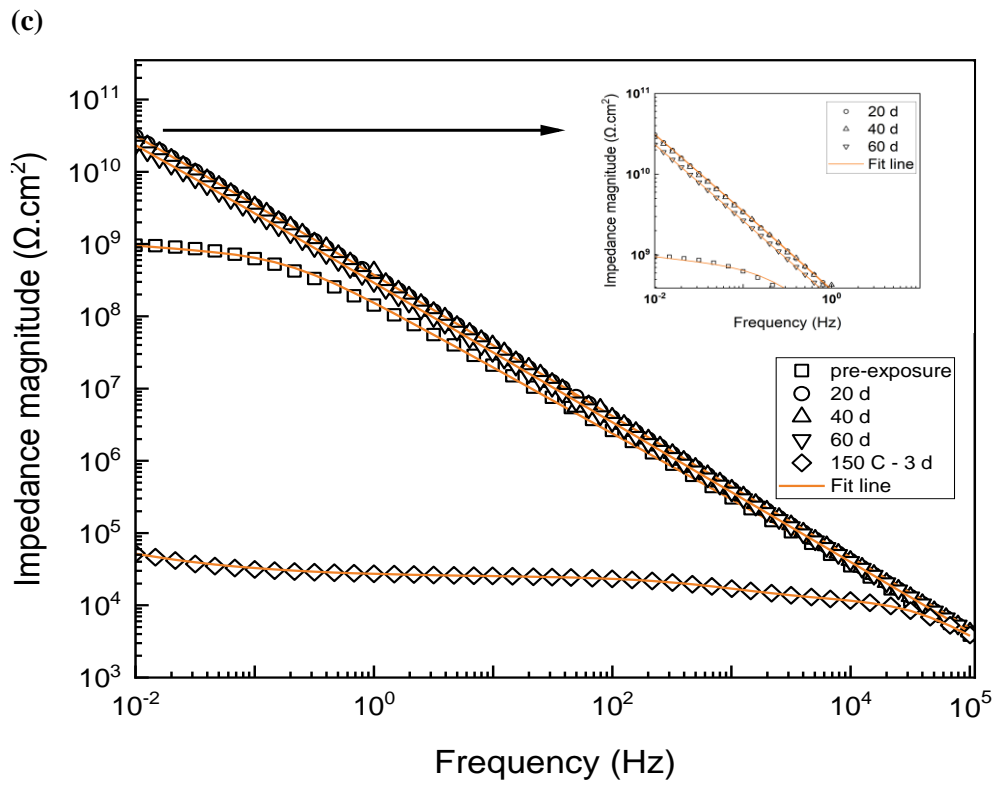
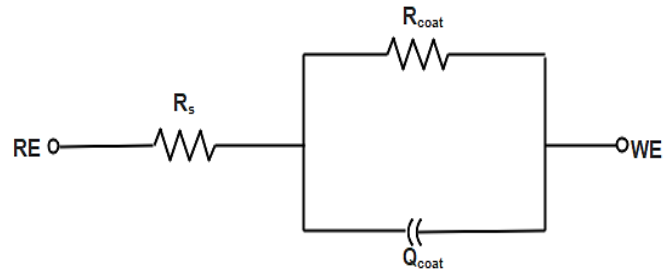


Figure 4-7: Bode plots of phenolic-epoxy-coated steel samples after immersion in 3.5 wt% NaCl solution: (a-b) cycled and (c-b) isothermal heat treatment (120 °C maximum temperature).

(a)



(b)

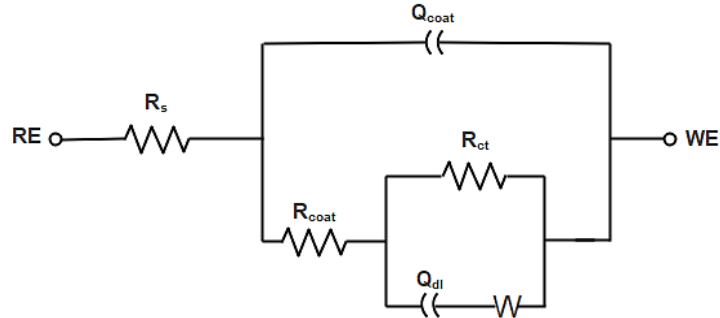


Figure 4-8: Equivalent circuits used to fit the impedance curves obtained for (a) all coated metal samples other than (b) the 150 °C isothermal sample (to account for cracks in the coating).

Table 4-3: EIS fitting parameters for the 120 °C isothermal samples

<i>Duration</i> (day)	R_{coat} ($\Omega \cdot \text{cm}^2$)	Q_{coat} ($F \cdot \text{s}^{\alpha-1} \cdot \text{cm}^{-2}$)	n_{coat}	X^2
Pre-exposure	8.12×10^8	1.8×10^{-9}	0.84	5.55×10^{-3}
20 d	1.03×10^{10}	3.90×10^{-10}	0.965	8.05×10^{-4}
40 d	3.18×10^{10}	5.23×10^{-10}	0.994	3.63×10^{-3}
60 d	1.48×10^{10}	4.66×10^{-10}	0.977	1.46×10^{-4}

Table 4-4: EIS fitting parameters for the 120 °C cycled samples

<i>Duration</i> (day)	R_{coat} ($\Omega \cdot \text{cm}^2$)	Q_{coat} ($F \cdot \text{s}^{\alpha-1} \cdot \text{cm}^{-2}$)	n_{coat}	X^2
Pre-exposure	8.12×10^8	1.8×10^{-9}	0.84	5.55×10^{-3}
20 d	2.36×10^{10}	4.36×10^{-10}	0.991	1.46×10^{-4}
40 d	3.38×10^{10}	5.73×10^{-10}	0.998	9.48×10^{-4}
60 d	3.29×10^{10}	5.03×10^{-10}	0.968	1.51×10^{-4}

Table 4-5: EIS fitting parameters for the 150 °C isothermal samples after 3 d of exposure.

R_{coat} ($\Omega \cdot \text{cm}^2$)	R_{ct} ($\Omega \cdot \text{cm}^2$)	Q_{coat} ($F \cdot s^{\alpha-1} \cdot \text{cm}^{-2}$)	n_{coat}	Q_{dl} ($F \cdot s^{\alpha-1} \cdot \text{cm}^{-2}$)	N_{dl}	X^2
1.1×10^{-4}	1.35×10^{-4}	4.62×10^{-4}	0.98	2.14×10^{-7}	0.71	2.37×10^{-4}

4.4.3 Thermal behaviour

TGA and differential TGA (DTGA) results are shown in Figure 4-9. The major reactions are the dehydration of the coating with the formation of a double bond in the polymer chain, double bond isomerisation, and allyl-oxygen bond scission [16]. The DTGA curves in Figure 4-9b and Figure 4-9d show a single endothermic peak at the same temperature region, close to 350 °C, for all coated panels. After heat treatment, two endothermic peaks are observed at 121 and 348 °C. This is due to the different temperature ranges of reactions of this sample. The peak at 121 °C could be due to the phase separation of the epoxy mixture during dehydration [17]. The second peak of the pre-exposure phenolic epoxy (at 348 °C) is considered the highest endothermic peak of all samples. This indicates that material decomposition accelerates at 348 °C [18]. Thermal damage during heating leads to a considerable loss of compounds, which in turn causes rapid degradation of the coating [17]. Subsequently, all coated panels show low endothermic peaks because of the formation of highly cross-linked structures and reduced reaction rates related to diminished chain mobility, which minimises the decomposition of compounds in the coating [17].

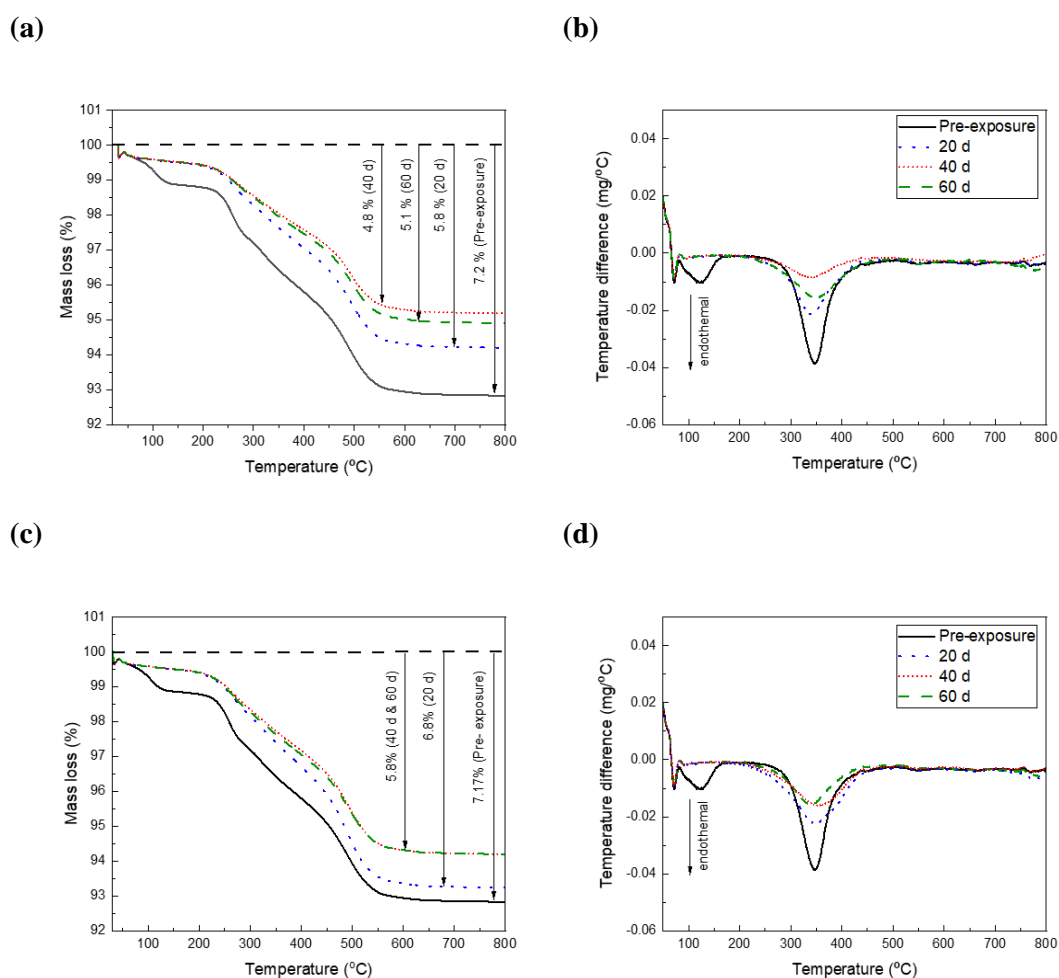


Figure 4-9: (a, c) TGA and (b, d) DTGA curves measured in air for phenolic-epoxy heat treated to a maximum of 120 °C under (a, b) isothermal or (c, d) cyclic conditions.

The T_g is an important parameter for identifying changes in the physical properties of polymers in their transition from a rigid glassy state to a softer rubbery state. The DSC curves used to determine the T_g values of the coated samples are shown in Figure 4-10. The lower T_g indicates the easier movement of molecules due to a less dense epoxy cross-linked network (lower MW) [19]. The T_g values of the phenolic-epoxy coating increased after different periods of exposure to 120 °C. The initial T_g of 43.5 °C increased to 49.35 ± 1 °C after thermal cycling and 49.55 ± 1 °C after isothermal treatment for different durations. This emphasises that epoxy molecules have a high molecular chain strength and high MW after exposure to heating at 120 °C [19]. The pre-exposure coating shows two heat-flow peaks, corresponding to a melting process and the presence of organic solvents. Low-MW solvents have a large effect on the results of DSC purity determinations. The volatile impurities of substances with melting points above approximately 80 °C can evaporate [20].

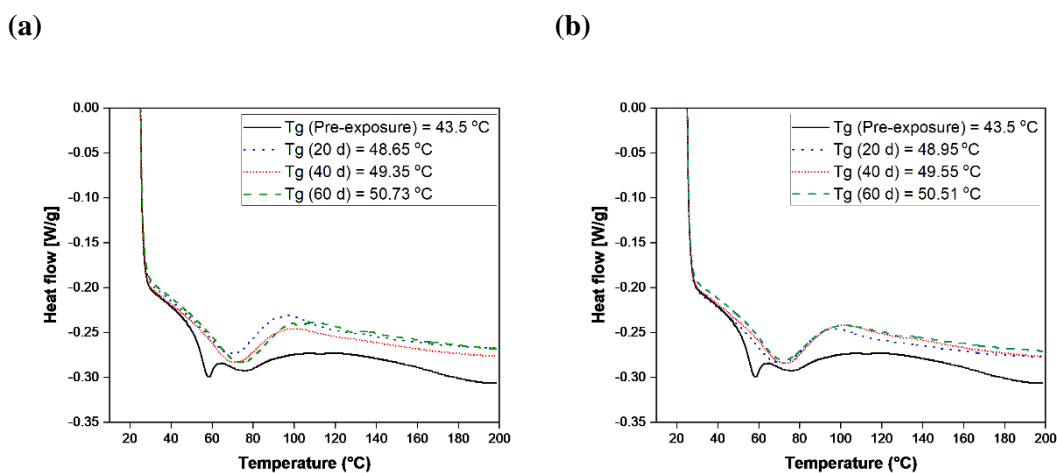


Figure 4-10: DSC curves used to determine the Tg values of phenolic epoxy coatings heat treated to a maximum of 120 °C under (a, b) isothermal or (c, d) cyclic conditions.

4.4.4 Chemical properties

The FTIR spectra of the phenolic epoxy coatings exposed to different thermal conditions are shown in Figure 4-11. The absorption bands at 1650 and 1725 cm^{-1} increased with increasing exposure time, which could be due to the effect of the high temperature on the fresh coating, i.e., the formation of carbonyl groups [23]. In the hydroxyl domain ($\sim 3800\text{--}2500\text{ cm}^{-1}$) [24], only minor changes were observed after 40 d of heat treatment. The C=C stretching vibration is normally observed at 1665–1675 cm^{-1} for the trans configuration and at 1635–1665 cm^{-1} for the cis configuration [24]. Consequently, the prominent band at 1730 cm^{-1} is assigned to the characteristic C=O stretching frequency [25].

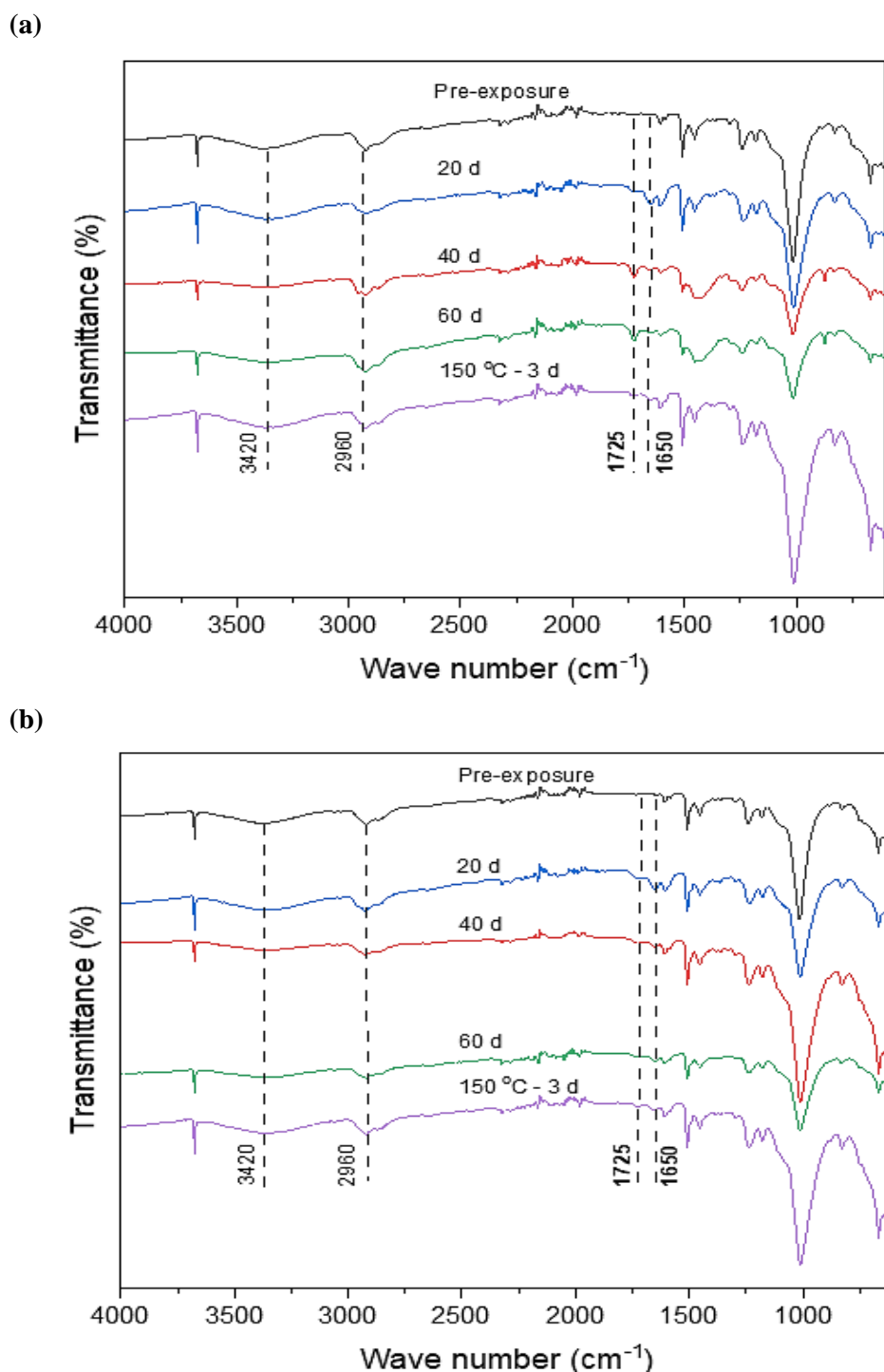


Figure 4-11: FTIR spectra phenolic epoxy coatings before and after heat treatment to a maximum of 120 °C under (a) cyclic or (b) isothermal.

The molecular-level changes in the structure that can occur in the phenolic epoxy-coating during thermal treatment are illustrated below. A representative molecular structure of epoxy resins (diglycidyl ether of bisphenol A; DGEBA) is shown in Figure 4-12 To interpret the thermal behaviour of the epoxy resin, the simplest DGEBA resin with $n = 0$ is

considered. Moreover, the curing of epoxy resin systems is strongly dependent on the type of hardener. To explain the structure of the heat-treated resins as simply as possible, an aliphatic amine curing agent, ethylene diamine (EDA), is considered. A stoichiometric mixture contains two molecules of EDA bonded with two molecules of DGEBA. The structure of the resultant product is shown in Figure 4-13a. The carbonyl group formed in an epoxy resin is surrounded by adjacent $-\text{CH}_2-$ groups. The bands at 1725 cm^{-1} are assigned to the characteristic $\text{C}=\text{O}$ stretch frequency, which is expected to result in absorption in the region for alkyl-substituted carbonyls [23]. The presence of double bonds in the amine linkages is indicated by the $\text{C}=\text{C}$ stretching vibration. These peaks at 1650 cm^{-1} are the result of shifting alkane frequencies arising from adjacent amine groups [24]. The changes in the structure of the carbonyl groups form pendant $-\text{OH}$ groups, and double bonds form in the amine linkages of the epoxy resin. Reactions involving the evolved hydrogen, such as the formation of carbonyl groups and double bonds in the amine linkage, and possibly cross-linking between molecules, are shown in Figure 4-13b. These reactions tend to make the molecular network more rigid, thus affecting the mechanical properties as shown in Table 4-2 and Figure 4-5.

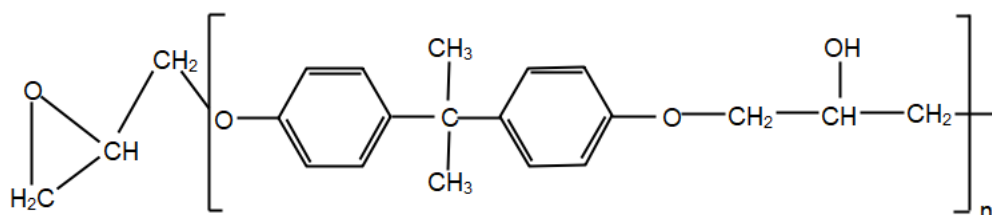
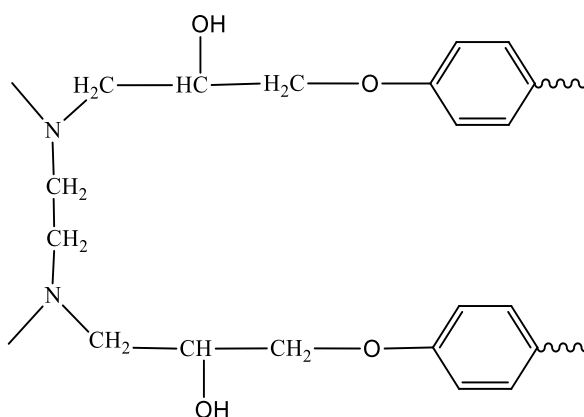


Figure 4-12: Chemical structure of DGEBA as a typical resin.

(a)



(b)

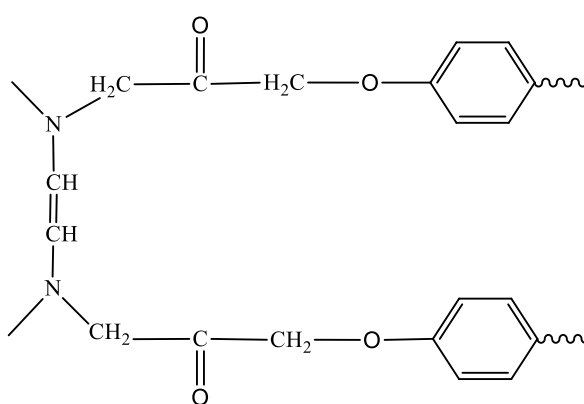


Figure 4-13: Chemical structures produced during the resin curing reaction between DGEBA and EDA hardener (a) before and (b) after heat exposure [24].

4.4.5 Molecular structure of the coatings

The molecular composition of the coatings was studied by ToF-SIMS. Figure 4-14 shows a variation in the intensity of the secondary ion peaks of positive ions for the coatings used in this study (exposed to three different thermal treatment conditions). The assignments of the peaks were initially based on reference libraries and the literature for DGEBA [24-27]. The $C_xH_yO^+$ ions were identified as the single-ring ions in the resin, the nitrogen-containing hydrocarbon ions ($C_xH_yN^+$) are related to the epoxy hardener, while the aliphatic hydrocarbon ions (C_xH^+) indicate structural density [26]. The MW of the hydrocarbon ions provides significant information about the cross-linking to the hydrocarbon structure in the phenolic epoxy coatings. The ToF-SIMS analysis focused on the sample with the highest adhesion strength, which was subjected to thermal cycling between 22 °C and 120 °C for 40 d. Cracks were present on the coating of the similar sample cycled to 150 °C. To investigate the differences between these samples, ToF-SIMS was used to investigate the molecular composition of the coating to identify the changes in the epoxy structure at high temperatures.

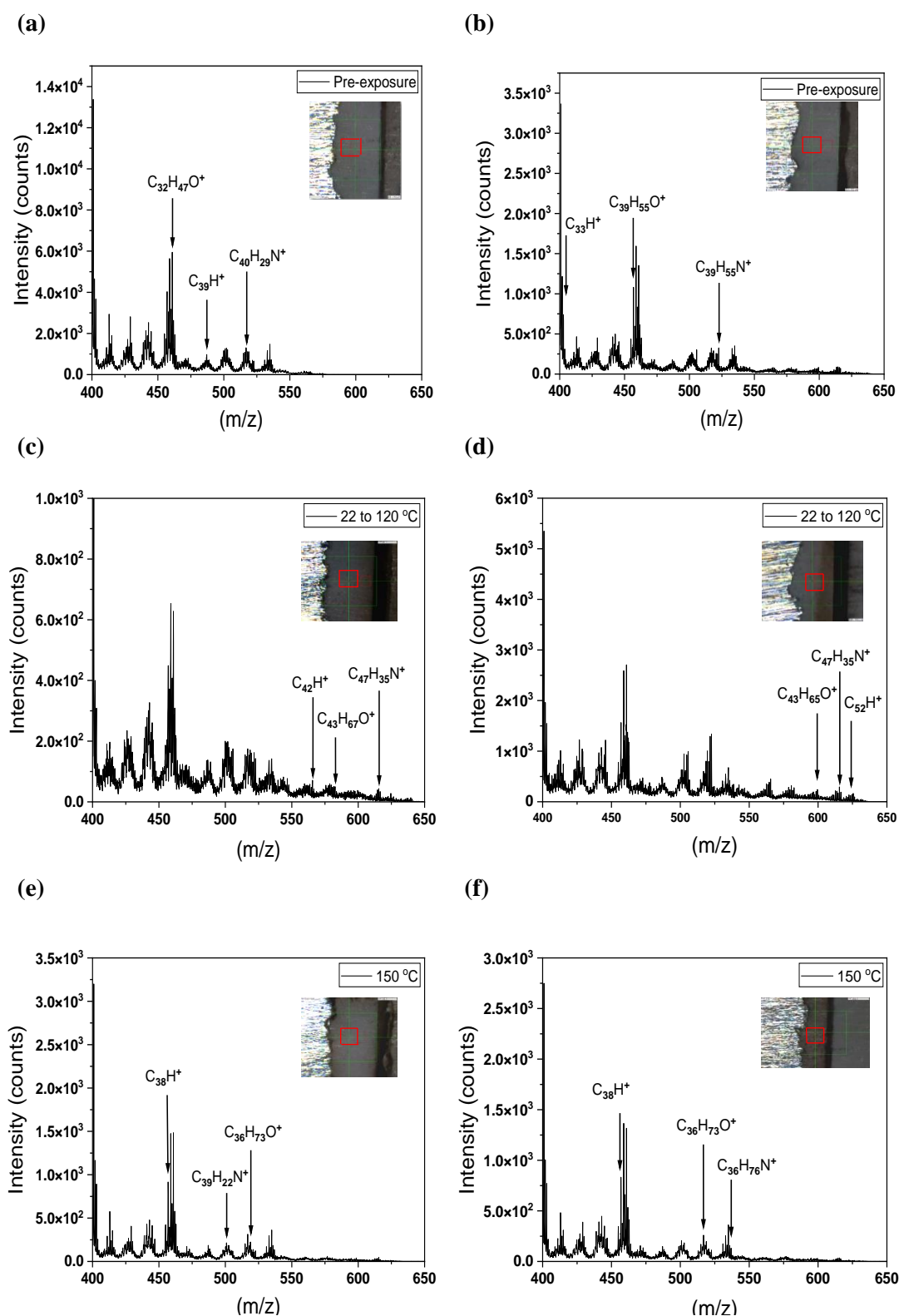


Figure 4-14: Positive ion ToF-SIMS spectra (field of view $0.1 \text{ mm} \times 0.1 \text{ mm}$, indicated in the inset optical microscopy images of cross-sections of single-layer coatings). The highest MW ions ($\text{C}_x\text{H}_y\text{O}^+$, $\text{C}_x\text{H}_y\text{N}^+$, and C_xH^+) with intensities above 10 counts are labelled. (a,b) Pre-exposure, (c,d) cyclic treatment up to $120 \text{ }^\circ\text{C}$ for 40 d, and (e,f) isothermal treatment at $150 \text{ }^\circ\text{C}$ for 3 d.

Measurements were taken at two locations for each coating, as indicated by the red squares in the inset microscopy images in Figure 4-14. The mass range of 400–640 m/z shows contributions from three high-MW components. The highest aliphatic hydrocarbon weight was identified for $C_{33}H^+$, $C_{39}H^+$, $C_{42}H^+$, $C_{52}H^+$, and $C_{38}H^+$ for all three thermal conditions. The results for the unexposed control sample were compared with those for the heat-treated samples (thermal cycling to 120 °C or isothermal treatment at 150 °C). The cycled sample had the highest MW and the aliphatic hydrocarbon was $C_{52}H^+$, which indicates enhanced cross-linking between the epoxy resin and curing agent (hardener) during thermal exposure [27]. At the higher temperature of 150 °C, epoxy chain scission occurred, resulting in a reduction in C–C bonding. A reduction in aliphatic hydrocarbon indicates a network rupture and a reduction in network density, which is due to the low MW aliphatic hydrocarbon $C_{38}H^+$. Other explanations might be a heat-induced condensation reaction or the formation of polyaromatic structures at the surface [26-27].

The other significant polymer group is resin molecules, which is indicated by the oxygen-containing hydrocarbon molecules revealed by the ToF-SIMS positive ion spectra (Figure 4-14). $C_{32}H_{47}O^+$, $C_{39}H_{55}O^+$, $C_{43}H_{67}O^+$, $C_{43}H_{65}O^+$, $C_{32}H_{60}O^+$, and $C_{36}H_{73}O^+$ were observed for the resin material. No differences attributable to the network density were observed in the spectra of the sample treated at 150 °C and the unexposed control sample. The increased development of hydrocarbon molecules during thermal cycling increased the MW of the resin material to $C_{43}H_{67}O^+$. This indicates that the cross-linking of the resin enhanced the oligomer bonds and distributions in the resin. This chain length provides better-balanced mechanical and thermal properties [24].

Another contribution appears in the $C_xH_yN^+$ ion fragments, such as $C_{40}H_{29}N^+$, $C_{39}H_{29}N^+$, $C_{47}H_{35}N^+$, $C_{39}H_{22}N^+$, and $C_{36}H_{76}N^+$. Figure 4-14 show significant changes in long-chain hydrocarbon ions that contain nitrogen. The structural density and cross-linking reactions in the hardener component increased when the coating was exposed to thermal cycling for 40 days, reaching $C_{47}H_{35}N^+$. This indicates a discrete physical phenomenon in which the concentrations of ions produced during thermal cycling increase in the hardener and resin. The structural changes at the interfaces of adhesive joints provide valuable information regarding the adhesive/coating surface and interfaces (adhesion chemistry).

In the case of the sample treated at 150 °C, the hydrocarbon ions containing nitrogen ($C_{40}H_{29}N^+$ to $C_{36}H_{76}N^+$) had lower MW than those identified for the control sample. The hardener component suffered chain scission as a result of thermomechanical stresses, resulting in structural damage [27]. Thermal stress generates mechanical pressure at the surface and in the bulk resulting in crack initiation and propagation. Organics coatings can be damaged at

elevated temperatures due to the outgassing of volatiles, dehydration, and shrinkage, where the latter results in the generation of cracks [25].

The ToF-SIMS results provide insight about the possible changes in chemistry of the coating. The results indicated that the molecular composition of the sample changed after heating, observed as changes in the intensities of ions reported to be related to the chain structure of epoxy components, which are consistent with the mechanical testing results.

4.5 Conclusions

This study investigated the chemical and physical changes of phenolic–epoxy coatings after exposure to elevated temperatures. The following conclusions were drawn.

- Phenolic-epoxy coatings underwent post-curing when exposed to 120 °C for up to 40 d, resulting in enhanced coating performance, as demonstrated by the increased adhesion strengths and high impedance of the coatings.
- After further exposure for 60 d, the opposite results were obtained; i.e., coating degradation was evidenced by lower adhesion strengths.
- The ToF-SIMS results demonstrated enhanced cross-linking after thermal exposure due to the generation of larger hydrocarbon fragments.

4.6 References

- [1] G. P. Bierwagen, "Reflections on corrosion control by organic coatings," *Prog. Org. Coatings*, vol. 28, no. 1, p. 5, 1996.
- [2] S. G. Croll, "Stress and embrittlement in organic coatings during general weathering exposure: A review," *Progress in Organic Coatings*. 2022.
- [3] N. H. Tennent, "Clear and pigmented epoxy resins for stained glass conservation: Light ageing studies," *Stud. Conserv.*, 1979.
- [4] D. Fast, "a two step solution to the high cost of corrosion under insulation," *corrosionpedia*, vol. 1, 2020.
- [5] M. Ogata, N. Kinjo, and T. Kawata, "Effects of crosslinking on physical properties of phenol-formaldehyde novolac cured epoxy resins," *J. Appl. Polym. Sci.*, 1993.
- [6] J. M. Charlesworth, "Effect of crosslink density on the molecular relaxations in diepoxide-diamine network polymers. Part 1. The glassy region," *Polym. Eng. Sci.*, 1988.
- [7] "INTERNATIONAL STANDARD Petroleum , petrochemical and natural gas," vol. 2012, p. 12, 2018.
- [8] ASTM, "D4541-09: Standard Test Method for Pull-Off Strength of Coatings Using Portable Adhesion," *ASTM Int.*, 2014.
- [9] R. B. Prime, H. E. Bair, S. Vyazovkin, P. K. Gallagher, and A. Riga, "Thermogravimetric Analysis (TGA)," in *Thermal Analysis of Polymers: Fundamentals and Applications*, 2008.
- [10] R. Singh, S. Schrufer, S. Wilson, J. Gibmeier, and R. Vassen, "Influence of coating thickness on residual stress and adhesion-strength of cold-sprayed Inconel 718 coatings," *Surf. Coatings Technol.*, 2018.
- [11] S. Kambhampati and T. Pojtanabuntoeng, "a systemic study on the effects of key influencing factors on pull-off adhesion test of organic coatings," *Corros. Sci. engineering*, vol. 1, p. 11, 2023.
- [12] X. Li, S. Deng, and H. Fu, "Blue tetrazolium as a novel corrosion inhibitor for cold rolled steel in hydrochloric acid solution," *Corros. Sci.*, 2010.
- [13] M. Mahdavian and S. Ashhari, "Mercapto functional azole compounds as organic corrosion inhibitors in a polyester-melamine coating," *Prog. Org. Coatings*, 2010.

- [14] R. C. M. K. R.D. Granata, "Polymer coating degradation mechanisms related to hot production. In HOUSTON TX: Defense Technical Information Center." p. 551, 1993.
- [15] J. M. Morancho, J. M. Salla, X. Ramis, and A. Cadenato, "Comparative study of the degradation kinetics of three powder thermoset coatings," *Thermochim. Acta*, 2004.
- [16] D. Puglia, L. B. Manfredi, A. Vazquez, and J. M. Kenny, "Thermal degradation and fire resistance of epoxy-amine-phenolic blends," *Polym. Degrad. Stab.*, 2001.
- [17] B. K. Kandola, B. Biswas, D. Price, and A. R. Horrocks, "Studies on the effect of different levels of toughener and flame retardants on thermal stability of epoxy resin," *Polym. Degrad. Stab.*, 2010.
- [18] R. Sarathi, R. K. Sahu, and P. Rajeshkumar, "Understanding the thermal, mechanical and electrical properties of epoxy nanocomposites," *Mater. Sci. Eng. A*, 2007.
- [19] A. Zaccone and E. M. Terentjev, "Disorder-assisted melting and the glass transition in amorphous solids," *Phys. Rev. Lett.*, 2013.
- [20] MettlerToledo, "DSC purity determination," *METTLER TOLEDO Therm. Anal. Syst.*, 2000.
- [21] A. E. Krauklis and A. T. Echtermeyer, "Mechanism of yellowing: Carbonyl formation during hygrothermal aging in a common amine epoxy," *Polymers (Basel)*, 2018.
- [22] S. G. Burnay, "Radiation-induced changes in the structure of an epoxy resin," *Radiat. Phys. Chem.*, 1980.
- [23] A.J.B., "IR - theory and practice of infrared spectroscopy," *J. Mol. Struct.*, 1974.
- [24] J. A. Treverton, A. J. Paul, and J. C. Vickerman, "Characterization of adhesive and coating constituents by time-of-flight secondary ion mass spectrometry (ToF-SIMS). Part 1: Epoxy-terminated diglycidyl polyethers of bisphenol-A and propal-2-ol," *Surf. Interface Anal.*, 1993.
- [25] J. Decelle, N. Huet, and V. Bellenger, "Oxidation induced shrinkage for thermally aged epoxy networks," *Polym. Degrad. Stab.*, 2003.
- [26] F. Awaja, G. Van Riessen, G. Kelly, B. Fox, and P. J. Pigram, "ToF-sims investigation of epoxy resin curing reaction at different resin to hardener ratios," *J. Appl. Polym. Sci.*, 2008.
- [27] F. Awaja and P. J. Pigram, "Surface molecular characterisation of different epoxy resin composites subjected to UV accelerated degradation using XPS and ToF-SIMS," *Polym. Degrad. Stab.*, 2009.

CHAPTER 5

S. Ahmed, K. Lepkova, T. Becker, T. Pojtanabuntoeng, The Performance of Phenolic Epoxy Coating after Thermal Exposure for Corrosion Protection in Marine Environments, paper no.C2023-19046, AMPP Annual conference + Expo, 2023. The conference paper covered NaCl concentration's influence on the performance of the phenolic epoxy coating.

This chapter presents the published paper with modified formats and contents that match the overall style of the thesis.

Influences of NaCl and pH on a Phenolic Epoxy Coating

Abstract

The behaviour of a commercial phenolic epoxy coating on carbon steel panels was examined after exposure to thermal cycling (22 to 120 °C for 40 d). Two groups of samples (before and after thermal treatment) were immersed in solutions with 3.5 or 5 wt. % NaCl or exposed to water condensation at 80 °C for 60 d, which had pH of 7.3 (without further adjusting). The effect of pH was evaluated at pH 4 and 8 in 3.5 wt% NaCl solution. All tests were conducted for 60 days. In each experiment, samples consisted of both scribed and un-scribed panels. The coated panels were assessed with electrochemical impedance spectroscopy at the end of the experiment.

The EIS results, and the degree of blistering and delamination around the scribed regions of the panels suggested that 3.5 wt. % NaCl caused greater degradation than did 5 wt. % NaCl. The coating degradation was more prominent at pH 8 compared to pH 4.

The thermal exposure improved corrosion protection of the coating as evidenced by an increased impedance of the specimens, the absence of blisters on the panel surfaces and the reduced delamination around the scribe areas of the thermal cycling panels compared with the freshly coated samples.

Keywords: Carbon steel; Phenolic-epoxy coating; pH; EIS; Delamination

5.1 Introduction

The application of organic coatings is the most widely used method of for external corrosion protection [1-2]. Its corrosion protective abilities depend on physical, chemical and mechanical properties including adhesion to a substrate and essential barrier properties against corrosive species, such as water and oxygen [3-4]. The durability of corrosion protection coatings is evaluated based on their effectiveness in providing long-term protection to metallic substrates when these materials are exposed to aggressive corrosion environments.

Coated carbon steel is widely used in marine environments. The main salt in seawater is NaCl, thus, NaCl solutions prepared from deionised water is often used to simulate the effect of salinity in marine environment. Salinity, moisture, and temperature generate internal stress acting at the coating/ substrate interface. This accelerates degradation in the coating which could be observed by loss of adhesion or delamination of the coating. The reliability of a coating thus depends directly on the exposure conditions.

Among the most commonly used marine coatings, phenolic-epoxy coating exhibits chemical and heat resistance properties, along with flexibility and excellent adhesion to metallic substrates [5]. It undergoes extensive cross-linking during the curing stage. Cross-linking confers phenolic-epoxy coating high resistance to corrosion and heat, which is considered an important governing factor for the physical properties of cured resin, [6]. Increasing the molecular weight of the phenolic resin leads to dense molecular structure, which consequently increases resistance to ionic transfer through the coating [7]. General chemical and solvent resistance of the epoxy phenolic coating improves at the expense of some of the flexibility and resistance to alkalis [7]. Indeed, further post-curing of the phenolic epoxy, does not improve resistance to alkali solutions [7]. Although the coating minimises the passage of ions, it can be affected by alkalis and form blistering [7].

Epoxy coatings are also susceptible to degradation at low pH. As noted previously[8-11] hydrolysis is an important reaction causing chain scission in a resin structure. Acids are commonly found in aqueous solutions, and acid-induced hydrolysis is a reaction with water at low pH [9]. Amide-cured and amine-cured epoxies were reported to be vulnerable to degradation in acidic environments and undergo chemical changes that yield bond breaking in an epoxy coating and the reactions scheme shown in Table 5-1

Table 5-1: Functional groups in coating resins that are vulnerable to acid-induced hydrolysis and the proposed chain-scission reaction mechanisms[12].

Name and structure of functional group	Acid hydrolysis reaction scheme	Relative reactivity of example molecules
<p>Amide</p> $\begin{array}{c} \text{O} \\ \parallel \\ \text{R}-\text{C}-\text{N}-\text{R} \\ \quad \quad \quad \diagdown \\ \quad \quad \quad \text{R} \end{array}$	$\begin{array}{c} \text{O} \\ \parallel \\ \text{R}-\text{C}-\text{N}-\text{R} \\ \quad \quad \quad \diagdown \\ \quad \quad \quad \text{R} \end{array} \xrightarrow[\text{H}^+]{\text{H}_2\text{O}} \begin{array}{c} \text{O} \\ \parallel \\ \text{R}-\text{C}-\text{OH} \end{array} + \begin{array}{c} \text{H} \\ \\ \text{N}-\text{R} \\ \quad \quad \quad \diagdown \\ \quad \quad \quad \text{R} \end{array}$	<p>Acetamid</p> $\begin{array}{c} \text{O} \\ \parallel \\ \text{R}-\text{C}-\text{OH} \end{array}$ <p>pH < 1: Marginal reactivity 1 ≤ pH ≤ 6: Stable</p>
<p>Amine</p> $\begin{array}{c} \text{R} \\ \\ \text{N} \\ / \quad \backslash \\ \text{R} \quad \text{R} \end{array}$	$\begin{array}{c} \text{R} \\ \\ \text{N} \\ / \quad \backslash \\ \text{R} \quad \text{R} \end{array} \xrightarrow[\text{H}^+]{\text{H}_2\text{O}} \text{R}-\text{NH}_2 + 2\text{H}-\text{R}$	Not available

Major differences were observed from previous studies in the ability of a phenolic epoxy coating to minimise the lateral spread of corrosion in saline environments at various pH levels. The coating behaviour is affected by differences in pH levels and which conditions (acidic/ alkaline) lead to more coating degradation. Considerations such as these would lead one to anticipate a loss of coating adhesion at low pH in some cases and the more usual displacement at a high pH level. Each disbondment (loss of adherence between metal substrate and cathodic coating occur due to a reduction reaction) would be a function of the acidic/ alkaline nature of the polymeric coating and the substrate surface [13].

The present study evaluated the behaviour of a phenolic epoxy coating, both as fresh samples and after thermal cycling between 22 °C to 120 °C for 40 d. The coatings were then subject to condensation and immersion in various types of corrosive solutions. The first case study was to determine the behaviour of phenolic-epoxy coating after exposure to different NaCl concentration (3.5 and 5 wt. %) solution at 80 °C and exposed to humid conditions (condensing vapour).

In the second case study, coated specimens were tested in the 3.5 wt. % NaCl solution with different pH levels, namely, pH 4.0 and 8.0.

Degradation in the coating was characterised through different methods to compare physico-chemical degradation in the samples. The adhesion of the coating and corrosion products were identified through several methods, such as the amount of coating degradation around a scribe (artificial defect), blister detection and blister grading, EIS, Raman spectroscopy, SEM, and EDS.

5.2 Experiments

5.2.1 Materials

Carbon steel samples (AS3678/ Grade 250) with a nominal chemical composition (wt. %) of 0.22 C, 1.7 Mn, 0.55 Si, 0.04 P, 0.03 S, and Fe balance were cut to dimensions of 170 mm × 50 mm × 6 mm. These were used as substrates for coating application. The surface preparation grade of test panels immediately before coating application complied with ISO 8501-1:2007, Sa 3.

The coating selected in this study is a commercial amine cured phenolic epoxy, the partial chemical composition is illustrated previously in Table 4-1. Phenolic epoxy coating has excellent specifications for corrosion protection from spillage of solvents and chemicals and resistant immersion in saltwater and the maximum operating temperature of the coating is 120 °C (dry heat). A supplier applied one coated film (amine cured phenolic epoxy) to the carbon steel substrates using an airless spray gun. The dry film thickness (DFT) was measured on five areas of a sample surface using a digital gauge (PosiTector 6000), adjusted according to appropriate gauge and calibration standards (MP 2527). The middle regions of some the coated samples were scribed (size 50 mm × 2 mm) using a computer numerical control (CNC) machine.

5.2.2 Exposure conditions

Thermal cycling (22 to 120 °C) was applied to one group of twelve coated samples following the ISO 19277:2018 standard (dry thermal cycling) [14]. The samples were exposed to dry heat at 120 °C in an oven (Binder GmbH, FDL 115, Germany) for 20 h and removed to cool at room temperature (22 °C) for 4 h. Subsequently, the samples were returned to the oven to repeat the process for 40 d. After the thermal cycling exposure was complete, the samples were subjected to corrosion tests.

5.2.3 Setup of the test cell

A schematic of the test setup for evaluating the effect of the NaCl concentration is shown in Figure 5-1. Each glass cell contained three freshly coated samples and three thermally exposed samples. Artificial damage was introduced as scribe on the samples, as

shown in Figure 5-1. Two test solutions were used, either 3.5 or 5 wt.% NaCl. The arrangement of the coated samples is illustrated in Figure 5-1. Four samples were immersed in the solution, while the remaining two were placed on a PTFE holder for condensation exposure. The solution temperature was kept to 80 °C for 60 d while the temperature on the surface of a sample exposed to the vapour phase was 76.5 °C. A condenser was used to minimise liquid loss.

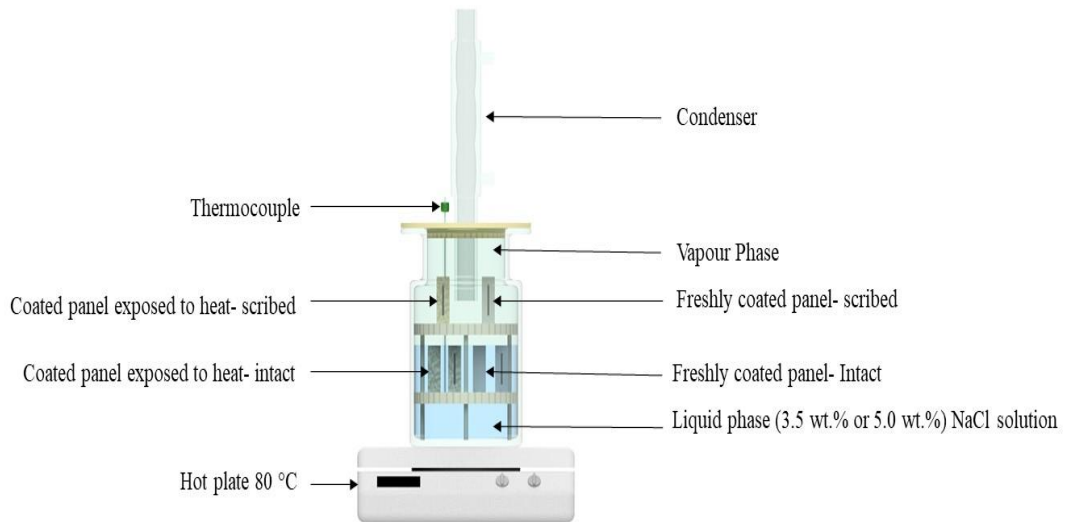


Figure 5-1: Schematic of the experimental setup to study the effects of the NaCl solution concentration on corrosion.

To study the effects of NaCl concentrations, 3.5 and 5 wt.% NaCl solutions were prepared, which had the initial pH of 6.62 and 6.74 at 80 °C (pH sensor, Hanna instrument, the serial number is IC-HI98190). At the end of the experiment, the pH rose to 7.30 and 7.37 for 3.5 and 5 wt. % NaCl solutions, respectively. The increase in pH was attributed to the accumulation of cations generated because of iron dissolution. The pH of the condensed water in the vapour phase was not measured because the liquid volume was insufficient for such measurement.

For experiments interrogating the effect of pH on coating behaviour, 3.5 wt% NaCl solution was prepared, and its pH was controlled to 4 and 8. The same test cell was used in both sets of experiments. In this case, the test solutions were kept at constant temperature for 60 d. The acid solution (pH = 4.0) was adjusted with 12.0 wt. % HCl, whereas the alkaline solution (pH = 8.0) was adjusted using 4.0 wt. % NaOH solution. The test solution was replenished daily, adjusted and measured with a pH meter instrument.

5.3 Coating characterisation techniques

5.3.1 Degree of delamination and corrosion around scribed regions

The scribed areas were unprotected by the coating, thereby allowing coating delamination to initiate. The degree of delamination was assessed as suggested by ISO 4628-8 “Paints and varnishes-evaluation of degradation of coatings. Designation of the quantity and size of the defects and intensity of uniform changes to appearance” [15]. Figure 5-2 shows an example of a delamination area originating from the scribe in the coating on a steel panel after the test.

After the test, the specimens were cleaned with tap water, and dried using compressed air. Loose coating was removed with a blade. The delamination area was then measured with a ruler at six different points uniformly distributed along the scribe. Figure 5-2 shows an example of specimens prepared by this procedure.

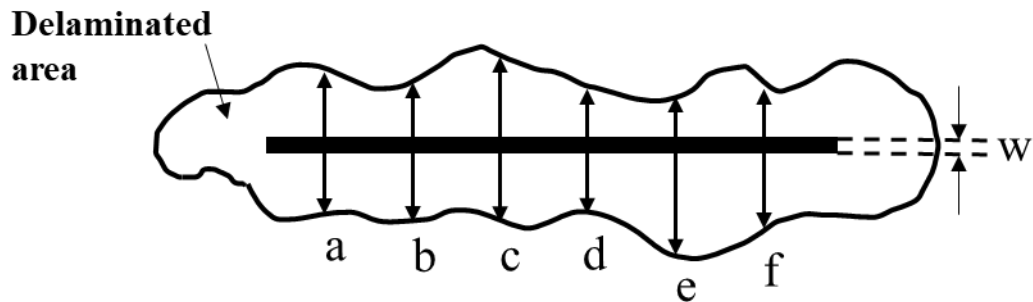


Figure 5-2: The zone of delamination illustrating six measurements. A line (w) marks the artificial scribe.

Subsequently, the mean width of delamination area, w_c was calculated using equation (5-1).

$$w_c = \frac{a + b + c + d + e + f}{6} \quad (5-1)$$

Then, the delamination value c was calculated using equation (5-2).

$$c = \frac{w_c - w}{2} \quad (5-2)$$

w = the width of the original scribe, in millimetres

5.3.2 Blister detection

Blistering is one of the coating defects that commonly occurs when a dry coating film forms a dome-shaped pattern because of the loss of local adhesion between the coating film and the structure [16]. The degree of blistering was visually determined based on ISO 4628-2 [17]. The ISO standard characterises blistering level using two parameters, namely, blister size (ranging from 0 to 5, where 1 represents microscopic size and 5 represents blisters larger than 5 mm in diameter) and blister density (each degree of size corresponds to four degrees of frequency).

5.3.3 EIS

Coating performance after exposure to corrosive environments was evaluated using EIS. A glass tube with an exposed area of 14.6 cm² and a height of 8 cm was placed on a coated panel and tightly sealed with a mechanical clamp as shown in Figure 5-3. On scribed coated panels, the EIS cell was placed on the coating 20 mm from the scribed area, ensuring the steel substrate was not exposed to the electrolyte. The electrolyte was 3.5 wt. % NaCl solution at 24 ± 1 °C, and the total volume of electrolyte in the glass cell was 100 mL. A conventional three-electrode cell consisting of Ag/AgCl was filled with 3 M KCl electrolyte as the reference electrode, with the tip placed 1 to 3 mm from the coating surface. A graphite rod was used as a counter electrode and the coated carbon steel served as the working electrode.

EIS measurements were conducted using a Gamry potentiostat (Interface 1010E™) operated at OCP. A 20 mV (r.m.s) sinusoidal perturbation was applied in the frequency range of 100 kHz to 10 mHz with six points per decade. The measurements were taken at intervals of 1 h for 1 d. The EIS curves were analysed using Gamry Echem Analyst™ software.

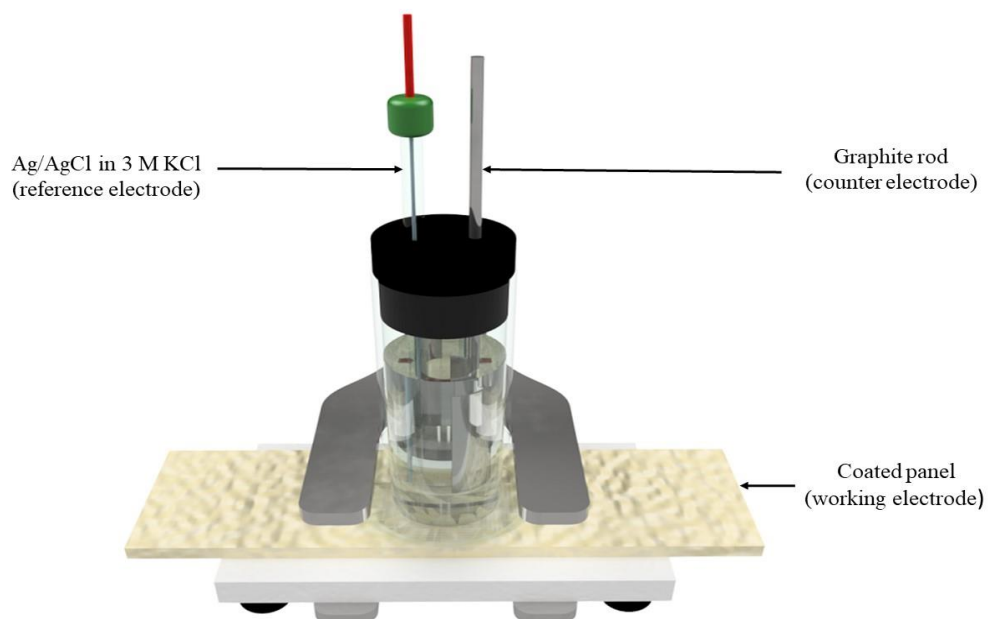


Figure 5-3: Schematic of the electrochemical cell used for testing the coated metal samples.

5.3.4 Characterisation of corrosion products

The morphologies and elemental compositions of the corrosion products were characterised with scanning electron microscopy, SEM (Mira instrument, Tescan) combined with energy dispersive X-ray spectroscopy (EDS). Aztec software (Oxford Instruments) was used to collect X-ray signals from the metal surface and analyse the elemental composition data obtained from corrosion products under a detached coating. The samples were cross-sectioned by cold mounting a test specimen in epoxy resin. The mounted samples were cut using Accutom-50 (Struers, Denmark), and their surfaces were polished using 1200 grit SiC abrasive paper.

The chemical compositions of the corrosion products were analysed using a WITec Alpha 300 SAR+ confocal Raman microscopy, and a frequency-doubled neodymium-doped yttrium aluminium garnet (NdYAG) laser with an excitation wavelength of 532 nm (green). Light was collected with a 20×0.4NA Zeiss objective and fed into the spectrometer via an optical fibre with a diameter of 40 μm.

5.3.5 Thermal analysis

Thermal analysis system TGA/DSC 3+ (Mettler Toledo AG, Switzerland) was used for both TGA and DSC. The measurements were carried out in the temperature range from 25

to 800 °C, at the heating rate of 10 °C min⁻¹, under nitrogen (100 mL·min⁻¹). 10 mg of the samples scraped from the top layer of the coating surface were placed in a 110 µL platinum open pan. For TGA analysis, the sample weight as a function of temperature was monitored and recorded by a PC connected with the Mettler Toledo AG apparatus. At the end of each run, the experimental data were used to plot the percentage of undegraded sample ($I-D$) % as a function of temperature, where $D = (W_0 - W) / W_0$ and W_0 and W were the masses of sample at the starting point and during scanning [18].

DSC is used to measure the temperatures and heat flows associated with exothermic and/or endothermic changes that occur during thermal transitions in a material. The sample was heated from 25 °C to 200 °C per min. in a nitrogen atmosphere flowing at 50 ml per min. The glass transition temperature (T_g) is used to determine a material's thermal stability, which indicates the coating's toughness [19].

5.4 Results and discussion

5.4.1 Influence of NaCl concentrations

5.4.1.1 Degree of delamination

The images in Table 5-2 and Table 5-3 show the appearance around the scribe region of the phenolic-epoxy coated specimens before and after the tests with 3.5 wt. % and 5.0 wt. % respectively.

It is apparent that the exposure to heat alone resulted in a colour changes. The yellowing of epoxy coatings were extensively reported [20]. After the coating was exposed to moisture, corrosion products are visible. It can also be observed from Table 5-2 and Table 5-3 that the samples exposed to water condensation were most susceptible to delamination, compared to the samples fully immersed in the 3.5 wt. % and 5.0 wt. % NaCl solutions.

Table 5-2: Degree of delamination in the phenolic- epoxy coating after exposure to a corrosive environment (3.5 wt.% NaCl condition).













	Pre-exposure to the test	Immersion in 3.5 wt.% NaCl solution at 80 °C for 60 d	Exposed to condensing vapour at 80 °C for 60 d
Freshly coated panel			
A coated panel exposed to thermal cycling of 22 to 120 °C for 40 d			

Table 5-3: The experimental results to phenolic- epoxy coating after exposure to a corrosive environment (5 wt.% NaCl condition).

	Pre-exposure	Immersion in 5.0 wt.% NaCl solution at 80 °C for 60 d	Exposed to condensing vapour at 80 °C for 60 d
Freshly coated panel			
A coated panel exposed to thermal cycling of 22 to 120 °C for 40 d			

The lesser delamination risk at the scribe region when the samples were fully immersed may be attributed to the diffusion limit of the oxygen reduction reaction, resulting in lower hydroxyl ions being generated (equation (5-3)) [21-22]:



This is similar to what was previously reported by Leidheser et al.[23] where the authors found no significant delamination occurred on the 7 mm diameter defect on steel panels coated with epoxy when oxygen was excluded from the system. In the current study, the delamination occurred only when the water condensation took place on the surface. The thinner layer of electrolyte could enhance the mass transport of dissolved oxygen to the metal surface. In addition, the limited quantity of electrolyte could facilitate the formation of corrosion products as their solubilities limits are readily reached [24].

The average delamination width is compared in Figure 5-4. The results show that the samples exposed to the vapour phase in the test cell containing 3.5 wt. % NaCl suffered greater delamination than those placed in the test cell comprising 5.0 wt. % NaCl. Delamination was reduced after the coated panels were thermally exposed prior to immersing in cells 3.5 and 5.0

wt. % NaCl. Increasing the NaCl concentration may reduce the water evaporation because the dissolved salt ions reduce the water activity (reduce the free energy) [25].

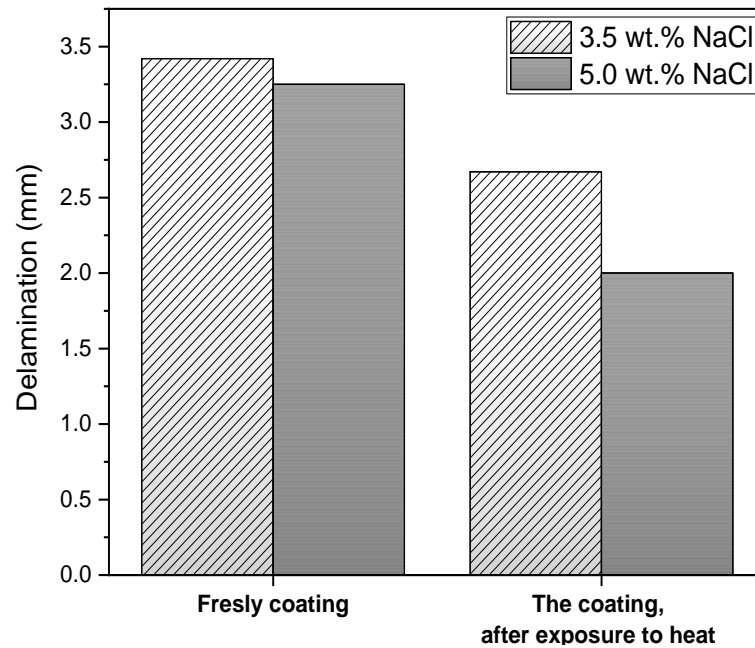


Figure 5-4: Comparison of delamination results on phenolic-epoxy coated panels exposed to the vapour phase in different test cells containing 3.5 and 5.0 wt. % of NaCl.

5.4.1.2 Degree of blistering

The density of blistering spots with a diameter larger than 200 μm is shown in Figure 5-5. After 1400 h of testing in both test cells, blisters were observed only in the freshly coated panels immersed in 3.5 and 5 wt. % NaCl solutions. The blister concentration was significantly higher in the freshly coated panel with an artificial scribe and immersed in a 3.5 wt. % NaCl solution, compared to that in a 5.0 NaCl solution (black and white images were processed using ImageJ).

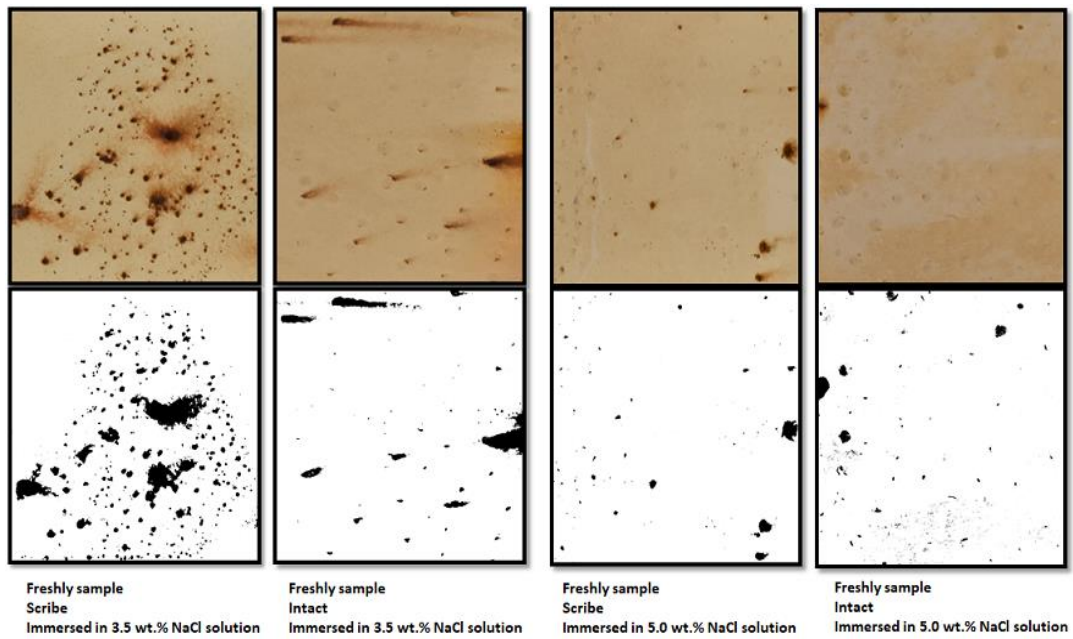


Figure 5-5: Photographs of samples after immersing in 3.5 and 5.0 wt. % NaCl solutions at 80 °C for 60 d, without pre-exposure to heat.

Figure 5-6 illustrates the blistering level (defined by ISO standard 4628-2 [17]) of the coatings subjected to different concentrations of NaCl solution at 80 °C. Blisters were observed on all freshly coated panels. Blister formation was accelerated for the scribed sample immersed in 3.5 wt.% NaCl solution, reaching a size of 4 mm and a density of 4 (S4) after 504 h. The other freshly coated panels showed blisters up to 3 mm in size with a density between 3 (S3) and 4 (S4). The freshly applied phenolic-epoxy coatings are less suitable for immersion in marine environments compared with thermally pre-treated ones.

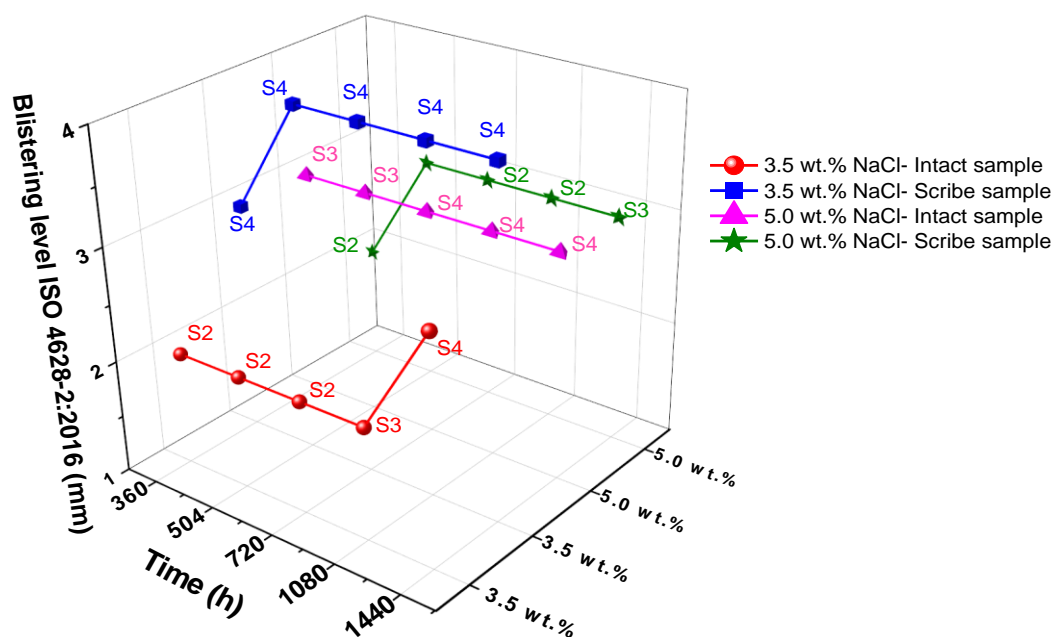


Figure 5-6: Blistering level of freshly coated samples as a function of NaCl concentration and time. ISO 4628-2:2016 defined the density of blisters (0: none to 5: many). The data labels represent the blister size (S1: none to S5: >5 mm).

The results also demonstrated that the phenolic epoxy was more sensitive to blistering in the 3.5 wt. % than 5.0 wt. % NaCl. The aggressive corrosive species such as water, oxygen and ions percolate through a coating to reach the coating-metal interface area and degrade the coating film [13, 26]. The oxygen concentration in the solution is an important influence factor for the corrosion process due to the cathodic reaction equation (5-3). Increased sodium chloride concentration reduces oxygen solubility and water activity in sodium chloride solution; both can reduce cathodic reaction [27-28]. The oxygen solubility in sodium chloride depends on electrolyte's composition concentration. Stephen et al. [29] reported O_2 solubility in high salinity solutions (0.3 wt.% NaCl) at 80 °C of 0.81 ppm, whereas it was greater 2.3 ppm in low salinity (0.05 wt.% NaCl). The anodic reaction is iron oxidation at the blister's centre, dissolved oxygen in the solution is reduced at the surface according to equation (5-3) [30]. This leads to high pH regions at the edges of the blister causing delamination of the coating. The generation of OH^- ions at the substrate/coating interface enhance the osmotic pressure difference [31-32].

5.4.1.3 Electrochemical performance

The Nyquist plots of electrochemical impedance under different concentrations of NaCl 3.5 and 5.0 wt.%, as shown in Figure 5-7 and Figure 5-8, can be categorised by three patterns.

- Pattern A: All coated panels exposed to condensation conditions (80 °C for 60 d) were characterised by a single semi-circle with high impedance, suggesting that water penetrated the coating but did not reach the coating–metal interface.
- Pattern B: Coated panels exposed to heat and immersed in different solution concentrations for 60 d were characterised by reduced resistance. The EIS plots show a semi-circle in a capacitive loop that changes at a high frequency, implying that corrosive media reached the coating–metal interface. Moreover, the coated panels immersed in 3.5 wt. % NaCl solution (Figure 5-7) show a different semi-circle loop than other samples, along with an oblique line at high frequencies, indicating that the coating was intact.
- Pattern C: Freshly coated panels immersed in different concentrations of NaCl solutions for 60 d were characterised by Nyquist plots with a single distinct semi-circle capacitance loop and a linear curve at low frequencies, indicating that the diffusion of corrosive species through pores in the coating occurred, followed by the development of corrosion products at the coating–metal interface [22].

Figure 5-8b confirmed good protective properties of the coating in a test cell that contained 5.0 wt.% NaCl solution. A slight decrease was detected on the scribe coating panel exposed to heat and immersed in solution. A semi-circle indicated a reduction of the coating resistance [22].

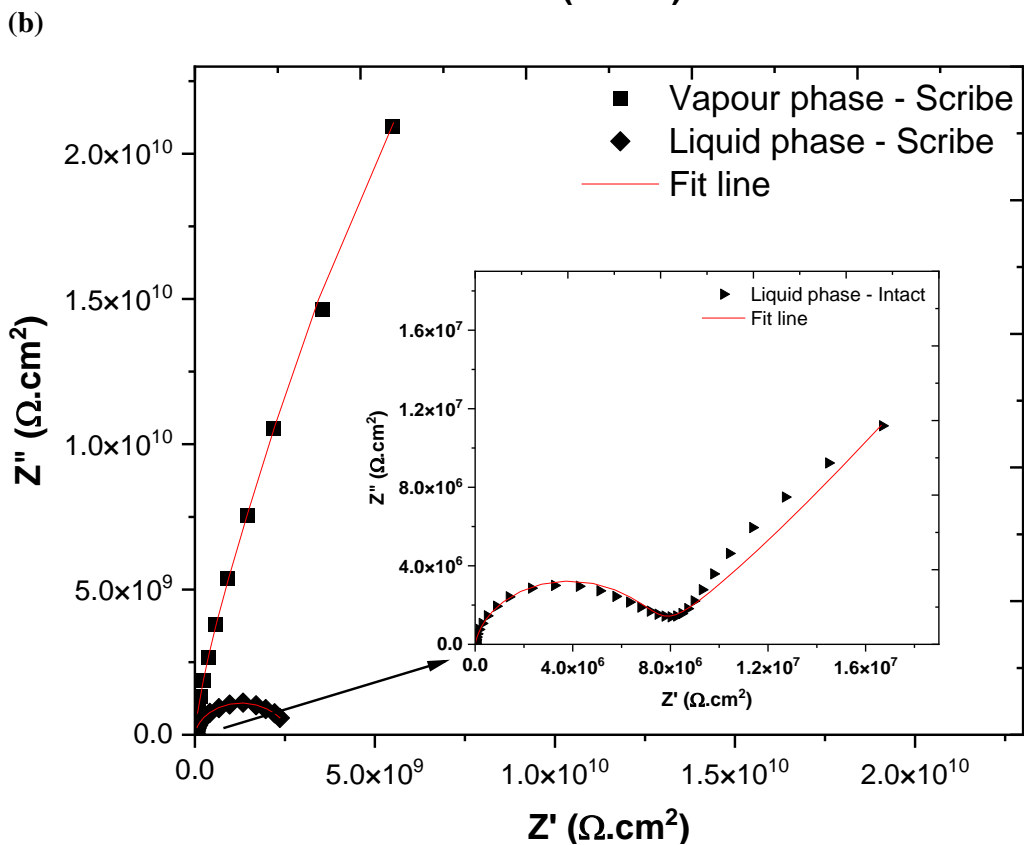
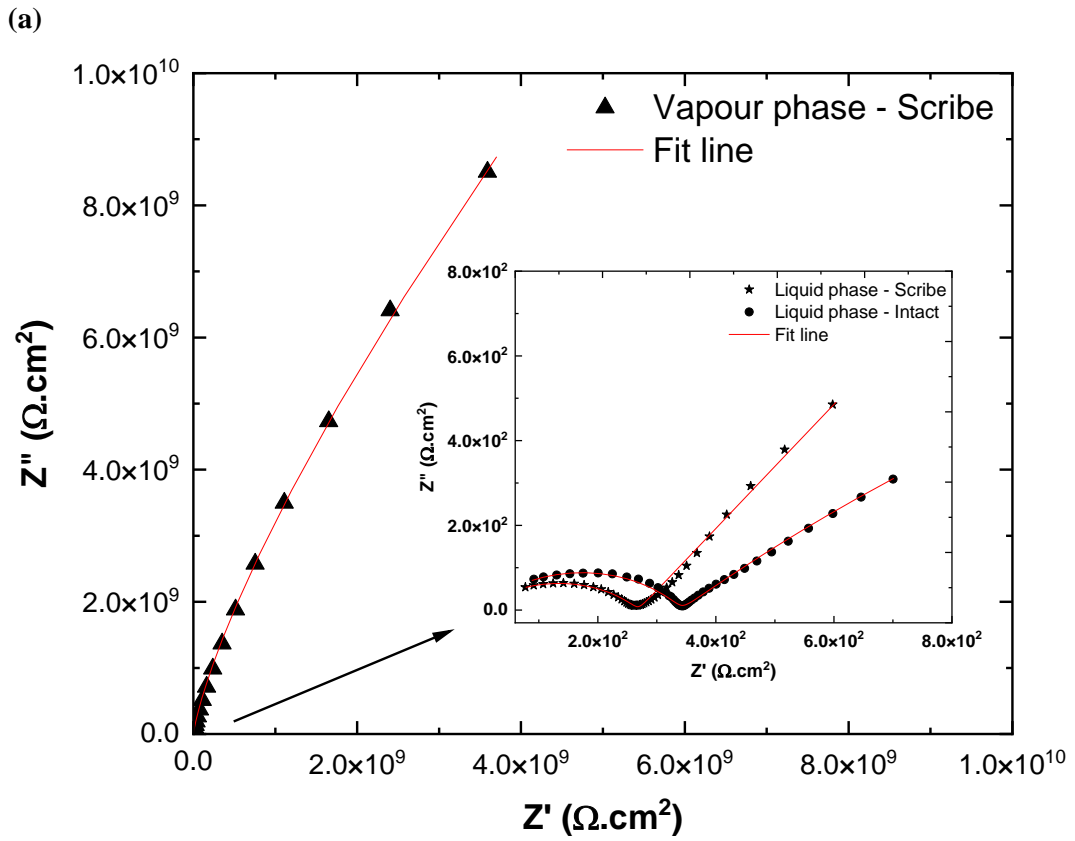


Figure 5-7: Nyquist plots of phenolic-epoxy coating after 1440 h exposure to 3.5 wt. % NaCl condition at 80 °C in glass cells containing (a) the freshly coated panels, (b) coated panels exposed to heat.

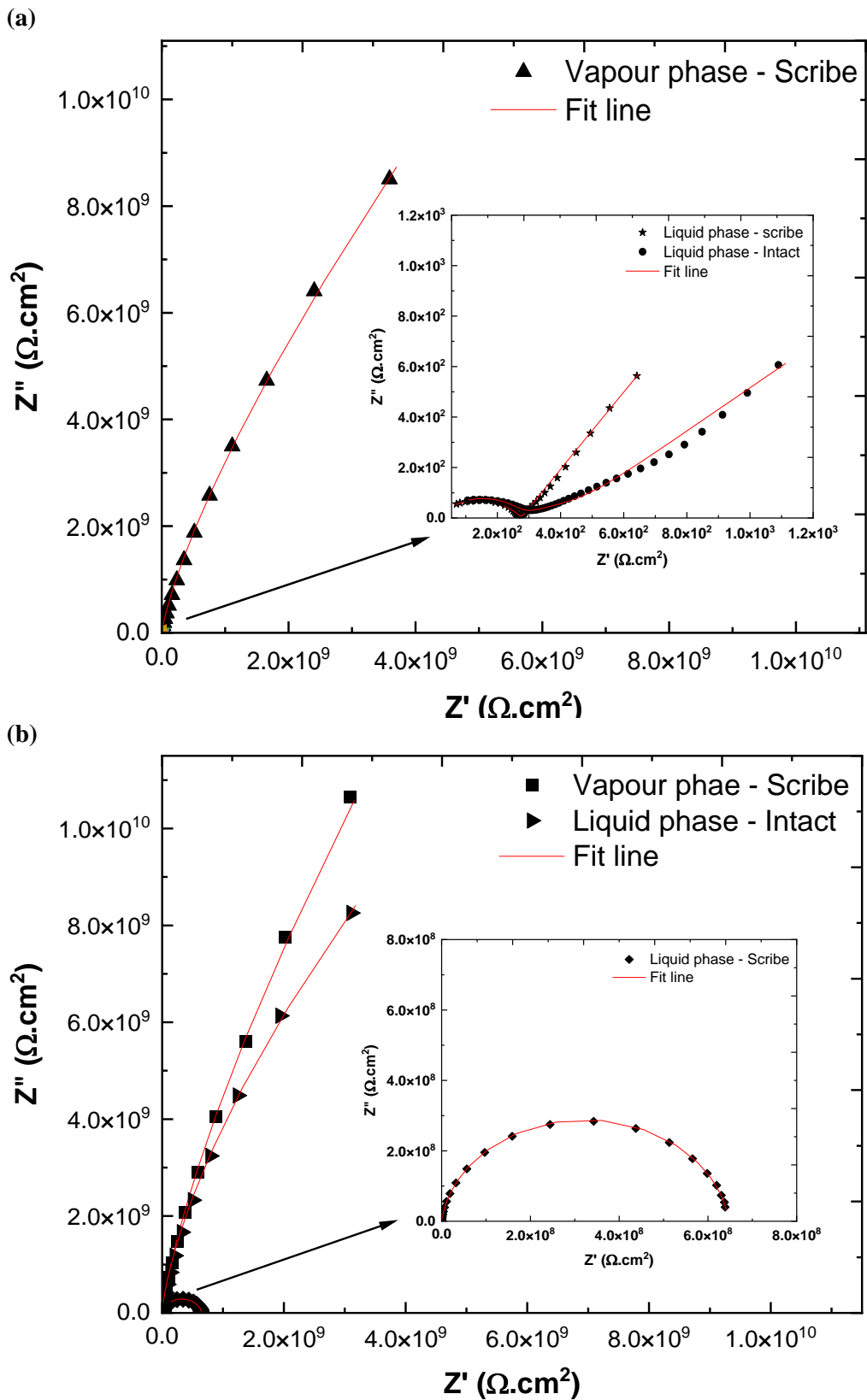


Figure 5-8: Nyquist plots of phenolic-epoxy coating after 1440 h exposure to 5.0 wt.% NaCl condition at 80 °C in glass cells containing (a) the freshly coated panels, (b) coated panels exposed to heat.

Figure 5-9 and Figure 5-10 illustrate the evolution of Bode plots of wholly coated panels exposed to the condensated water (vapour phase); these samples exhibited the highest impedance of 10^9 to $10^{10} \Omega \cdot \text{cm}^2$. Furthermore, the intact coated specimen exposed to heat and then immersion in 5.0 wt.% NaCl solution had an impedance of $10^9 \Omega \cdot \text{cm}^2$ (Figure 5-10c). A slightly reduced in impedance occurred in the scribed coated panel that was exposed to the heat and then immersed in 5.0 wt.% NaCl solution, which was i.e. $10^8 \Omega \cdot \text{cm}^2$ (Figure 5-10c).

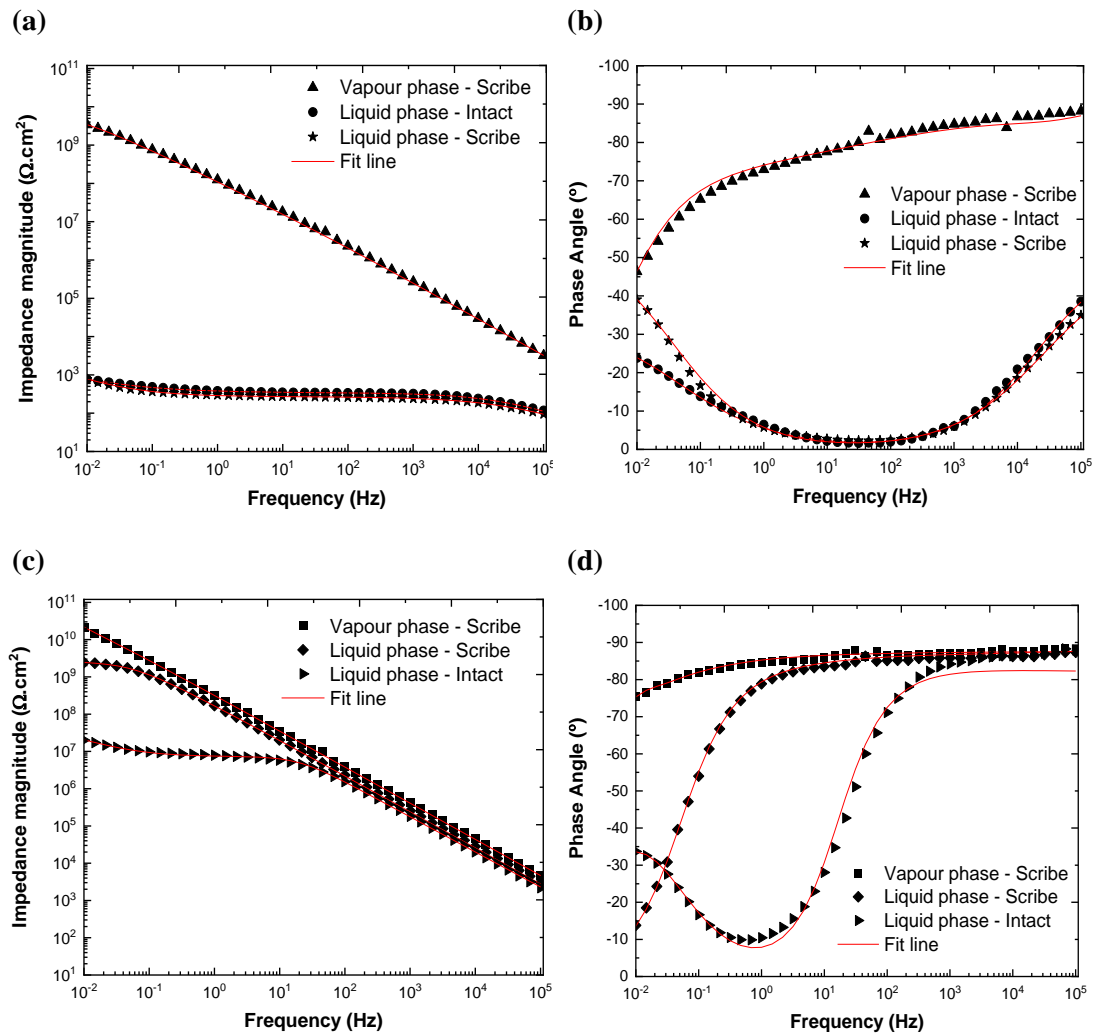


Figure 5-9: Bode plots of coated panels with phenolic epoxy exposed to different conditions vapour and liquid in test cell containing on 3.5 wt. % NaCl solution; (a-b) the freshly coated panels, and (c-d) coated panels exposed to heat.

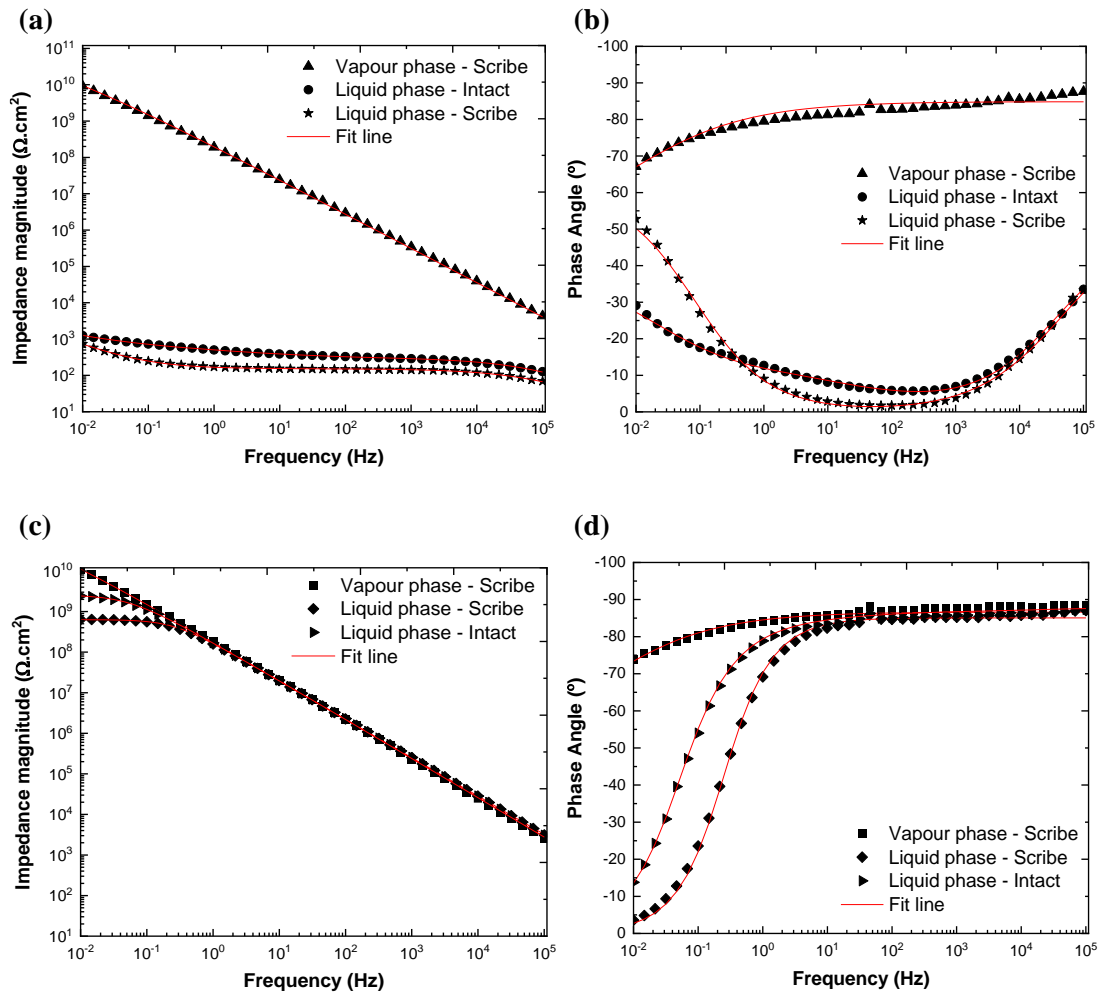


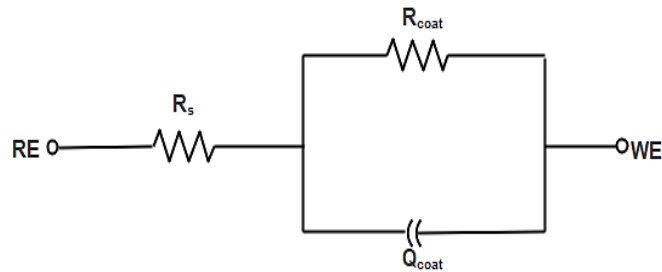
Figure 5-10: Bode plots of coated panels with phenolic epoxy exposed to different conditions vapour and liquid in test cell containing on 5.0 wt. % NaCl solution; (a-b) the freshly coated panels, and (c-d) coated panels exposed to heat.

The intact coated sample exposed to the heat and then immersion in 3.5 wt.% NaCl solution had the least impedance among heated and entirely coated specimens. Its impedance value was $10^7 \Omega \cdot \text{cm}^2$, which is slightly higher (Figure 5-9c). A simple equivalent circuit is shown in (Figure 5-11a); solution resistance R_s , coating resistance R_{coat} , and constant phase element Q_{coat} are commonly used for systems with a one-time constant [33-34].

Whole freshly coated specimens immersed in different concentrations of NaCl had low impedance Figure 5-9a and Figure 5-10a, which reflected defects on the coating films (blisters), as shown in Figure 5-5. The shape of the plots for a coated metal, displayed two minima in the phase plot. The one at high frequency reflects the physical behaviour of the coating (Q_{coat} , R_{coat}) whereas that at intermediate frequencies corresponds to the corrosion

reactions at the interface between the metal and coating (Q_{dl} , R_{ct} and W) as shown in Figure 5-11b.

(a)



(b)

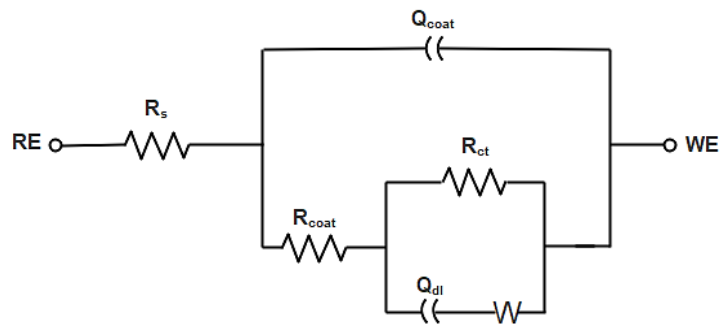


Figure 5-11: Equivalent circuit of the impedance of coated metals: (a) All coated panels exposed to heat and (b) freshly coated panels immersed in 3.5 and 5.0 wt.% of NaCl solution around 60 d.

The corresponding fitting results are illustrated in Table 5-4 and Table 5-5. The changes in the impedance of fresh coating were immersed in different solutions because of an accumulation of corrosion products at the metal/ coating interface. Moreover, the increase of CPE in the coating ($\sim \times 10^{-10}$ to $10^{-6} F \cdot s^{\alpha-1} \cdot cm^{-2}$) indicates an increase in the water that is permeated into the coating.

Table 5-4: EIS data of the coating panels tested in a test cell containing 3.5 wt. % NaCl solution at 80 °C for 60d.

<i>Type of coated panels</i>	R_{coat} ($\Omega \cdot \text{cm}^{-2}$)	R_{ct} ($\Omega \cdot \text{cm}^{-2}$)	Q_{coat} ($\text{F} \cdot \text{s}^{\alpha-1} \cdot \text{cm}^{-2}$)	Q_{dl} ($\text{F} \cdot \text{s}^{\alpha-1} \cdot \text{cm}^{-2}$)	W ($\text{F} \cdot \text{s}^{\alpha-1} \cdot \text{cm}^{-2}$)	X^2
Exposed to heat – Vapour Phase – Scribe	1.12×10^{10}		9.32×10^{-10}			4.98×10^{-4}
Freshly – Vapour Phase – Scribe	2.12×10^9		8.41×10^{-10}			1.23×10^{-4}
Exposed to heat – Liquid Phase – Scribe	1.25×10^9		1.03×10^{-10}			6.12×10^{-4}
Exposed to heat – Liquid Phase – Intact	2.12×10^7		1.12×10^{-9}		2.25×10^{-4}	5.22×10^{-3}
Freshly – Liquid Phase – Scribe	361.6	281.2	1.13×10^{-6}	0.29×10^{-3}	4.98×10^{-3}	1.41×10^{-3}
Freshly – Liquid Phase – Intact	332.9	307.1	1.57×10^{-6}	1.4×10^{-3}	1.85×10^{-3}	4.23×10^{-4}

Table 5-5: EIS data of the coating panels tested in a test cell containing 5.0 wt. % NaCl solution at 80 °C for 60d.

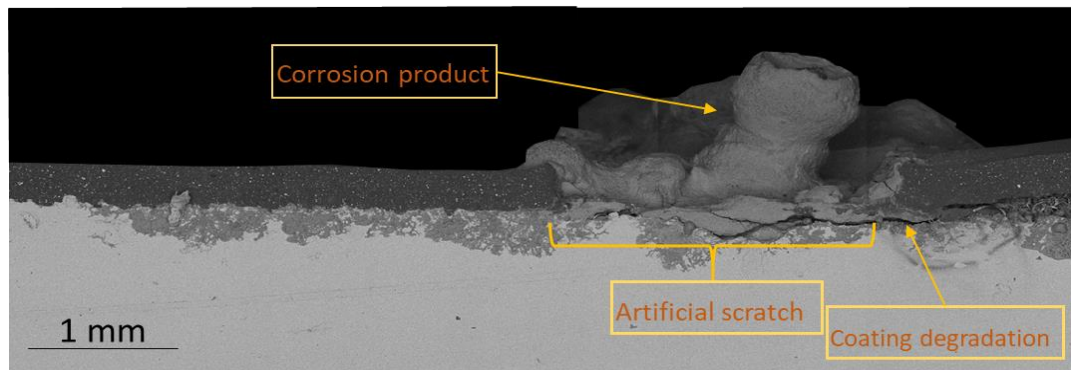
<i>Type</i>	R_{coat} ($\Omega \cdot \text{cm}^{-2}$)	R_{ct} ($\Omega \cdot \text{cm}^{-2}$)	Q_{coat} ($\text{F} \cdot \text{s}^{\alpha-1} \cdot \text{cm}^{-2}$)	Q_{dl} ($\text{F} \cdot \text{s}^{\alpha-1} \cdot \text{cm}^{-2}$)	W ($\text{F} \cdot \text{s}^{\alpha-1} \cdot \text{cm}^{-2}$)	X^2
Exposed to heat – Vapour Phase – Scribe	1.81×10^{10}		4.32×10^{-10}			6.10×10^{-4}
Freshly – Vapour Phase – Scribe	2.01×10^{10}		2.12×10^{-10}			8.01×10^{-4}
Exposed to heat – Liquid Phase – Scribe	8.1×10^8		2.1×10^{-9}			2.0×10^{-4}
Exposed to heat – Liquid Phase – Intact	4.01×10^9		1.02×10^{-10}			6.12×10^{-4}
Freshly – Liquid Phase – Scribe	2.98×10^3	2.1×10^3	2.3×10^{-6}	9.32×10^{-3}	3.31×10^{-3}	1.02×10^{-3}
Freshly – Liquid Phase – Intact	671.6	620	1.72×10^{-6}	4.22×10^{-3}	3.41×10^{-4}	3.21×10^{-3}

5.4.1.4 Characterisation of corrosion product layers

Raman spectroscopy (RS) and SEM/EDS were used to characterise the corrosion product associated with the observed delamination on the coating film at the artificial scribed area.

Figure 5-12a and b illustrate the cross sections of the scribe region of the coated steels exposed to condensation and immersion, respectively. Figure 5-12a shows the cross-section in the overlaid optical microscopic images of the rust layer formed on the scribe in the vapour phase. The thickness of the rust layer can be seen, which is up to 2 mm. The delamination between coating and the substrate is also visible. At the same time, the corrosion product in the liquid phase was thin with some cracks and pores, which had no impact on the coating film as shown in Figure 5-12b.

(a)



(b)

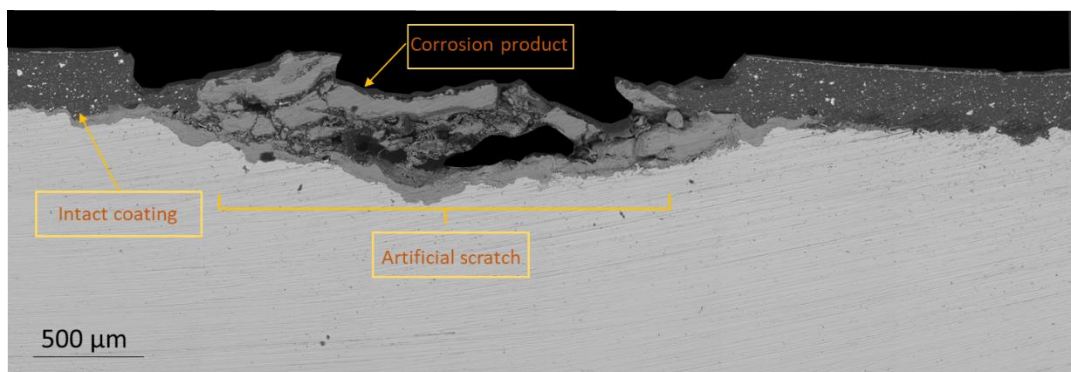
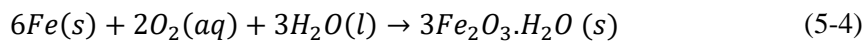


Figure 5-12: SEM of corrosion products, especially the cross-sections of under the coated film exposed to heat treatment: (a) coating sample exposed to water condensation (vapour phase) (b) the coating panel immersed in 3.5 wt. % NaCl solution (liquid phase).

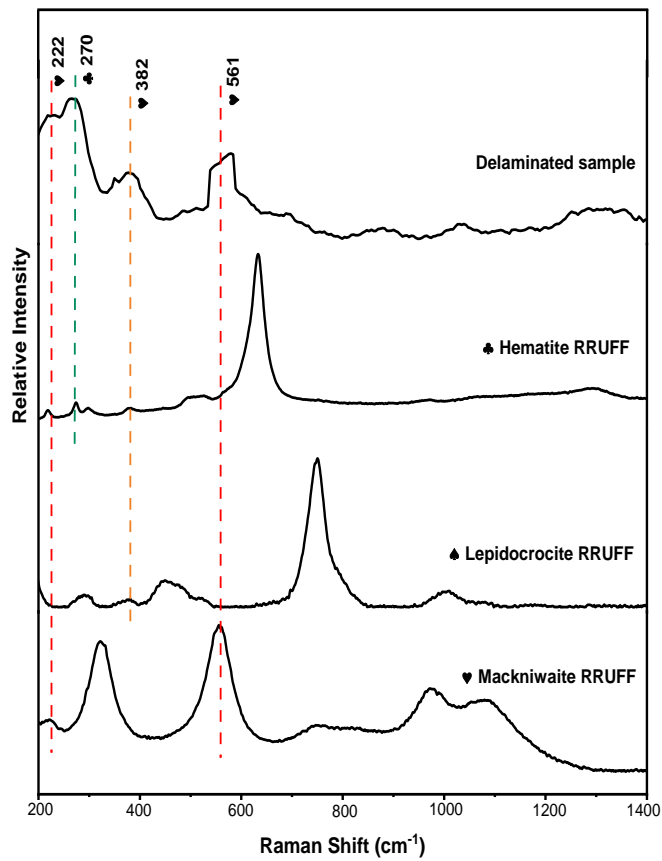
In the Raman results shown in Figure 5-13, two Raman spectra were distinct from the corrosion products formed on the scribe line at different conditions (liquid and vapour), with related RRUFF™ database spectra as the reference [35]. The strong peaks of 222, 270, 382

and 561 cm^{-1} were observed on the delaminated coated sample. The Raman spectra reflected that hematite ($\alpha\text{-Fe}_2\text{O}_3$), lepidocrocite ($\gamma\text{-FeOOH}$) and mackinawite (FeS) formed on the samples, and these were compared with RRUFF databases spectra of all possible iron oxidation products. However, in the coated panel that did not exhibit detachment, as illustrated in (Figure 5-12b), Raman spectra show dominant peaks at approximately 218 and 265 cm^{-1} . These findings indicated the corrosion product under formed under the coating film were $\gamma\text{-FeOOH}$ and FeS .

It could distinguish that the component $\alpha\text{-Fe}_2\text{O}_3$ was found only under the coating film that detachment. It is the last step in the oxidation of iron hydroxide, referred to as rust [36] that could occur as follows:



(a)



(b)

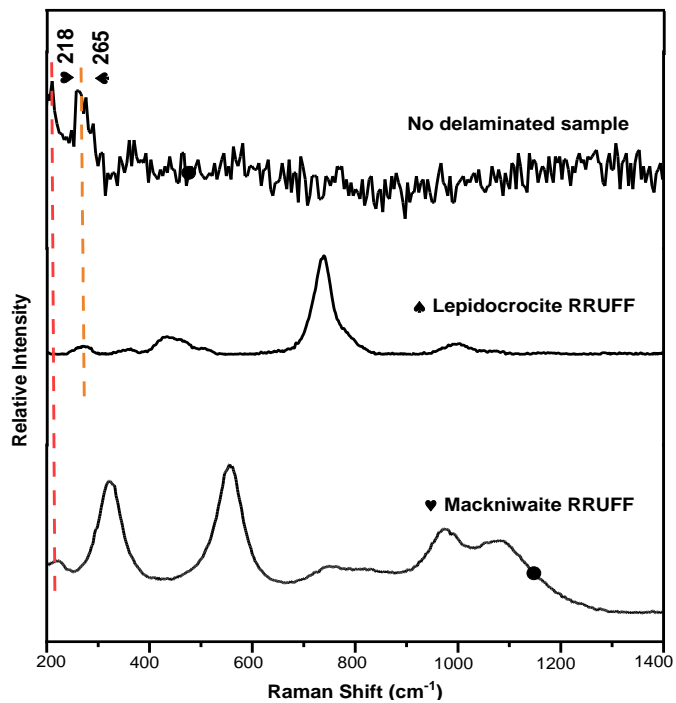


Figure 5-13: Raman spectra of corrosion-product layers formed under the coating for samples (a) with and (b) without delamination. Reference spectra from the RRUFF database.

The SEM/EDS was also used to inspect the blisters on the coating film and identify elements present in a cross-section of the substrate and coating, as shown in Figure 5-14 and Figure 5-15. It should be noted that blisters were formed only on the fresh coated panel, thus cross-sectional analysis was only performed on these panels. Figure 5-14 illustrates that a blister is approximately 48 μm high. The image shows that the coating consisted of one layer. Additionally, corrosion product was observed on the substrate, under the blister. Elemental mapping indicated that Fe, O, C and Cl are dominant elements in the corrosion product. S and O were also found in the coating layer, which may be part of the formulation as flame retardants in epoxy resin [37-38]. The leaching of S species from the coating is beyond the scope of this work.

The anodic reaction significantly accelerates the Fe^{2+} ion, which reacts with S^{2-} ion that was released from the coating film to form iron sulfide (mackinawite) as illustrated in Figure 5-13 and Figure 5-15, and the reaction could occur as follows [39]:



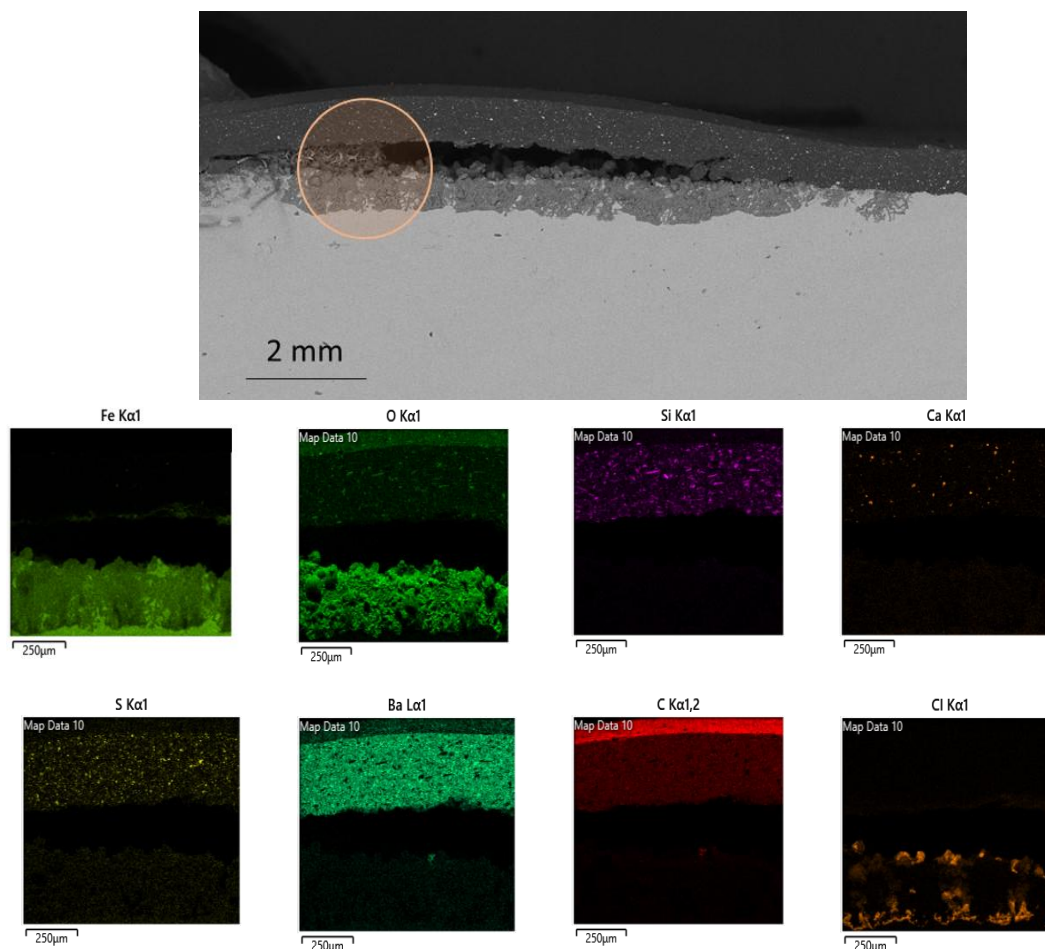


Figure 5-14: SEM/EDS image of blister region with corrosion products at the metal/coating interface and a partially detached coating.

Figure 5-15 shows a top-view image of another blister with a diameter of about 4 mm after coating removal. Fe, O, C, Cl and S elements dominated on the rust layer. Chloride ions could permeate through a coating film, increasing the conductivity in the water, the severity of corrosion on the substrate and the degradation of an organic coating on the steel. It seems that the freshly applied coating used in this study was not suitable to be used in NaCl immersion conditions.

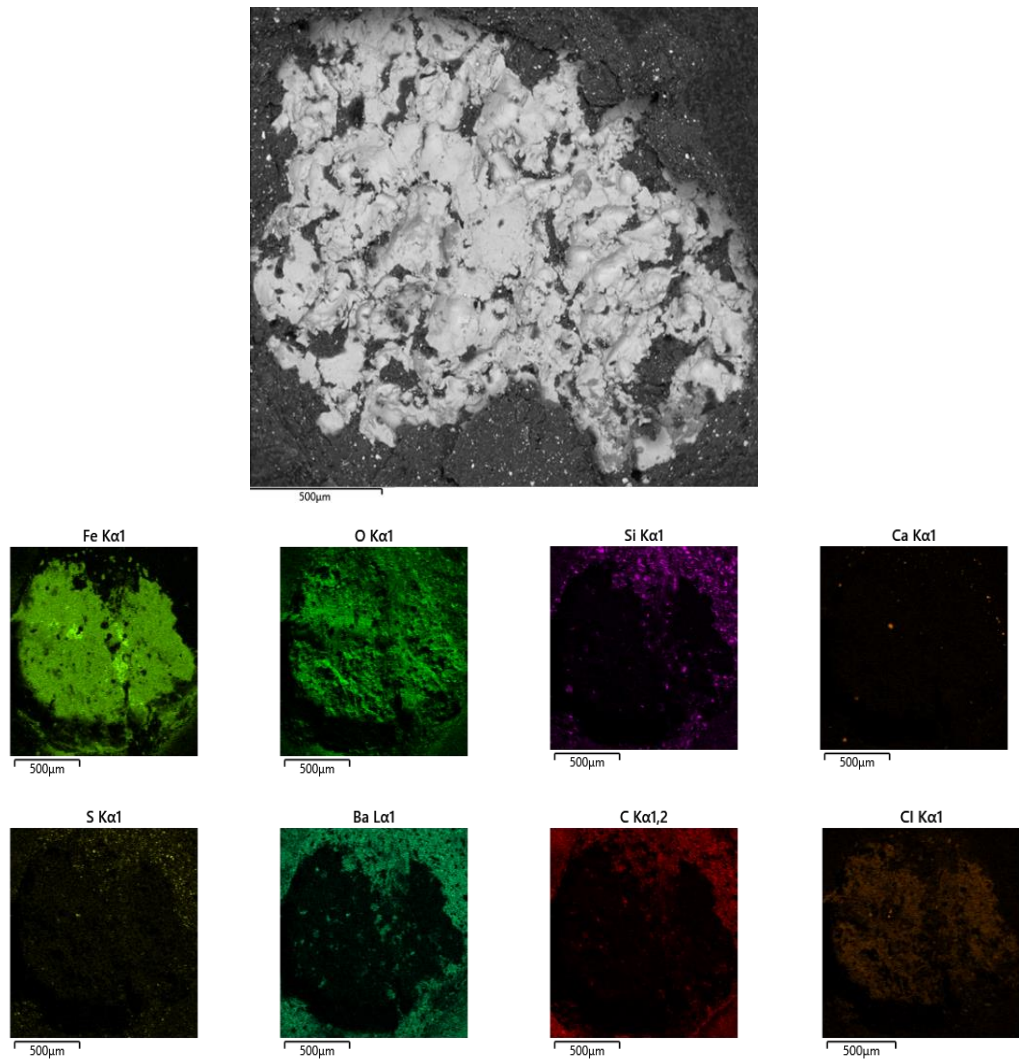


Figure 5-15: SEM/EDS image of blister with corrosion products at the metal/coating after coating removal.

5.4.2 Influence of pH levels

In this section, the behaviour of the same phenolic epoxy coating was investigated as a function of the solution pH at the same NaCl concentration of 3.5 wt%. The experimental regime was similar to that described in section 5.2.

5.4.2.1 Degree of blistering

After 1400 h of exposure to the test solution, blisters were observed only on the freshly coated panels immersed in 3.5 wt.% NaCl solution at pH = 8.0. Remarkably, no such blistering was observed on panels that had undergone heat treatment. Table 5-6 and Table 5-7 compare the freshly coated specimens immersed in 3.5 wt.% NaCl solutions of different pH levels (4.0 and 8.0), respectively. Table 5-6 also shows the density of blistering spots with a diameter larger than 300 μm . Blister concentration was significantly higher on both intact and scribed freshly coated panels. On the other hand, coated panels when immersed in 3.5 wt. % NaCl (pH 4.0) solution, as shown in Table 5-7, show no blisters or failure.

Table 5-6: Photographs of samples after immersing in 3.5 wt. % NaCl solution (pH 8.0) at 80 °C for 60 d, without pre-exposure to heat.

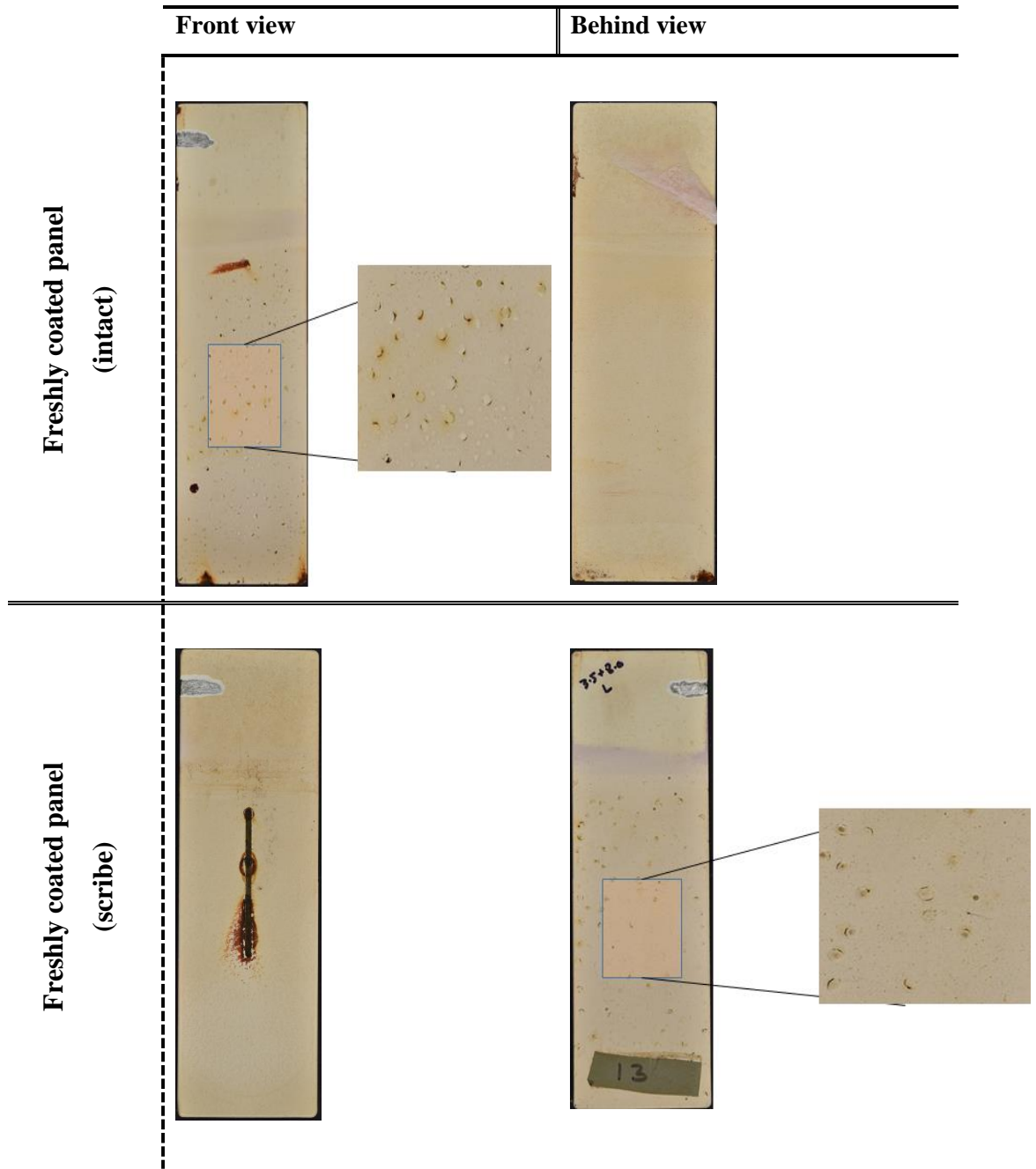


Table 5-7: Photographs of samples after immersing in 3.5 wt. % NaCl solution (pH = 4.0) at 80 °C for 60 d, without pre-exposure to heat.

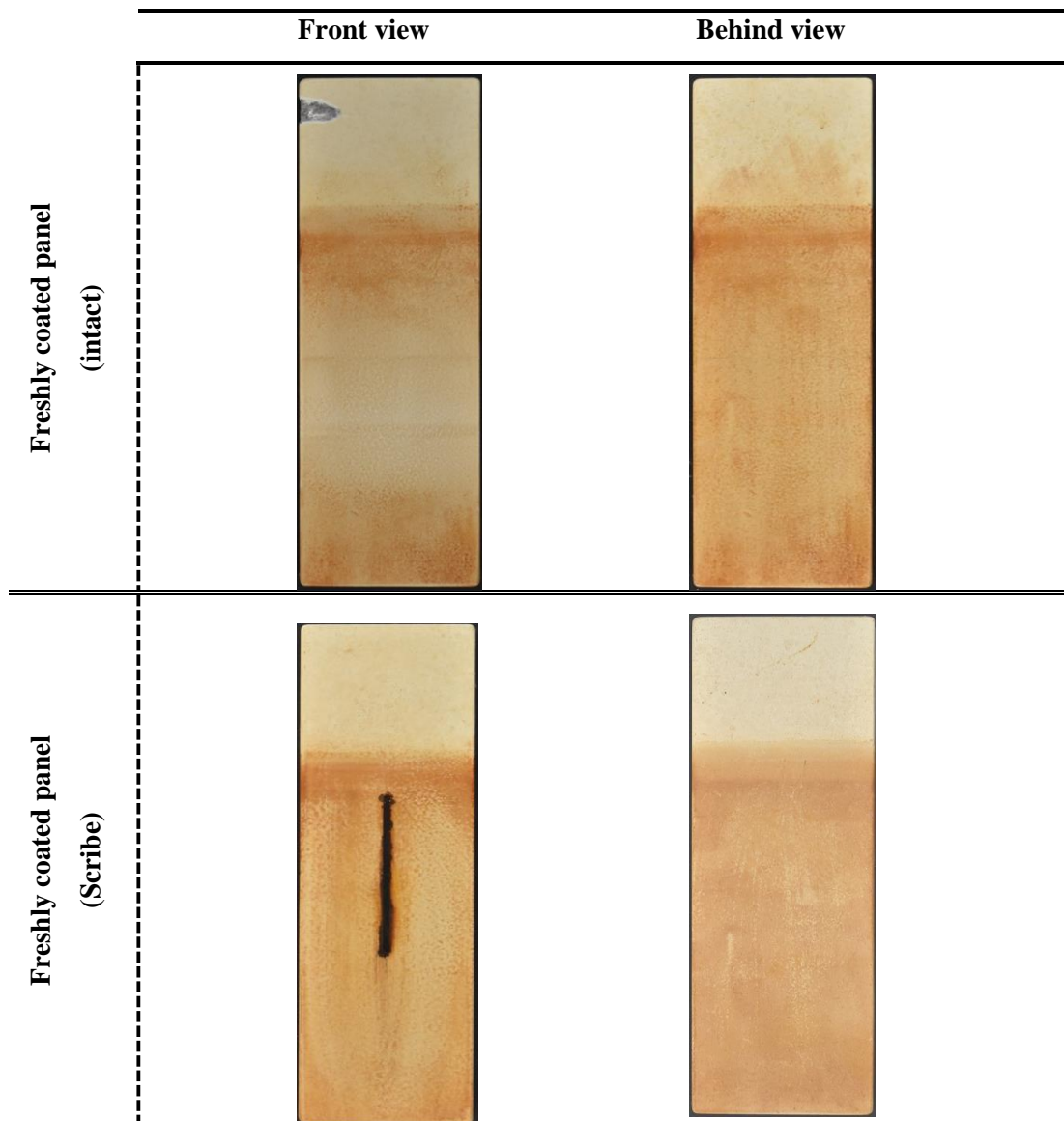


Figure 5-16 shows a comparison of the blistering level on the coating film at different test conditions. Blisters were observed in freshly coated panels immersed in (pH = 8.0) 3.5 wt.% NaCl solution, and formation accelerated in the scribed sample. These blisters reached to 4 mm in diameter and a density of 4 (S4) after 504 h on a scribe panel and after 1080 h on an intact sample. The rest of the freshly coated panels immersed in pH 4.0 solution had no blisters on the coating panels during the test period. It is evident that the freshly applied phenolic-epoxy coating used in this study was not suitable for immersion in 3.5 wt.% NaCl solution-pH = 8.0. Notably, pre-exposure to thermal cycling enhanced the coating's resistance, effectively preventing the formation of blisters on the coating layer.

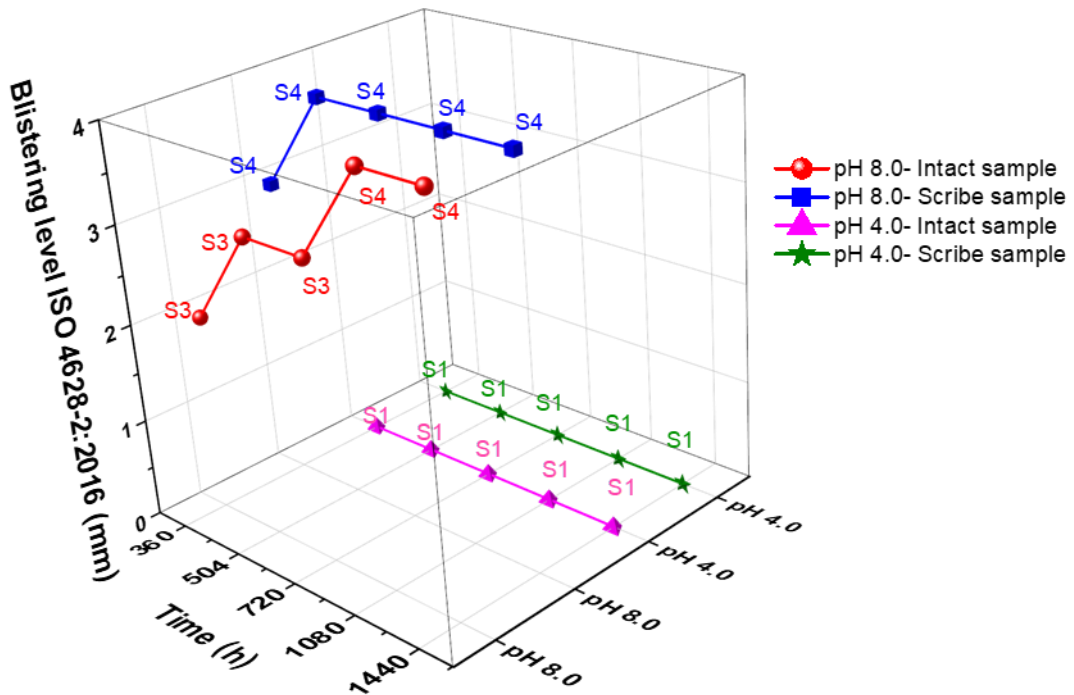
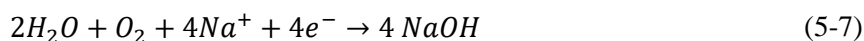


Figure 5-16: Blistering level of freshly coated samples as a function of the pH of the NaCl concentration and time. ISO 4628-2:2016 defined the density of blisters (0: none to 5: many). The data labels represent the blister size (S1: none to S5: >5 mm).

The cathodic reaction that occurs under the coating generated OH^- ions in the cathodic zone [28], as shown by equation (5-3). The OH^- can result in the dissolution of oxide layers on the metal surface and break the chemical bonds at the coating–metal interface. At the cathodic sites, oxygen is reduced, and in the presence of cations, such as Na^+ , a highly alkaline NaOH solution is formed at the coating/metal(oxide) interface [40]:



As osmotic force drives water has a low NaOH concentration in bulk solution (aforementioned, pH 8.0 was adjusted with 4.0 wt. % NaOH in 3.5 wt. % NaCl solution) through the coating to a high concentration of an alkaline solution in the interface area (metal/coating), which increase the coating deformed upward [41]

5.4.2.2 Delamination degree around the scribed area

The images in Table 5-8 and Table 5-9 show the morphology around the scribed regions of the phenolic-epoxy coated specimens before and after testing in alkaline and acidic solutions, respectively. The exposure to heat alone resulted in colour changes, as reported extensively [20]. After the coating was exposed to moisture, corrosion products are visible. It

can also be observed from Table 5-8 and Table 5-9 that the samples exposed to water condensation were most susceptible to delamination, compared to the samples fully immersed in the 3.5 wt. % NaCl solutions at different pH levels.

Table 5-8: Photographs showing the degree of delamination of the phenolic-epoxy coating after exposure to acidic 3.5 wt.% NaCl at 80 °C for 60 d under condensation and immersion conditions





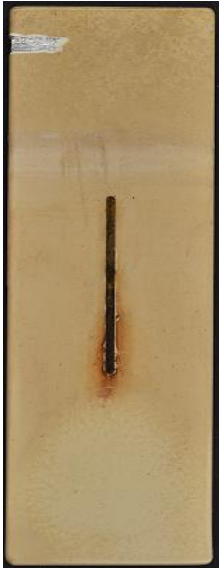

	Pre-exposure to the test	Immersion in acidic solution at 80 °C for 60 d	Exposed to condensing vapour at 80 °C for 60 d
Freshly coated panel			
A coated panel exposed to thermal cycling of 22 to 120 °C for 40 d			

Table 5-9: Photographs showing the degree of delamination of the phenolic-epoxy coating after exposure to alkaline 3.5 wt. % NaCl at 80 °C for 60 d under condensation and immersion conditions.

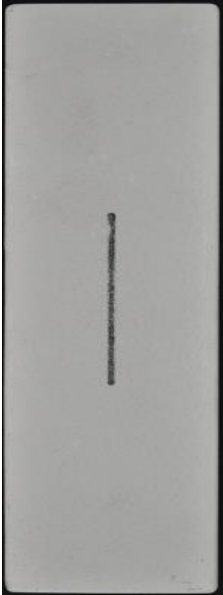





	Pre-exposure to the test	Immersion in alkaline solution at 80 °C for 60 d	Exposed to condensing vapour at 80 °C for 60 d
Freshly coated panel			
A coated panel exposed to thermal cycling of 22 to 120 °C for 40 d			

Figure 5-17 shows that under alkaline condensation conditions, more significant degradation of the freshly coated panel occurred compared to the heat-treated sample. After the heat treatment of the coated panels, delamination was 1.95 mm.

Slightly greater degradation occurred in the freshly coated panel contained in the test cell with an acidic condition compared to the heat-treated sample. More specifically, a delamination of 0.2 mm was observed on the panel.

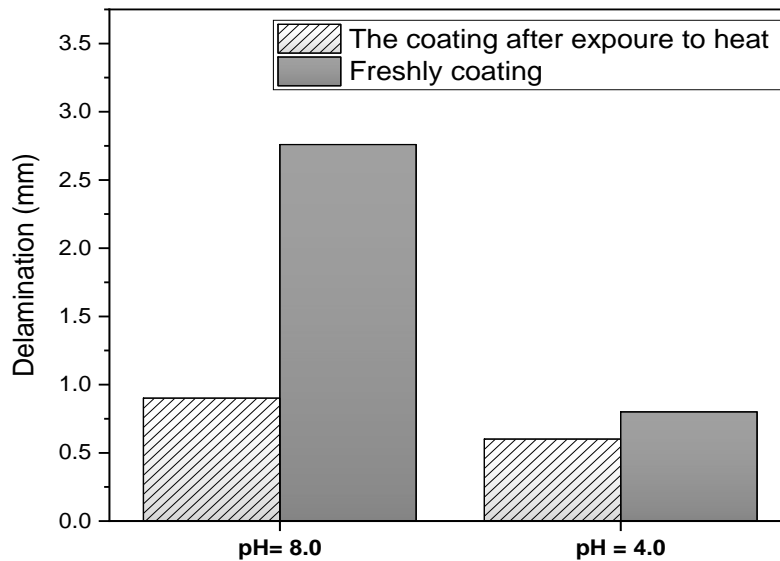
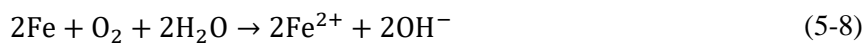


Figure 5-17: Comparison of the delamination value around the scribed regions of phenolic-epoxy-coated steel panels exposed to condensation conditions with acidic and alkali NaCl solutions.

The lesser delamination risk at the scribe region when the samples were fully immersed may be attributed to the diffusion control nature of the oxygen reduction reaction, resulting in lower hydroxyl ions being generated equation (5-3) [15,42].

This is similar to what was observed in the previous experiment; the coating degradation around the scribe area occurred only at condensation conditions. The system is considered a close system; the percentage of O₂ in the atmosphere is 21% compared with CO₂ is 0.041%, so the corrosion mechanism is dominated by dissolved oxygen in the water as shown in equation (5-8)



The solubility of oxygen in the thinner layer of electrolyte (vapour phase) is more than in bulk solution (liquid phase).[23] The oxygen leads to increased releases of OH^- ions, affecting the interface area between (metal/ coating) and breaking bonds at the coating oxide metal [43-47].

The delamination area around scribed panels was high in alkaline environment containing NaCl and NaOH components. As aforementioned, the test solution is replenished daily and poured into the test cell, where electrolyte drops fall onto the samples at the upper part of the glass cell. The NaOH component reinforced the osmotic driving force through the coating and faster penetration into the capillary channels in the coating, as illustrated in section 5.4.2.1.

5.4.2.3 Electrochemical performance

The Nyquist plots of electrochemical impedance in Figure 5-18 and Figure 5-19 reflect four patterns, which represent four behaviours of the coated panels. A low impedance was typical for the fresh samples in the alkaline NaCl solution (Figure 5-18a). The EIS plot showed two characteristics: At a scribe on a freshly coated panel was a semi-circle in a capacitance loop that changed at a high-frequency range and an oblique line that appeared at a high-frequency range. By contrast, the intact, freshly coated specimen had a semi-circle in a capacitance loop that changed at a low-frequency range and an oblique line that appeared at a low-frequency range. These phenomena indicate that the coating was degraded (appearance blisters) as shown in Table 5-6.

The coated panels exposed to heat and immersed in the alkaline had two characteristics as illustrated in Figure 5-18b. At the scribe panel was a semi-circle with high impedance, suggesting that the water penetrated the coating, and the corrosive medium diffused into the coating/metal interface. In the intact coated panel, the impedance spectra terminated by a straight line occurring at an angle of 45° , implying that the water penetrated the coating but did not reach the coating/metal interface. This finding is also reflected in the high impedance of the coated panels in the vapour phase.

As indicated in Figure 5-19, the EIS impedance spectra behaved in two ways. On the freshly coated specimens immersed in the acidic solution was a single semi-circle with high impedance. All the other samples showed high impedance with a straight line at an angle of 45° .

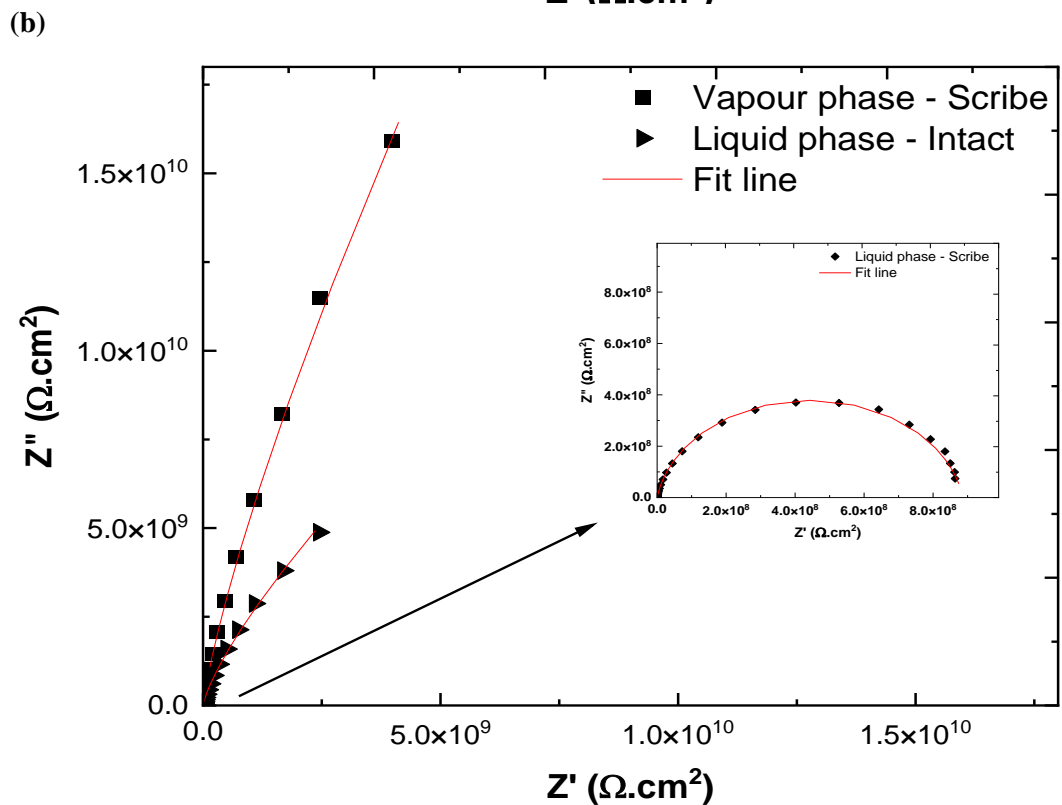
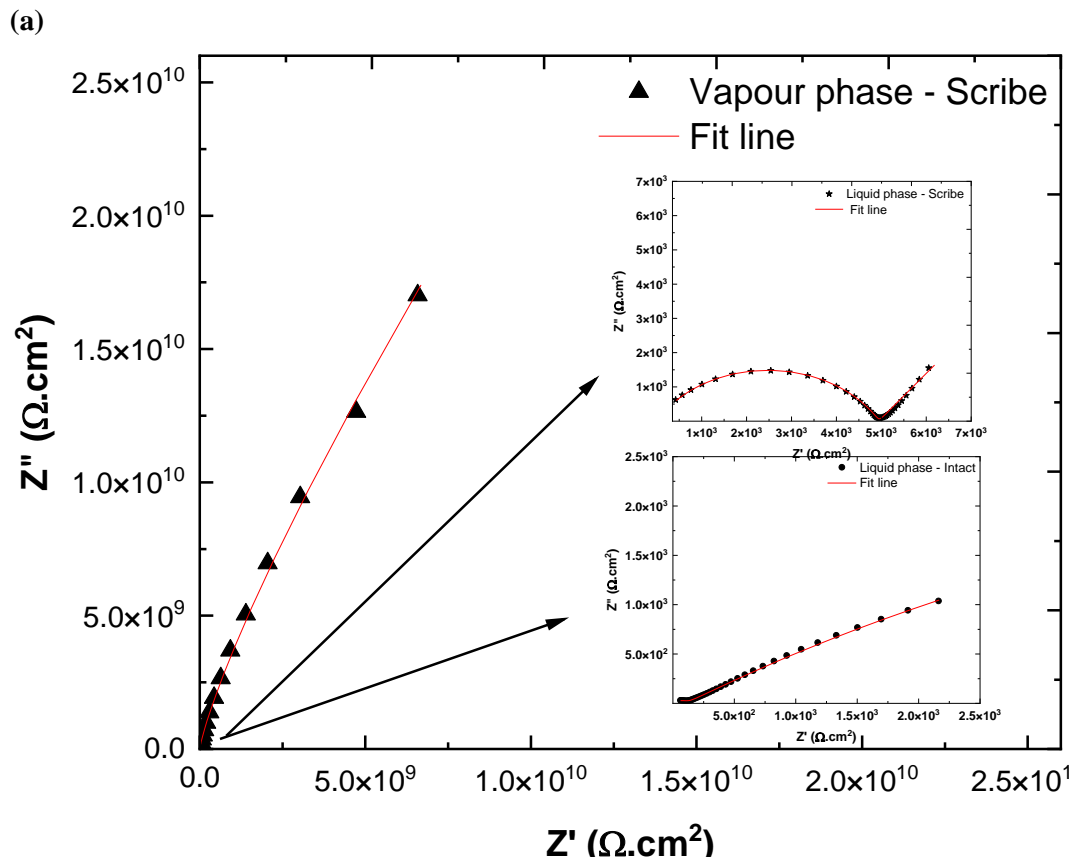


Figure 5-18: Nyquist plots of phenolic-epoxy-coated steel panels after 1440 h of exposure to alkaline 3.5 wt. % NaCl solution at 80 °C in glass cells containing (a) freshly coated panels or (b) coated panels exposed to thermal treatment.

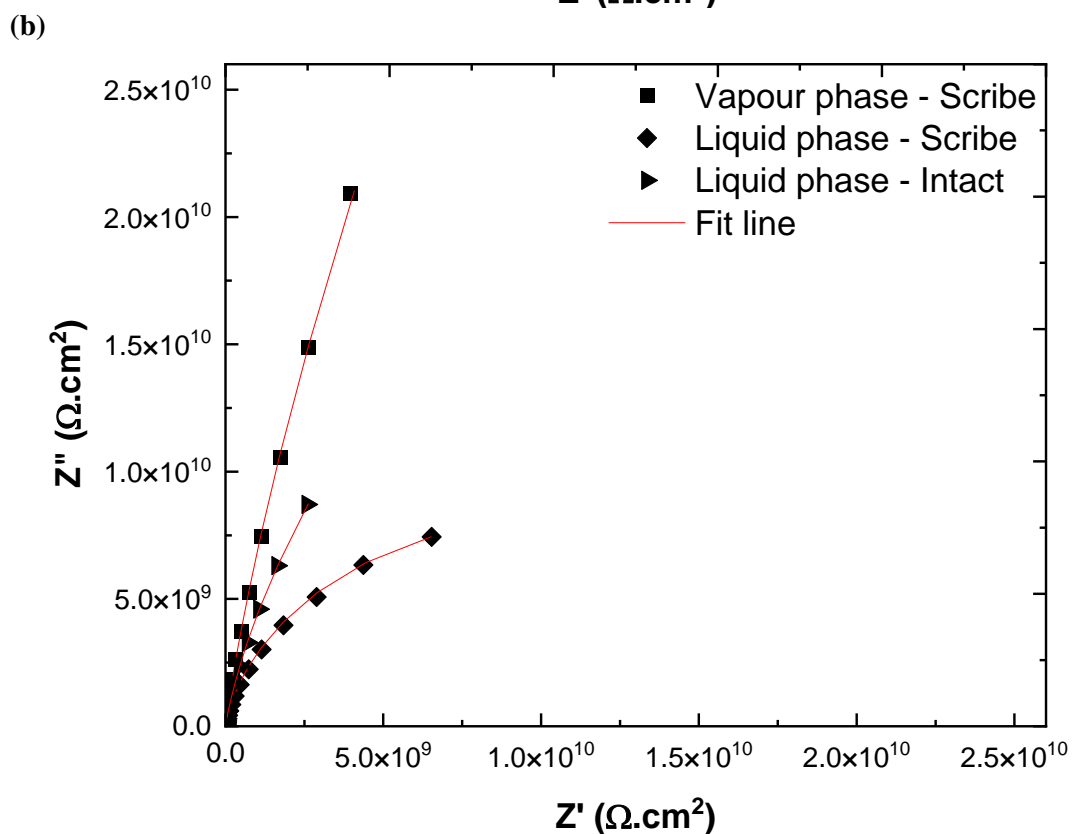
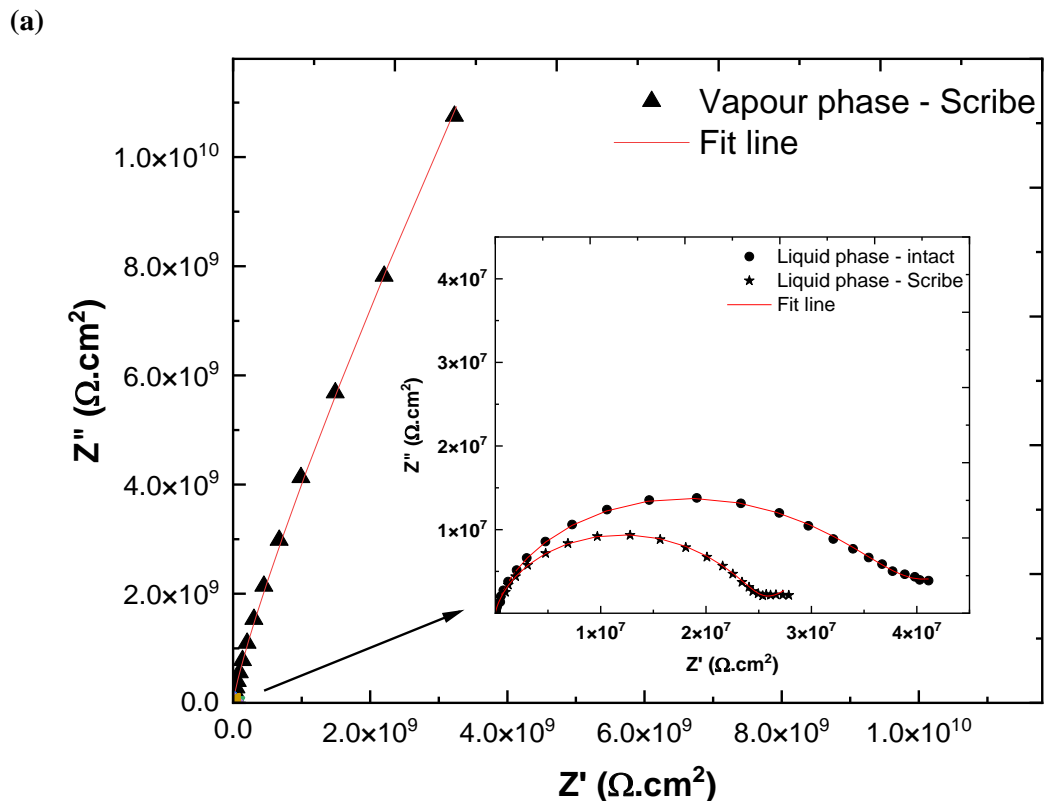


Figure 5-19: Nyquist plots of phenolic-epoxy-coated steel panels after 1440 h of exposure to acidic 3.5 wt. % NaCl solution at 80 °C in glass cells containing (a) freshly coated panels or (b) coated panels exposed to thermal treatment.

Figure 5-20 and Figure 5-21 illustrate the evolution of the Bode plots of the wholly coated panels exposed to condensed water (vapour phase). These samples exhibited the highest impedance of 10^9 to $10^{10} \Omega.cm^2$.

The freshly coated specimens immersed in a solution with a pH = 8.0, whether intact or scribe the decline was substantial, the impedance decreased to $10^3 \Omega.cm^2$ (Figure 5-20a). The shape of the plots for a coated metal with two minima for the phase plot indicates the onset of the electrochemical corrosion reaction at the metallic substrate and initial insight into the coating degradation [48], as shown in Table 5-6.

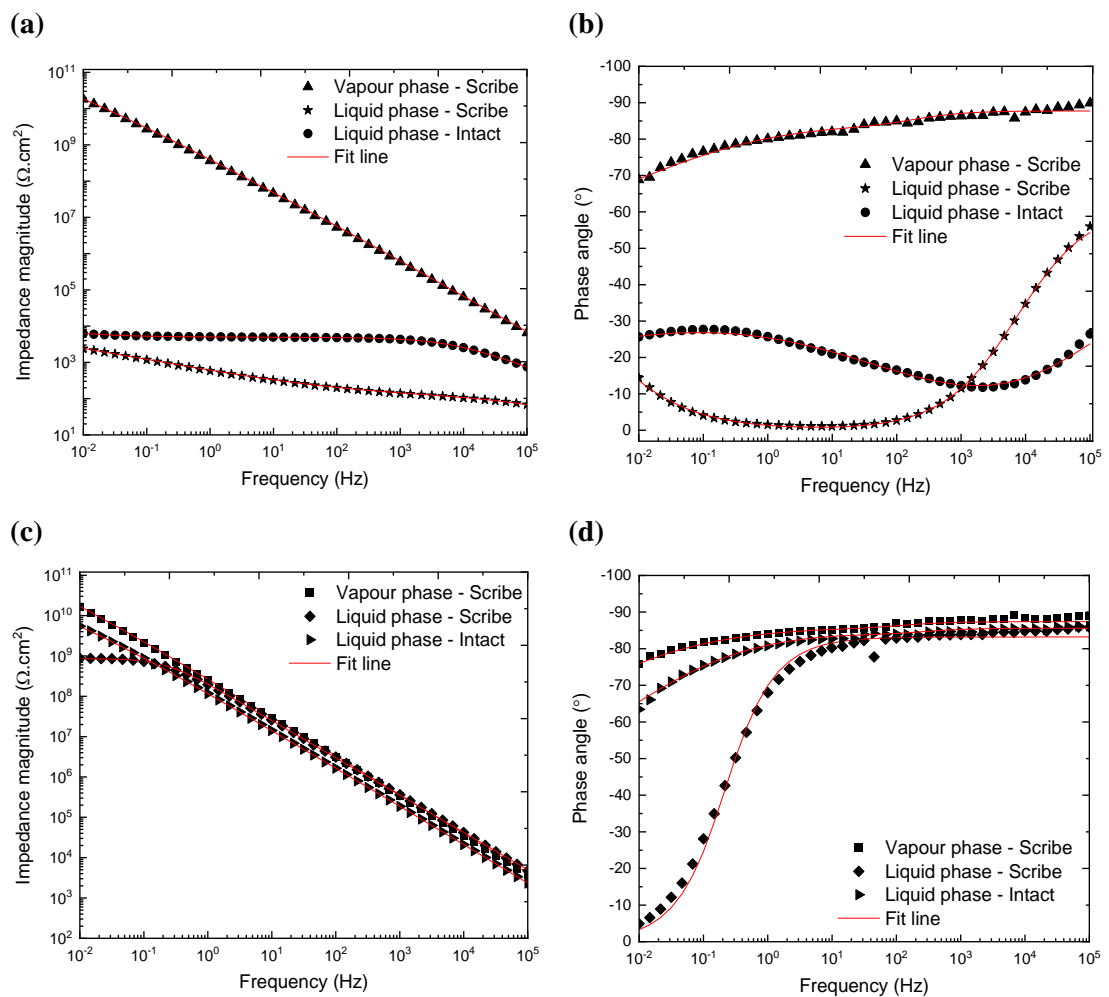


Figure 5-20: Bode plots: (a, c) impedance and (b, d) phase angle of steel panels coated with phenolic-epoxy resin (a, b) before and (c, d) after exposure to heat and 3.5 wt. % NaCl solution (pH 8).

Figure 5-20a-c and Figure 5-21a-c, show the coated specimens exposed to heat and then immersed in solutions of different pH levels had impedances of 10^9 to $10^{10} \Omega.cm^2$. Furthermore, a slight reduction in impedance occurred in the freshly coated panels (intact or scribe) immersed in a solution with a pH = 4.0 (i.e., $10^7 \Omega.cm^2$; (Figure 5-21a).

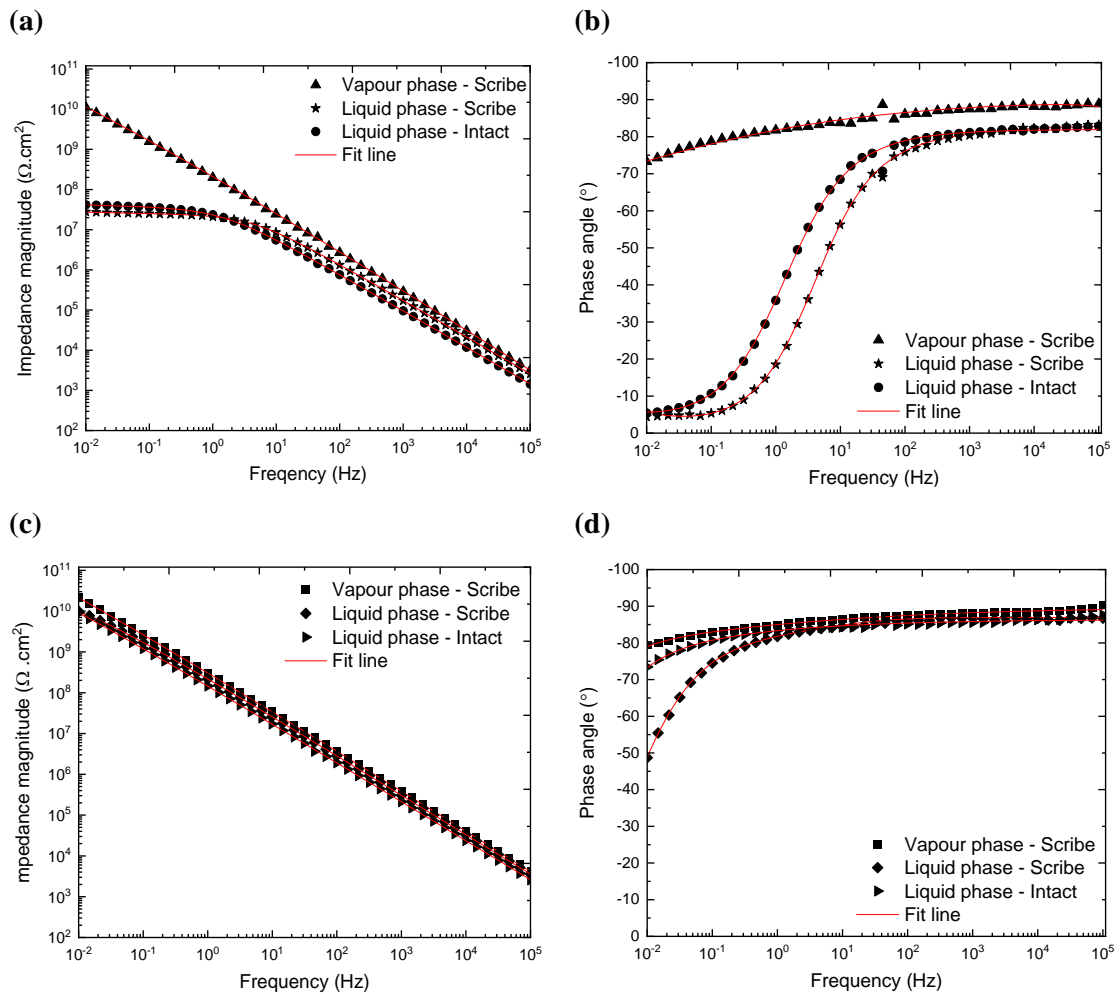


Figure 5-21: Bode plots: (a, c) impedance and (b, d) phase angle of steel panels coated with phenolic-epoxy resin (a, b) before and (c, d) after exposure to heat and 3.5 wt. % NaCl solution (pH 4).

5.5.4 Thermal behaviour

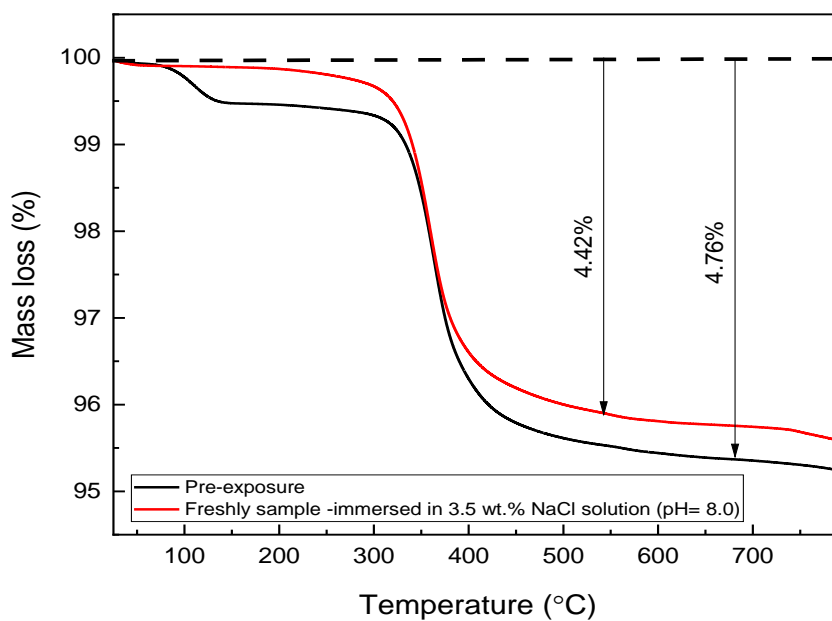
The thermal analysis focused on the freshly coated panels immersed in alkaline 3.5 wt. % NaCl solution because these conditions resulted in significant blistering. The TGA and DTGA results are shown in Figure 5-22. The major reactions include dehydration with the formation of a double bond in the chain, double bond isomerisation, and allyl-oxygen bond scission [49]. Figure 5-22a shows TGA mass loss vs temperature curves ($10^\circ\text{C}/\text{min}$). At low temperatures ($67\text{--}130^\circ\text{C}$), the curves show a mass loss of $\sim 0.5\%$ due to the loss of volatiles (such as water) and low-MW monomers. See section 4.4.3 for details regarding the curing reaction of epoxy during such tests.

The emission of water could be due to the condensation reaction between the residual methylol groups and phenolic OH groups (see equation 4-2), which can form new cross-links [50].

All samples showed curves with a similar shape, but different residual masses (4.42–4.76%) at the end of the decomposition stage. The overall slope of the mass-loss curve is proportional to the rate of weight loss. The derivative value of weight loss is higher for the sample before immersion than after immersion in the alkaline solution. A decrease in the decomposition rate is related to the formation of surface residues, which are characterised by increased thermal stability [51]. The freshly coated panel was less stable; the mass loss indicates the breaking of chemical bonds [51].

The curves in Figure 5-22b show a single endothermic process for all studied samples around the same temperature (336.2 °C), which is attributed to material decomposition [52]. Furthermore, the curve for the pre-exposure sample has an additional endothermic peak at 111.7 °C, which could be due to the phase separation of the epoxy mixture during dehydration, as noted earlier [53].

(a)



(b)

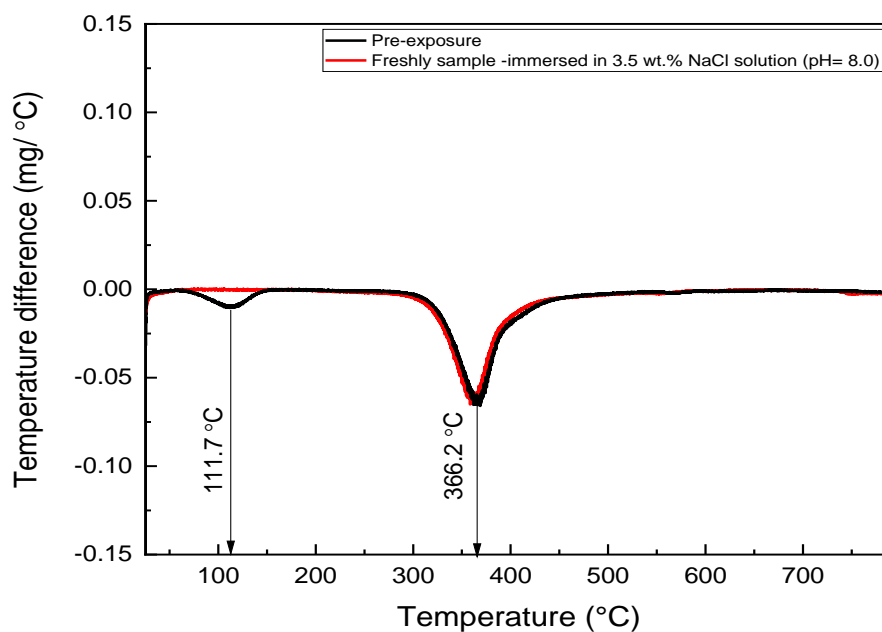


Figure 5-22: TGA/DTGA curves of phenolic epoxy coating under N₂ gas (a) TGA pattern and (b) DTGA pattern.

The DSC curves used to obtain the T_g values of the samples are shown in Figure 5-23. The T_g of the freshly coated panel is 121.6 °C before immersion, which drops to 117.6 °C after immersion. The reduction in T_g was associated with a low molecular-chain strength and

low molecular weight [54]. The water is a destructive element that can permeate a protective coating when the T_g is low in the coating layer, causing blistering [55].

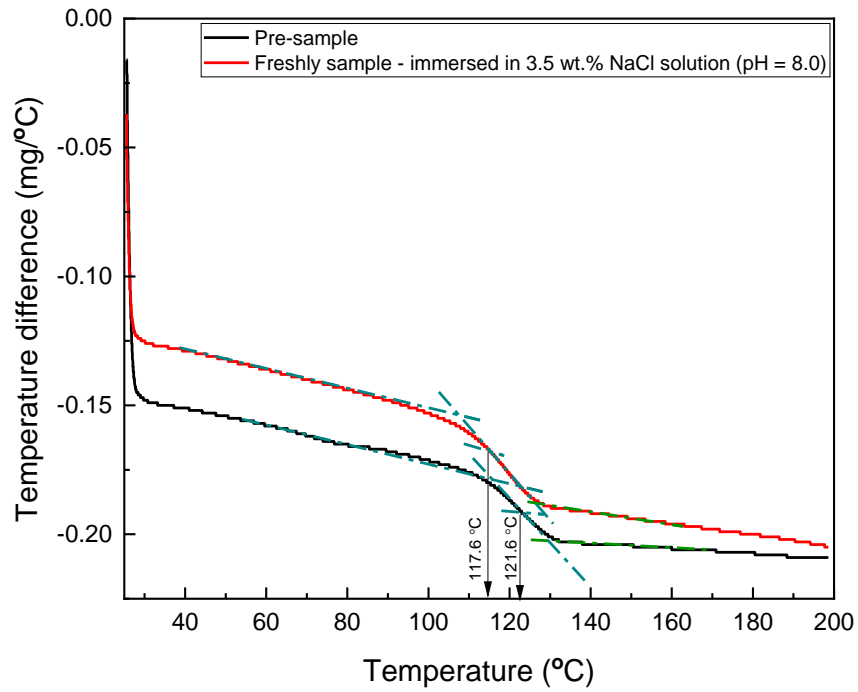


Figure 5-23: DSC diagrams for freshly phenolic coating before and after immersion in 3.5 wt.% NaCl solution (pH = 8.0).

5.5. Conclusions

This chapter investigated the effect of NaCl concentration and pH on the performance of phenolic-epoxy coated steel panels before and after exposure to thermal cycling (between 22 and 120 °C for 40 d). Different NaCl concentrations and pH levels were used to mimic acidic/alkaline marine environments. The main conclusions are as follows:

The steel panels that were freshly coated with the phenolic epoxy resin were more sensitive to 3.5 wt. % NaCl than to 5.0 wt. % NaCl. Corrosive species such as water, oxygen, and corrosive ions (NaCl) penetrated the coating to reach the coating–metal interface and degraded the coating film. Oxygen concentration in the solution is an important factor that affects the cathodic half-reaction of the corrosion process. An increase in NaCl concentration reduces the concentration of oxygen and the water activity in the solution, thereby reducing the rate of the cathodic reaction.

Blisters were observed only on the freshly coated panels immersed in 3.5 wt. % NaCl solution with pH 8.0. In addition, freshly coated panels immersed in acidic/alkaline 3.5 wt. % NaCl solutions showed low impedance during EIS. Cathodic reactions in neutral and basic solutions involved the reduction of dissolved oxygen to form hydroxide ions, leading to bond breaking at the coating–metal interface.

However, no blisters were observed on the coating panels exposed to thermal cycling. These panels also showed higher impedance values than freshly coated panels. These findings suggest that the thermal exposure actually enhances the coating's ability to protect carbon steel panels from corrosion.

5.6 References

- [1] G. P. Bierwagen, "Reflections on corrosion control by organic coatings," *Prog. Org. Coatings*, vol. 28, no. 1, p. 5, 1996.
- [2] E. P. M. van Westing, G. M. Ferrari, and J. H. W. de Wit, "The determination of coating performance with impedance measurements-I. Coating polymer properties," *Corros. Sci.*, 1993.
- [3] W. Funke, "Problems and progress in organic coatings science and technology," *Progress in Organic Coatings*. 1997.
- [4] S. Kagwade, "A review of: 'Corrosion Resistant Coatings Technology' by Ichiro Suzuki," *Mater. Manuf. Process.*, 1994.
- [5] Z. W. Wicks, F. N. Jones, S. P. Pappas, and D. A. Wicks, *Organic coatings: science and technology, Third edition*. 2007.
- [6] M. Ogata, N. Kinjo, and T. Kawata, "Effects of crosslinking on physical properties of phenol-formaldehyde novolac cured epoxy resins," *J. Appl. Polym. Sci.*, 1993.
- [7] C. G. Munger, "Corrosion prevention by protective coatings.," 1984.
- [8] C. H. Hare, "Chemically induced degradation," *J. Prot. Coatings Linings*, 1999.
- [9] C. Hare, "Chemically induced degradation of coatings: Part II," *J. Prot. Coatings Linings*, 2000.
- [10] G. Hall, "Understanding the basics of chemical-resistant polyesters and vinyl esters," *J. Prot. Coatings Linings*, 2013.
- [11] H. Hojo, K. Tsuda, M. Kubouchi, and D. S. Kim, "Corrosion of plastics and composites in chemical environments," *Met. Mater. Int.*, 1998.
- [12] V. Moller, K. Johanson, S. Franker, and S. Kiil, "Acid-resistance coatings for the chemical industry a review," *J. Coatings Technol.*, 2017.
- [13] Q. Zhou and Y. Wang, "Comparisons of clear coating degradation in NaCl solution and pure water," *Prog. Org. Coatings*, 2013.
- [14] "INTERNATIONAL STANDARD Petroleum , petrochemical and natural gas," vol. 2012, p. 12, 2018, ISO 19905-1:2012.
- [15] "ISO International, ISO 4628-8:2012, Paints and varnishes-Evaluation of degradation of coatings-Designation of quantity and size of defects, and intensity of uniform

- changes in appearance: Assessment of degree of delamination and corrosion around a scribe ,” *ISO Int.*, vol. 4628–8, 2012.
- [16] H. Y. Nadia Moradi, Saeideh Gorji Kandi, “A new approach for detecting and grading blistering defect of coatings using a machine vision system,” *Measurement*, vol. 1, p. 10, 2022.
- [17] “ISO International, ISO 4628-2:2016, Paints and varnishes-Evaluation of degradation of coatings-Designation of quantity and size of defects, and intensity of uniform changes in appearance: Assessment of degree of blistering.,” *ISO Int.*, vol. ISO 4628-2.
- [18] R. B. Prime, H. E. Bair, S. Vyazovkin, P. K. Gallagher, and A. Riga, “Thermogravimetric Analysis (TGA),” in *Thermal Analysis of Polymers: Fundamentals and Applications*, 2008.
- [19] I. Blanco, L. Oliveri, G. Cicala, and A. Recca, “Effects of novel reactive toughening agent on thermal stability of epoxy resin,” in *Journal of Thermal Analysis and Calorimetry*, 2012.
- [20] A. E. Krauklis and A. T. Echtermeyer, “Mechanism of yellowing: Carbonyl formation during hygrothermal aging in a common amine epoxy,” *Polymers (Basel)*, 2018.
- [21] J. H. Leidheiser, “De-adhesion at the organic coating/metal interface in aqueous media,” 1980, p. 13, *Croatica chemica acta*.
- [22] J. Henry Leidheiser and Richard D. Granata, “CORROSION CONTROL THROUGH A BETTER UNDERSTANDING OF THE METALLIC SUBSTRATE/ORGANIC COATING/INTERFACE,” 1988, *Annual report No. 4, 1 Sep 82-30 Sep 83*. United States.
- [23] H. Leidheiser, W. Wang, and L. Igetoft, “The mechanism for the cathodic delamination of organic coatings from a metal surface,” *Prog. Org. Coatings*, 1983.
- [24] S. Hœrlé, F. Mazaudier, P. Dillmann, and G. Santarini, “Advances in understanding atmospheric corrosion of iron. II. Mechanistic modelling of wet-dry cycles,” *Corros. Sci.*, 2004.
- [25] Z. Mor, S. Assouline, J. Tanny, I. Lensky, and N. Lensky, “effect of water surface salinity on evaporation: the case of a diluted buoyant plume over the dead sea,” *AGU*, vol. 54, no. 1460–1475, p. 16, 2018.
- [26] Q. Zhou, Y. Wang, and G. P. Bierwagen, “Influence of the composition of working

- fluids on flow-accelerated organic coating degradation: Deionized water versus electrolyte solution,” *Corros. Sci.*, 2012.
- [27] (accessed 06.07.13), “http://www.engineeringtoolbox.com/oxygen-solubilty-water-d_841.html,” 2013. .
- [28] M. Taheri, M. Jahanfar, and K. Ogino, “Cathodic disbonding behavior of epoxy - Polyamide coating,” *Eng. Fail. Anal.*, 2021.
- [29] S. D. Cramer, “The Solubility of Oxygen in Brines from 0 to 300 °,” *Ind. Eng. Chem. Process Des. Dev.*, 1980.
- [30] E. D. Schachinger, R. Braidt, B. Strauß, and A. W. Hassel, “EIS study of blister formation on coated galvanised steel in oxidising alkaline solutions,” *Corros. Sci.*, 2015.
- [31] H. Bi and J. Sykes, “Cathodic disbonding of an unpigmented epoxy coating on mild steel under semi- and full-immersion conditions,” *Corros. Sci.*, 2011.
- [32] K. Ogle, S. Morel, and N. Meddahi, “An electrochemical study of the delamination of polymer coatings on galvanized steel,” *Corros. Sci.*, 2005.
- [33] E. Cano, D. Lafuente, and D. M. Bastidas, “Use of EIS for the evaluation of the protective properties of coatings for metallic cultural heritage: A review,” *Journal of Solid State Electrochemistry*. 2010.
- [34] M. Mahdavian and S. Ashhari, “Mercapto functional azole compounds as organic corrosion inhibitors in a polyester-melamine coating,” *Prog. Org. Coatings*, 2010.
- [35] B. Lafuente, R. T. Downs, H. Yang, and N. Stone, *RRUFFTM Project*. De Gruyter: Berlin, Germany, 2015.
- [36] K. J. K. R.D. Granata, R.C. MacQueen, “Polymer coating degradation mechanisms related to hot production,” 1993, p. 551.
- [37] M. Xu, W. Zhao, B. Li, K. Yang, and L. Lin, “Synthesis of a phosphorus and sulfur-containing aromatic diamine curing agent and its application in flame retarded epoxy resins,” *Fire Mater.*, 2015.
- [38] J. Wagner, P. Deglmann, S. Fuchs, M. Ciesielski, C. A. Fleckenstein, and M. Döring, “A flame retardant synergism of organic disulfides and phosphorous compounds,” *Polym. Degrad. Stab.*, 2016.
- [39] R. Bolney, M. Grosch, M. Winkler, J. van Slageren, W. Weigand, and C. Robl,

- “Mackinawite formation from elemental iron and sulfur,” *RSC Adv.*, 2021.
- [40] T. J. Chuang, T. Nguyen, and S. Lee, “Micro-mechanic model for cathodic blister growth in painted steel,” *J. Coatings Technol.*, 1999.
- [41] Knudsen and Forsgren, *corrosion control through organic coatings*. pennsylvania: Taylor & Francis group, 2017.
- [42] S. Effendy, T. Zhou, H. Eichman, M. Petr, and M. Z. Bazant, “Blistering failure of elastic coatings with applications to corrosion resistance,” *Soft Matter*, 2021.
- [43] J. I. Skar and U. Steinsmo, “Cathodic disbonding of paint films-transport of charge,” *Corros. Sci.*, 1993.
- [44] O. Knudsen, “Effects of cathodic disbonding and blistering on current demand for cathodic protection of coated steel,” *Corrosion*, 2000.
- [45] D. Roy, G. P. Simon, M. Forsyth, and J. Mardel, “Towards a better understanding of the cathodic disbondment performance of polyethylene coatings on steel,” *Adv. Polym. Technol.*, 2002.
- [46] C. T. Love, G. Xian, and V. M. Karbhari, “Cathodic disbondment resistance with reactive ethylene terpolymer blends,” *Prog. Org. Coatings*, 2007.
- [47] M. Farzam, “Hydrogen degradation of steel-diffusion and deterioration,” *Iran. J. Sci. Technol. Trans. B Eng.*, 2004.
- [48] U. Rammelt and G. Reinhard, “Application of electrochemical impedance spectroscopy (EIS) for characterizing the corrosion-protective performance of organic coatings on metals,” *Prog. Org. Coatings*, 1992.
- [49] D. Puglia, L. B. Manfredi, A. Vazquez, and J. M. Kenny, “Thermal degradation and fire resistance of epoxy-amine-phenolic blends,” *Polym. Degrad. Stab.*, 2001.
- [50] Y. Chen, J. Lee, T. Yu, J. Chen, W. Chen, and M. Cheng, “The curing reaction of poly(ether-sulfone)-modified epoxy resin,” *Macromol. Chem. Phys.*, 1995.
- [51] C. Tsiptsias, “On the specific heat and mass loss of thermochemical transition,” *Chem. Thermodyn. Therm. Anal.*, vol. 8, p. 11, 2022.
- [52] R. Sarathi, R. K. Sahu, and P. Rajeshkumar, “Understanding the thermal, mechanical and electrical properties of epoxy nanocomposites,” *Mater. Sci. Eng. A*, 2007.
- [53] B. K. Kandola, B. Biswas, D. Price, and A. R. Horrocks, “Studies on the effect of different levels of toughener and flame retardants on thermal stability of epoxy resin,”

Polym. Degrad. Stab., 2010.

- [54] A. Zaccone and E. M. Terentjev, “Disorder-assisted melting and the glass transition in amorphous solids,” *Phys. Rev. Lett.*, 2013.
- [55] T. Byrnes, “Pipeline coatings,” in *Trends in Oil and Gas Corrosion Research and Technologies: Production and Transmission*, 2017.

CHAPTER 6

CONCLUSIONS AND FUTURE WORK

6.1 Conclusions

The objective of the thesis was to investigate the behaviour and failure mechanism of phenolic epoxy coatings under various exposure conditions; in particular, the influence of water condensation and immersion in an electrolyte, as experienced in enclosed environments. To achieve this, the thesis was divided into four objectives.

Chapter 3 presented a case study on the effect of chloride ions on carbon steel corrosion in an enclosed environment, simulating the conditions experienced by insulated metal in a marine environment when water is trapped inside the insulation pipe and cannot evaporate. The experiments investigated a possible CUI scenario, where the immersion and condensation experiments with 3.5 wt.% NaCl solution were designed to simulate corrosion of the upper part of the jacketing material and when the electrolyte touches the upper part of the outside pipe and accumulates in the lower part, respectively. In the glass cell used in these experiments, drops of electrolyte remain in contact with the carbon steel surface in the condensation setup on top layer, while the electrolyte immerses the carbon steel specimens in the immersion setup. Finally, the differences between constant temperature (80 °C) and thermal cycling (25 ↔ 80 °C) were evaluated. Several methods were used to characterise the corrosion products, including SEM, EDS, and Raman spectroscopy. Electrochemical techniques such as EN and EIS were used to derive insight into localised corrosion activity and obtain real-time corrosion rates. Uniform corrosion rates were determined using a weight loss technique and the severity of localised corrosion was quantified using 3D surface profilometry. Pitting corrosion was evident on the metal surface of condensation samples, and isothermal heating enhanced the pitting corrosion compared with thermal cycling. In contrast, the specimens immersed in electrolyte exhibited a uniform corrosion layer on the metal surface after both isothermal and thermal cycling conditions, as evidenced by weight-loss and SEM results. Thermal cycling appears to enhance the formation of a protective corrosion-product layer on the carbon steel surface to a greater degree than a constant temperature, thus creating an effective barrier that hinders pitting corrosion of the immersed samples. The pitting factors and EN data showed that uniform corrosion was dominant for the samples immersed in 3.5 wt.% NaCl, and the EN current and potential signals were lower for the immersed samples than the condensation ones.

Chapter 4 discussed the changes in the performance of carbon steel panels coated with phenolic-epoxy coatings when exposed to various dry heating conditions. ToF-SIMS was used to assess the interfacial degradation of the polymer structure by comparing the MW of the coating components before and after thermal treatment. These results confirmed enhanced cross-linking of the coating after it was exposed to 120 °C due to the larger hydrocarbon fragments produced. In contrast, increasing the dry temperature to 150 °C led to a loss of hydrocarbon weight, resulting in cracking of the coating surface. The highest adhesion strength and high EIS impedance values confirmed that the coating performance improved after exposure to thermal cycling (22 ↔ 120 °C for 40 d). After further exposure for 60 d, the opposite results were obtained, i.e., coating degradation evidenced by a decrease in the adhesion strength.

Chapter 5 described the effect of the NaCl concentration and pH on the performance of phenolic-epoxy coated steel panels before and after exposure to thermal cycling (22 ↔ 120 °C for 40 d). This thermal cycling was implemented to simulate the harsh conditions encountered in a marine environment, specifically within an enclosed space where both immersion and condensation are prevalent. Coated specimens were immersed in 3.5 or 5.0 wt.% NaCl at 80 °C for 60 d or exposed to water-condensation conditions. Visual observations of the coating behaviour showed that blisters were observed only on the freshly coated specimens immersed in the various NaCl solutions, but not on the equivalent samples exposed to heat treatment. Delamination around scribed regions of the coatings occurred under condensation conditions, although this behaviour was reduced for the coated panels exposed to thermal cycling. Moreover, the corrosion products were similar for the immersion and condensation samples, except that hematite was detected only beneath the detached coating for the latter. EIS measurements proved that thermal exposure improves corrosion protection. Furthermore, the 3.5 wt.% NaCl solution caused more severe coating failure than the 5.0 wt.% NaCl solution. Finally, to evaluate the effect of solution pH, the same types of coated carbon steel panels were exposed to 3.5 wt.% NaCl solution at pH 4 or 8 for 60 d (immersion and condensation conditions) to simulate the effects of acidic/alkaline marine environments in an enclosed space. The EIS data confirmed that thermal exposure improved corrosion protection to acidic/alkaline solutions. The absence of blisters on the panel surfaces and the reduced delamination around the scribed areas of thermally cycled panels compared with freshly coated ones were noted. Blisters were observed only on the freshly coated specimens immersed in a 3.5 wt.% NaCl solution with pH 8, but not for those immersed in the same solution with pH 4. The alkaline solution caused more severe coating failure than the acidic solution and also decreased the T_g compared to freshly coated panels.

6.2 Future work

This thesis confirms the improved effectiveness of phenolic-epoxy coatings after exposure to thermal cycling (between 22 and 120 °C for 40 d). Enclosed environments were used to simulate CUI conditions or ballast tanks, which often contain aggressive environments, such as high temperature, corrosive salts (e.g., high seawater concentrations), and varying pH levels. The effects of chloride ions on the carbon steel substrate were investigated to clarify the corrosion behaviour and mechanism based on the damage inflicted on the protective coating.

Some recommendations for further research are presented below.

- Clarify the factors contributing to the degradation of heat-treated phenolic-epoxy coatings, such as ultraviolet radiation, leaching of components from insulation materials, abrasion or other mechanical stress, and chemical damage (e.g., from pollutants, sulfites, and sulfates).
- Study the effect of the heat-treatment temperature on the coating performance.
- Evaluate the adhesion strength of coatings to identify the point at which a substrate separates from a surface with different levels of surface roughness (obtained for example using different surface preparation methods perhaps).
- Optimise dry-film thickness of phenolic-epoxy coating after heat treatment to provide maximum substrate protection.

Appendix 1. Written Statements from Co-authors of the Publications

1. Written statements from co-authors of the publication entitled “Investigation of the effect chloride ions on carbon steel in closed environments at different temperatures”.

2. Written statements from co-authors of the submitted manuscript “The performance of phenolic epoxy coating after exposure to high temperatures”.

3. Written statements from co-authors of the published entitled “The performance of phenolic epoxy coating after thermal exposure for corrosion protection in marine environments”.